

**EFFECT OF GRAIN SIZE AND PHASE CONSTITUTION
ON THE MAGNETIC PROPERTIES OF Fe-X-Nb-Si-B [X
= Cu, Au & Ag] ALLOYS**

M. Phil. Thesis

BY

A. K. M. ASADUZZAMAN



**DEPARTMENT OF PHYSICS
KHULNA UNIVERSITY OF ENGINEERING & TECHNOLOGY
KHULNA - 9203, BANGLADESH
NOVEMBER - 2016**

**EFFECT OF GRAIN SIZE AND PHASE CONSTITUTION
ON THE MAGNETIC PROPERTIES OF Fe-X-Nb-Si-B [X
= Cu, Au & Ag] ALLOYS**

BY

A. K. M. ASADUZZAMAN

ROLL NO: 1155552

SESSION: JULY - 2011

**A THESIS SUBMITTED TO THE DEPARTMENT OF PHYSICS,
KHULNA UNIVERSITY OF ENGINEERING & TECHNOLOGY,
KHULNA - 9203 IN PARTIAL FULFILMENT OF THE
REQUIRMENT FOR THE DEGREE OF MASTER OF
PHILOSOPHY**



**DEPARTMENT OF PHYSICS
KHULNA UNIVERSITY OF ENGINEERING & TECHNOLOGY
KHULNA - 9203, BANGLADESH
NOVEMBER - 2016**

This noble work has been

DEDICATED

TO

MY PARENTS

DECLARATION

This is to certify that the thesis work entitled as “**Effect of Grain size and Phase constitution on the Magnetic Properties of Fe-X-Nb-Si-B [X = Cu, Au & Ag] Alloys**” has been carried out in partial fulfillment of the requirement for M. Phil degree in the department of Physics, Khulna University of Engineering & Technology, Khulna - 9203, Bangladesh. The above research work or any part of this work has not been submitted anywhere for the award of any degree or diploma. No other person’s work has been used without due acknowledgement.

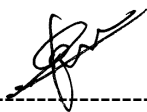
1. Supervisor

Candidate

(Prof. Dr. S. S. Sikder)

(A. K. M. Asaduzzaman)

2. Co-Supervisor



(Dr. M. A. Gafur)

Acknowledgements

I express, with due respect my deepest sense of sincere gratitude indebtedness to my supervisor Prof. Dr. Shibendra Shekher Sikder, Department of Physics, Khulna University of Engineering & Technology (KUET), Khulna for his indispensable guidance, erudite discussion, constructive suggestions, fruitful discussion and constant inspiration throughout the research work. He is always ready to provide a lucid explanation of the different concepts involved and critical reading of the script and subsequent corrections are much appreciated. Any mistake that remain is of course mine.

I am very much indebted to my Co-Supervisor Dr. Abdul Gafur, Senior Engineer, PP & PDC, Bangladesh Council of Scientific and Industrial Research (BCRID), Dhanmondi, Dhaka-1205, Bangladesh for introducing the present research topic and inspiring guidance and valuable suggestion throughout the research work who has supported consistently and necessary motivation to progress my experimental works.

It is a matter of great pleasure for me to record the deepest sense of gratitude to Prof. Dr. Md. Mahbub Alam, Prof. Dr. Abdullah Elias Akther and Prof. Dr. Jolly Sultana Department of Physics, KUET, have been given me a strong support in various ways during the entire period of my study in the department of Physics KUET. I am thankful to Mr. Sujit Kumer Shil and Mr. Alamgir Hossain, Assistant professor, Department of Physics, KUET of their tired less co-operation in my thesis work.

I am grateful to Dr. Sk. Manjura Hoque, Head & Chief Scientific Officer, Materials Science Division, Atomic Energy Centre, Dhaka (AECD) for providing kind opportunity to work her laboratory for experimental work. I wish to thanks all the scientist of Materials Science Division, especially to Dr. Nazrul Islam Khan, Dr. Md. Mahbul Haque, Mrs. Samia Islam Liba for their support and Scientific discussion to do this research work.

I am deeply grateful to Mr. Rakibul Qadir, Engineer, PP & PDC, Bangladesh Council of Scientific and Industrial Research (BCSIR) Dhanmondi, Dhaka-1205, Bangladesh, who helped me to understand annealing XRF measurement and technical assistance in the laboratory. My thanks are also for all the staff of Heat Treatment Section, PP & PDC, BCSIR who all were very much co-operative with me.

I must express my heartfelt gratitude to Mr. Suman Kumar Halder, Lecturer, Department of Physics, KUET, Mr. Rahat Kumar Howlader, Mr. Nitish Chandro Mollik, Mr. Md. Humayan Ahmed, Mr. Zakir Hossain and as well as my fellows Md. Abdul Gofur, and other postgraduate students of our group and friends who have given me a lot of encouragement to accomplish this noble work.

I am very much grateful to Brigadier General Moshir Rahaman, PSC, Principal, MCSK, Lt.Colonel Farhad Harun Chowdhury, Vicc-Principal, Adjutant Major Md. Ariful Islam as well as my colleagues Assistant professor A.K.M Nasimul Islam, Assistant professor Md. Jahangir Hosen, Lecturer Md. Masum Billah (department of physics) who supported me to make duties easier and with necessary help.

I want to acknowledge the memorable well-wisher my elder brother A. K. M Kamaruzzaman Executive Engineer, Shahidullah Associates, Dhaka, who provided me a lot of encouragement to go for M. Phil program. He always asked about the progress and gave me the correct guideline. Mostly indebted forever to the best personality my maternal father in law Abdul Karim Shuja, Senior Vice President, Bank of Sharjah, Dubai, who helps me in all of my life's decisions staying in Dubai.

Many thanks are due to the Director, Atomic Energy Center, Dhaka for his kind permission to use the laboratory of Material Science Division, AEC, Dhaka

I wish to express thanks to my life-partner Azizun Nahar Bela for keeping me free from family-affairs during my work and also for her sustained inspiration, encouragement and continuous co-operation. Finally, thanks to my only loving son Ayman Bin Asad Khan.

My gratitude and thanks are also to my father, mother, father-in-law, mother-in-law, brothers, sisters, nephew, niece and all of my family members who all were very much co-operative with my higher studies.

A very special thanks to Mrs. Nandita Saha, spouse of Prof. Dr. S. S. Sikder for her heartfelt encouragement, cares and helps throughout the entire period of M. Phil. program.

I also wish to thank the authority of Khulna University of Engineering & Technology (KUET), Khulna for providing me with the necessary permission and financial assistance for conducting this thesis work.

ABSTRACT

Amorphous FINEMET type alloy nominal composition of $\text{Fe}_{73.5}\text{X}_1\text{Nb}_3\text{Si}_{13.5}\text{B}_9$ [X = Cu, Au and Ag] has prepared by melt spinning technique. The samples are initially prepared in the amorphous state in the form of thin ribbons by rapid quenching technique at wheel speed of 25m/s in an Ar atmosphere. The ribbon has been annealed in a controlled way in temperature range $450^\circ - 800^\circ\text{C}$ for 30 minutes. The kinetics of crystallization amorphous FINEMET type alloys were investigated by the use of differential thermal analysis (DTA) and X-ray diffraction (XRD) techniques. DTA runs for these three samples show the existence of two exothermic peaks one for $\alpha\text{-Fe}(\text{Si})$ and other for Fe_2B phase. The crystallization of each phase has occurred over a wide range of peak temperatures and the primary crystallization like $\alpha\text{-Fe}(\text{Si})$ phase temperature shift higher temperature as the replace $\text{Ag} > \text{Au} > \text{Cu}$ concentration. DTA experiment and from the obtain data activation energy of primary crystallization $\alpha\text{-Fe}(\text{Si})$ phase are varies 2.18 - 4.37eV and secondary crystallization products Fe_2B phase is 3.62 - 4.45 eV. Amorphosity of the ribbon and nanocrystalline state has been evaluated by XRD. The primary crystallization phase shifts to higher annealed temperature with Cu replacement Au or Ag implying the enhancement of thermal stability of amorphous alloys against crystallization. All the three samples has been annealed in the temperature range $600^\circ\text{C} - 800^\circ\text{C}$ for 30 minutes and taken under XRD experiment in order to study the effect of structural parameters such as lattice parameter, grain size and silicon content of the nanocrystalline $\alpha\text{-Fe}(\text{Si})$ grain. In optimizing annealing condition the grain size has been obtained in the range of 14 - 20nm for Cu, 13 - 25nm for Au and 09 - 30nm for Ag. Saturation magnetization M_s increase in order with condition $\text{Ag} > \text{Cu} > \text{Au}$ in these experimental samples. The reduction curie temperature (T_c) with substitution of Cu by Au or Ag in order $\text{Ag} < \text{Au} < \text{Cu}$ may attributed to this simultaneous weakening of strength of exchange interaction between the magnetic moments. This is because the amorphous matrix is depleted Fe and relative amount of Nb in the amorphous matrix increases Cu replace Au or Ag which weakness the exchange interaction resulting in reduction of T_c .

Contents

	Page No.
Title Page	
Declaration Page	i
Acknowledgement	ii
Abstract	iv
Contents	v
List of Figures	viii
List of Tables	xiii
List of Symbols	xv

CHAPTER I

INTRODUCTION

1.1	Introduction	1
1.2	The Aim and Objectives of the Present Work	4
1.3	Experimental Reason for Choosing this Research Work	4
1.4	Application of Nanocrystalline Ribbons	6
1.5	Review of Researches on FINEMET	7
1.6	Organization of the Thesis	10

CHAPTER II

THEORETICAL BACKGROUND

2.1	History of Nanocrystalline Materials	11
2.2	Composition of the Nanocrystalline	12
2.2.1	An Overview of Nanocrystalline materials	14
2.2.2	Alloy Design Issues	15
2.2.3	Stages of Evolution of Microstructure	17
2.2.4	Advantages of Soft Nanocrystalline Alloys	19
2.2.5	Viscosity Condition for the Formation of Metallic Glass	20
2.2.6	Condition for the Formation of Nanocrystalline Alloys	21
2.3	Factors Contributing to glass formation and stability	22
2.3.1	Stability of the Amorphous and Nanocrystalline Materials	24
2.3.2	Characteristics of the Glass Transition Temperature	25

2.4	Differential Thermal Analysis and its Application	26
2.5	Evaluation of Activation Energy Based on DTA Technique	27
2.6	Determination of Nanometric Grain Size by X-Ray Diffraction	28
2.6.1	Random Anisotropy Model (RAM)	31
2.7	Magnetic Dipole Moments and magnetization	34
2.7.1	Magnetization of the Nanocrystalline Ribbon	36
2.7.2	Ferromagnetic Ordering (Curie) Temperatures	36

CHAPTER III

EXPERIMENTAL DETAILS

3.1	Methods used for Preparation of Nanocrystalline Alloy	39
3.1.1	The Fast cooling of The Melt	39
3.1.2	Sample for Master Alloy Preparation	40
3.1.3	Preparation of Ribbon by Melt Spinning Technique	41
3.1.4	Important Factors to Control the Thickness of Ribbon	43
3.1.5	Confirmation of Amorphousity Ribbons	43
3.2	Thermal Analysis Techniques	44
3.2.1	The principle of Differential Thermal Analysis	45
3.2.2	Apparatus	47
3.2.3	Experimental Factors	49
3.2.4	Interpretation and Presentation of DTA	50
3.3	Annealing	52
3.3.1	Stages	52
3.3.2	Setup and Equipment	53
3.4	Thermal Treatment of the Nanocrystalline Amorphous Ribbon	53
3.5	Powder/Polycrystalline Diffraction	54
3.5.1	Theoretical Consideration of X-Ray Diffraction (XRD)	54
3.5.2	X-Ray Powder Method	56
3.5.3	Experimental Technique for X-Ray Diffractometer	57
3.5.4	Analysis of XRD data	60
3.6	Magnetization Measurement Technique	62
3.6.1	Vibrating Sample Magnetometer (VSM)	62
3.6.2	Principle of VSM	62

CHAPTER IV

RESULTS AND DISCUSSIONS

4	Results and Discussion	65
4.1	Crystallization Behavior of Fe-X-Nb-Si-B Alloys	65
4.2	DTA Results of Fe -X-Nb-Si -B ribbons as affected by Cu, Au and Ag content.	66
4.2.1	Study of DTA traces of Fe _{73.5} Cu ₁ Nb ₃ Si _{13.5} B ₉ Alloy	68
4.2.2	Study of DTA Traces of Fe _{73.5} Au ₁ Nb ₃ Si _{13.5} B ₉ Alloy	74
4.2.3	Study of DTA traces of Fe _{73.5} Ag ₁ Nb ₃ Si _{13.5} B ₉ Alloy	80
4.3	Comparison between DTA of Fe-X-Nb-Si-B and original FINEMET	86
4.4	Microstructural Analysis of Amorphous and Nanocrystalline Fe-X-Nb-Si-B [X=Cu, Au and Ag] Alloy by XRD Analysis	87
4.4.1	XRD Analysis of the Nanocrystalline Ribbon with Composition Fe _{73.5} Cu ₁ Nb ₃ Si _{13.5} B ₉	90
4.4.2	XRD Analysis of the Nanocrystalline Ribbon with Composition Fe _{73.5} Au ₁ Nb ₃ Si _{13.5} B ₉	94
4.4.3	XRD analysis of the Nanocrystalline Ribbon with composition Fe _{73.5} Ag ₁ Nb ₃ Si _{13.5} B ₉	97
4.5	Specific Magnetization Measurement of Fe-X-Nb-Si-B [X=Cu, Au and Ag] Nanocrystalline Amorphous Ribbons	101
4.5.1	Temperature Dependence of Specific Magnetization Fe-X-Nb-Si-B [X=Cu, Au and Ag] Nanocrystalline Amorphous Ribbons	104

CHAPTER V

CONCLUSION

5.1	Conclusion	109
5.2	Scope for Future Work	111
	Reference	113

List of Figures

Figure No	Descriptions	Page No
Figure 2.1	Flow chart for the consideration in designing and developing nanocrystalline soft magnetic material from an amorphous precursor route	16
Figure 2.2	Schematic illustration of the formation of nanocrystalline structure	17
Figure 2.3	FINEMET is superior compared to conventional materials	19
Figure 2.4	Volume-Temperature relationship in solid ,liquid, and glass state	23
Figure 2.5	Effect of fine particle broadening in XRD (a) fine particle and (b) perfect crystal	24
Figure 2.6	Schematic representation of Random Anisotropy Model (RAM)(a) Assembly of grains, each of them is having a randomly fluctuating anisotropy axis (b) The correlation volume of size L_{ex} in nanocrystalline material consisting of grains	31
Figure 3.1	Vacuum Arc Melting Machine	41
Figure 3.2	Schematic Diagram	42
Figure 3.3	Melt-Spinning Machine	42
Figure 3.4	X-ray diffraction of as-cast nanocrystalline amorphous ribbons with Composition Fe-X-Nb-Si-B [X=Cu, Au and Ag]	44
Figure 3.5(a)	Heating curve of sample and reference substance	46
Figure 3.5(b)	DTA Curve	46
Figure 3.6	Schematic illustration of a DTA cell	48
Figure 3.7	Block diagram of a DTA equipment, (S) sample thermocouple, (R) reference thermocouple, (M) monitor thermocouple	49
Figure 3.8	SII EXSTAR 6000 TG/DTA 6300 assembly	51
Figure 3.9	MTI - GSL-1600x40 Tube Furnaces	54

Figure 3.10	Bragg's diffraction pattern	55
Figure 3.11	Reflection and Transmission geometry of powder diffraction	59
Figure 3.12	Block diagram of the Bruker AXS D8 Advance XRD system	57
Figure 3.13	Bruker AXS D8 Advance	58
Figure 3.14	Vibrating Sample Magnetometer (VSM)	63
Figure 4.1	DTA traces of as-cast nanocrystalline amorphous ribbon Fe-X-Nb-Si-B [X = Cu, Au and Ag] at the heating rate of 50°C/min	67
Figure 4.2(a)	DTA trace of as-cast nanocrystalline amorphous ribbon Fe _{73.5} Cu ₁ Nb ₃ Si _{13.5} B ₉ at the heating rate of 10°C/min	69
Figure 4.2(b)	DTA trace of as-cast nanocrystalline amorphous ribbon Fe _{73.5} Cu ₁ Nb ₃ Si _{13.5} B ₉ at the heating rate of 20°C/min	69
Figure 4.2(c)	DTA trace of as-cast nanocrystalline amorphous ribbon Fe _{73.5} Cu ₁ Nb ₃ Si _{13.5} B ₉ at the heating rate of 30°C/min	70
Figure 4.2(d)	DTA trace of as-cast nanocrystalline amorphous ribbon Fe _{73.5} Cu ₁ Nb ₃ Si _{13.5} B ₉ at the heating rate of 40°C/min	70
Figure 4.2(e)	DTA trace of as-cast nanocrystalline amorphous ribbon Fe _{73.5} Cu ₁ Nb ₃ Si _{13.5} B ₉ at the heating rate of 50°C/min	71
Figure 4.3	Effects of heating rate on DTA traces of nanocrystalline amorphous ribbons Fe _{73.5} Cu ₁ Nb ₃ Si _{13.5} B ₉ at the heating rate of 10 to 50°C/min	71
Figure 4.4(a)	Kissinger's plot to determine the activation of Fe(Si) phase for Fe _{73.5} Cu ₁ Nb ₃ Si _{13.5} B ₉ alloy	73
Figure 4.4(b)	Kissinger's plot to determine the activation of Fe ₂ B phase for Fe _{73.5} Cu ₁ Nb ₃ Si _{13.5} B ₉ alloy	74
Figure 4.5(a)	DTA trace of as-cast nanocrystalline amorphous ribbon Fe _{73.5} Au ₁ Nb ₃ Si _{13.5} B ₉ at the heating rate of 10°C/min	75
Figure 4.5(b)	DTA trace of as-cast nanocrystalline amorphous ribbon Fe _{73.5} Au ₁ Nb ₃ Si _{13.5} B ₉ at the heating rate of 20°C/min	76

Figure 4.5(c)	DTA trace of as-cast nanocrystalline amorphous ribbon $\text{Fe}_{73.5}\text{Au}_1\text{Nb}_3\text{Si}_{13.5}\text{B}_9$ at the heating rate of $30^\circ\text{C}/\text{min}$	76
Figure 4.5(d)	DTA trace of as-cast nanocrystalline amorphous ribbon $\text{Fe}_{73.5}\text{Au}_1\text{Nb}_3\text{Si}_{13.5}\text{B}_9$ at the heating rate of $40^\circ\text{C}/\text{min}$	77
Figure 4.5(e)	DTA trace of as-cast nanocrystalline amorphous ribbon $\text{Fe}_{73.5}\text{Au}_1\text{Nb}_3\text{Si}_{13.5}\text{B}_9$ at the heating rate of $50^\circ\text{C}/\text{min}$	77
Figure 4.6	Effects of heating rate on DTA traces of nanocrystalline amorphous ribbon with composition $\text{Fe}_{73.5}\text{Au}_1\text{Nb}_3\text{Si}_{13.5}\text{B}_9$ at the heating rate of 10°C to $50^\circ\text{C}/\text{min}$	78
Figure 4.7(a)	Kissinger's plot to determine the activation of Fe(Si) phase for $\text{Fe}_{73.5}\text{Au}_1\text{Nb}_3\text{Si}_{13.5}\text{B}_9$ alloy	79
Figure 4.7(b)	Kissinger's plot to determine the activation of Fe_2B phase for $\text{Fe}_{73.5}\text{Au}_1\text{Nb}_3\text{Si}_{13.5}\text{B}_9$ alloy	80
Figure 4.8(a)	DTA trace of as-cast nanocrystalline amorphous ribbon $\text{Fe}_{73.5}\text{Ag}_1\text{Nb}_3\text{Si}_{13.5}\text{B}_9$ at the heating rate of $10^\circ\text{C}/\text{min}$	81
Figure 4.8(b)	DTA trace of as-cast nanocrystalline amorphous ribbon $\text{Fe}_{73.5}\text{Ag}_1\text{Nb}_3\text{Si}_{13.5}\text{B}_9$ at the heating rate of $20^\circ\text{C}/\text{min}$	81
Figure 4.8(c)	DTA trace of as-cast nanocrystalline amorphous ribbon $\text{Fe}_{73.5}\text{Ag}_1\text{Nb}_3\text{Si}_{13.5}\text{B}_9$ at the heating rate of $30^\circ\text{C}/\text{min}$	82
Figure 4.8(d)	DTA trace of as-cast nanocrystalline amorphous ribbon $\text{Fe}_{73.5}\text{Ag}_1\text{Nb}_3\text{Si}_{13.5}\text{B}_9$ at the heating rate of $40^\circ\text{C}/\text{min}$	82
Figure 4.8(e)	DTA trace of as-cast nanocrystalline amorphous ribbon $\text{Fe}_{73.5}\text{Ag}_1\text{Nb}_3\text{Si}_{13.5}\text{B}_9$ the heating rate of $50^\circ\text{C}/\text{min}$	83
Figure 4.9	Effects of heating rate on DTA traces of nanocrystalline amorphous ribbon with composition $\text{Fe}_{73.5}\text{Ag}_1\text{Nb}_3\text{Si}_{13.5}\text{B}_9$ at the heating rate of 10°C to $50^\circ\text{C}/\text{min}$	83
Figure 4.10(a)	Kissinger's plot to determine the activation of Fe(Si) phase for $\text{Fe}_{73.5}\text{Ag}_1\text{Nb}_3\text{Si}_{13.5}\text{B}_9$ alloy	85
Figure 4.10(b)	Kissinger's plot to determine the activation of Fe_2B phase for $\text{Fe}_{73.5}\text{Ag}_1\text{Nb}_3\text{Si}_{13.5}\text{B}_9$ alloy	85
Figure 4.11	XRD spectra of $\text{Fe}_{73.5}\text{Cu}_1\text{Nb}_3\text{Si}_{13.5}\text{B}_9$ alloys of annealed at	91

	different temperatures at constant annealing time 30 min	
Figure 4.12	Change of Si (at. %) content and Lattice Parameter with different annealing temperature for the sample with composition $\text{Fe}_{73.5}\text{Cu}_1\text{Nb}_3\text{Si}_{13.5}\text{B}_9$	92
Figure 4.13	Change of Grain Size with different annealing temperature for the sample with composition $\text{Fe}_{73.5}\text{Cu}_1\text{Nb}_3\text{Si}_{13.5}\text{B}_9$	93
Figure 4.14	XRD spectra of $\text{Fe}_{73.5}\text{Au}_1\text{Nb}_3\text{Si}_{13.5}\text{B}_9$ alloys of annealed at different temperature at constant annealing time 30 min	95
Figure 4.15	Change of Si (at %) content and Lattice Parameter with different annealing temperature for the sample with composition $\text{Fe}_{73.5}\text{Au}_1\text{Nb}_3\text{Si}_{13.5}\text{B}_9$	96
Figure 4.16	Change of Grain Size with different annealing temperature For the sample with composition $\text{Fe}_{73.5}\text{Au}_1\text{Nb}_3\text{Si}_{13.5}\text{B}_9$	96
Figure 4.17	XRD spectra of $\text{Fe}_{73.5}\text{Ag}_1\text{Nb}_3\text{Si}_{13.5}\text{B}_9$ alloys of annealed at different temperature at constant annealing time 30 min	99
Figure 4.18	Change of Si (at %) content and Lattice Parameter with different annealing temperature for the sample with composition $\text{Fe}_{73.5}\text{Ag}_1\text{Nb}_3\text{Si}_{13.5}\text{B}_9$	100
Figure 4.19	Change of Grain Size with different annealing temperature For the sample with composition $\text{Fe}_{73.5}\text{Ag}_1\text{Nb}_3\text{Si}_{13.5}\text{B}_9$	100
Figure 4.20	Field dependence magnetization of amorphous ribbons with Fe-X-Nb-Si-B [X = Cu,Au and Ag] alloy at room temperature.	102
Figure 4.21	Field dependence on specific magnetization of as-cast sample of Fe-X-Nb-Si-B [X=Cu,Au and Ag] alloy at room temperature.	103
Figure 4.22(a)	Temperature dependence of specific magnetization of amorphous nanocrystalline ribbons with composition $\text{Fe}_{73.5}\text{Cu}_1\text{Nb}_3\text{Si}_{13.5}\text{B}_9$ alloy	104

Figure 4.22(b)	Temperature dependence of specific magnetization of amorphous nanocrystalline ribbons with composition $\text{Fe}_{73.5}\text{Au}_1\text{Nb}_3\text{Si}_{13.5}\text{B}_9$ alloy	105
Figure 4.22(c)	Temperature dependence of specific magnetization of amorphous nanocrystalline ribbons with composition $\text{Fe}_{73.5}\text{Ag}_1\text{Nb}_3\text{Si}_{13.5}\text{B}_9$ alloy	105
Figure 4.23(a)	dM/dt versus temperature curve of amorphous nanocrystalline ribbons with composition $\text{Fe}_{73.5}\text{Cu}_1\text{Nb}_3\text{Si}_{13.5}\text{B}_9$	106
Figure 4.23(b)	dM/dt versus temperature curve of amorphous nanocrystalline ribbons with composition $\text{Fe}_{73.5}\text{Au}_1\text{Nb}_3\text{Si}_{13.5}\text{B}_9$	107
Figure 4.23(c)	dM/dt versus temperature curve of amorphous nanocrystalline ribbons with composition $\text{Fe}_{73.5}\text{Ag}_1\text{Nb}_3\text{Si}_{13.5}\text{B}_9$	108

List of Tables

Table. No	Descriptions	Page No
Table 2.1	Spontaneous and room temperature magnetizations, magnetic dipole moments and Curie temperature for elemental ferromagnets	44
Table 4.1	Onset temperature of 1 st and 2 nd crystallization states of the nanocrystalline amorphous ribbons with composition Fe-X-Nb-Si-B [X = Cu, Au and Ag] alloy during continuous heating rate 50 ⁰ C/min	67
Table 4.2	Effect of heating rate on 1st and 2nd crystallization states of the nanocrystalline amorphous ribbon with composition Fe _{73.5} Cu ₁ Nb ₃ Si _{13.5} B ₉	72
Table 4.3	Effect of heating rate on 1st and 2nd crystallization of the nanocrystalline amorphous ribbon with composition Fe _{73.5} Cu ₁ Nb ₃ Si _{13.5} B ₉ state's calculative data for activation energy calculation data.	73
Table 4.4	Effect of heating rate on 1st and 2nd crystallization states of the nanocrystalline amorphous ribbon with composition Fe _{73.5} Au ₁ Nb ₃ Si _{13.5} B ₉	78
Table 4.5	Effect of heating rate on 1st and 2nd crystallization of the nanocrystalline amorphous ribbon with composition Fe _{73.5} Au ₁ Nb ₃ Si _{13.5} B ₉ state's calculative data for activation energy calculation data.	79
Table 4.6	Effect of heating rate on 1 st and 2 nd crystallization states of the nanocrystalline amorphous ribbon with composition Fe _{73.5} Ag ₁ Nb ₃ Si _{13.5} B ₉	84
Table 4.7	Effect of heating rate on 1 st and 2 nd crystallization of the nanocrystalline amorphous ribbon with composition Fe _{73.5} Ag ₁ Nb ₃ Si _{13.5} B ₉ for activation energy calculation data.	84
Table 4.8	crystallization states (heating rate 20 ⁰ C/min) and activation energy of different phases of nanocrystalline amorphous ribbons with composition Fe-X-Nb-Si-B [X = Cu, Au and Ag]	86

Table 4.9	Experimental XRD data of nanocrystalline $\text{Fe}_{73.5}\text{Cu}_1\text{Nb}_3\text{Si}_{13.5}\text{B}_9$ for different annealing temperature	92
Table 4.10	Experimental XRD data of nanocrystalline $\text{Fe}_{73.5}\text{Au}_1\text{Nb}_3\text{Si}_{13.5}\text{B}_9$ amorphous ribbon at different annealing temperatures	96
Table 4.11	Experimental XRD data of nanocrystalline $\text{Fe}_{73.5}\text{Ag}_1\text{Nb}_3\text{Si}_{13.5}\text{B}_9$ amorphous ribbon at different annealing temperatures	98
Table 4.12	Curie temperature and saturation magnetization of nanocrystalline amorphous ribbons with Fe-X-Nb-Si-B [X= Cu, Au and Ag] alloys	103

List of Symbols

a_0	=	Lattice parameter
B	=	Magnetic induction
D_g	=	Grain size
DTA	=	Differential Thermal Analysis
DSC	=	Differential Scanning Calorimetry
d	=	Average diameter
FWHM	=	Full Width at Half Maximum
H	=	Magnetic field
H_c	=	Coercivity
H_a	=	Applied magnetic field
$[hkl]$	=	Miller Indices
k	=	Magnetic hardness parameter
K_B	=	Boatman's constant
K_{eff}	=	Effective magnetic anisotropy constant
L	=	Self inductance of the sample core
L_o	=	Inductance of the winding coil without sample
L_{ex}	=	Ferromagnetic exchange length
M	=	Magnetization
M_s	=	Saturation magnetization
nm	=	nanometer
NM	=	Nobel metal
RAM	=	Random anisotropy model
RDF(r)	=	Radial Distribution Function
S	=	Total spin angular momentum
T_{ij}	=	Exchange interaction between atoms at the position r_i and r_j .
TTT	=	Temperature, time & transformation
T_a	=	Annealing temperature
T_c	=	Curie temperature
T_g	=	Glass transition temperature
T_x	=	Crystallization temperature
T_m	=	Melting point temperature

T_{x_1}	=	Primary crystallization temperature
T_{x_2}	=	Secondary crystallization temperature
T_{p_1}	=	Primary crystallization peak temperature
T_{p_2}	=	Secondary crystallization peak temperature
VSM	=	Vibrating Sample Magnetometer
XRD	=	X-ray diffraction
μ	=	Permeability
λ	=	Wave length
θ	=	Scattering angle
t_0	=	Time constant
β	=	Heating rate
δ_w	=	Domain wall Width
σ	=	Effective stress
$\rho(r)$	=	Atomic density
$\langle K \rangle$	=	Average anisotropy
T_c^{am}	=	Curie temperature of residual amorphous matrix
ΔH	=	Enthalpy of crystallization
ΔE	=	Activation Energy

CHAPTER I

INTRODUCTION

CHAPTER II

THEORETICAL BACKGROUND

CHAPTER III

EXPERIMENTAL DETAILS

CHAPTER IV

RESULTS AND DISCUSSION

CHAPTER V

CONCLUTIONS

REFERENCES

INTRODUCTION

1.1 Introduction

The nanotechnology has its roots date back to a 1959 talk given by Richard Feynman (<http://nano.xerox.com/nanotech/feyman.html>) in which he said, “The principles of Physics, as far as I can see, do not speak against the possibility of maneuvering things atom by atom. It is not an attempt to violet any laws; it is something in principle, that can be done; but practice it has not been done because we are too big”. But with the tremendous advancement of science and technology for the last two decades the idea that we should be able to economically arrange atoms in most of the ways permitted by physical law has gained fairly general acceptance. To the general understanding of the magnetic properties of amorphous and nanocrystalline materials the development of nanocrystalline materials for soft magnetic application is an emerging field. The new field based on nonmaterial’s has been named as nanotechnology and emerged as a new branch of science and technology.

The enhancement of soft magnetic properties require reduction of crystalline grain sizes to a much smaller length scale that can overcome the anisotropy effects and result in an improved soft magnetic behavior. This needs for a look into ‘Nanoscience’ which has made immense program in previous respect within the last decades. Research interest in the study of soft magnetic nanostructured materials has been increasing at an accelerating rate, stimulated by recent advances in materials and synthesis and characterization technique and the realization that these materials exhibit many unique and interesting physical, optical, magnetic and chemical properties with a number of potential technological applications [1.1-1.6]. Nowadays the attempts to understand different properties of materials on a smaller and smaller length scale are marking footsteps for development of research in many areas of material science. With the reduction of size into nanometer range the materials exhibit interesting properties including physical, chemical, mechanical, magnetic and electrical comparing to conventional coarse grained counterparts.

The nanocrystalline structures which substantially improve the magnetic properties of Fe-Cu-Nb-Si-B or Fe-Zr-B types alloys is presently attracting much

interest [1.7-1.8]. In this structure the particle diameter is less than 20 nm and the crystallization from the amorphous phase produces the fine structure of a bcc iron based solid solution. The properties of the isolated grains are consolidated to form nanostructural materials the magnetic properties are largely determined by the grain size and the exchange interaction between the adjacent grains [1.9]. Amorphous alloys provide an extremely convenient-precursor material for preparation of nanocrystals through the crystallization process controlled by thermal treatments [1.1-1.13].

In 1988 Yoshizawa, Oguma and Yamauchi at Hitachi metals Ltd developed the first nanocrystalline ultra soft magnetic alloy called FINEMET having composition $Fe_{73.5} Nb_3 Cu_1 Si_{13.5} B_9$ from the Fe-Si-B amorphous alloys to which addition of Cu and Nb were added [1.14]. The Cu and Nb additives play a key role in the formation of the nanocrystalline state Cu by multiplying the nucleation centres and Nb by inhibition the grain growth [1.15]. The annealing parameters (time, temperature and atmosphere) must be controlled and the nanocrystalline state can be obtained after conventional annealing under vacuum or atmosphere for typically 1h at $> 550^{\circ}C$.

The FINEMET consists of a two phase microstructure in its optimally annealed condition. The microstructure is made up of a ferromagnetic bcc α -Fe (Si) phase and /or Do_3 type of ordered Fe (Si) phase with grain size of 10-15nm embedded in this residual ferromagnetic amorphous matrix of about 1-2nm thickness .These represent a new family of excellent soft magnetic core materials and have stimulated an enormous research activity due to their potential applications [1.16 -1.18]. Müller *et. al.* [1.19] studied the influence of Cu/Nb content and annealing condition on the microstructure and the magnetic properties of FINEMET alloys. Grain size, phase composition and transition temperature were observed to depend on the Cu/Nb content.

Over the past several decades, amorphous and more recently nanocrystalline materials have been investigated for applications in magnetic devices requiring magnetically soft materials such as transformers, inductive devices, etc. Most recently, research interest in nanocrystalline soft magnetic alloys has dramatically increased. This is due, in part, to the properties common to both amorphous and crystalline materials and the ability of these alloys to compete with their amorphous and crystalline counterparts. The benefits found in the nanocrystalline alloys stem

from their chemical and structural variations on a nanoscale which are important for developing optimal magnetic properties.

The term 'nanocrystalline alloy' will be used for those alloys that have a majority of grain diameters in the typical range from 10 - 100nm. This term will include alloys made by rapid solidification, deposition techniques and solid state reactions where the initial material may be in the amorphous state and subsequently crystallized. These are considered processing routes and methods to control chemistry and microstructural morphology on increasingly smaller length scales, and various developing experimental techniques which allow more accurate and quantitative probes of structure on smaller length scales. Review the impact of microstructural control on the development of state of the art of soft magnetic materials.

Nanocrystalline soft magnetic materials constitute a new class of condensed matter having interesting properties, which are mostly microstructure dependent. These materials are first formed into amorphous ribbons and then annealed above the crystallization temperature to form the nanocrystalline microstructure that consists of bcc-Fe(Si) nanograins embedded in an amorphous matrix. Excellent soft magnetic properties can be found in these nanocrystalline materials obtained by the controlled crystallization of Fe-Si-B amorphous ribbon containing Cu and Nb.

The addition of Cu and Nb results in the formation of an ultrafine grain structure. Cu is used as a nucleating agent for the growth of nanocrystals while Nb inhibits their growth. Therefore the appropriate amount of Cu and Nb are very important for controlling the crystallization behavior of FINEMET type amorphous alloys. Instead of Nb other refractory elements such as Ta, Mo, can be used [1.20] while Au and Ag can be used instead of Cu [1.21-1.22]. Crystallization behavior and grain size are very much correlated with the magnetic properties.

The theoretical understanding of the nonmetric grain with magnetic softness has been consolidated in the light of the random anisotropy model (RAM) as proposed by Alben *et. al.*[1.23], on the basis of RAM showed that extraordinary soft magnetic properties of nanocrystalline materials arise due to strong inter granular magnetic coupling, the suppression of effective magnetocrystalline anisotropy and vanishing magnetostriction. The magnetocrystalline anisotropy vanishes when the grain size is smaller than the ferromagnetic exchange length and magnetostriction goes towards zero due to the cancellation of the positive magnetostriction of α -Fe(Si) crystallites and negative magnetostriction of the amorphous matrix. The aim of the present work

is to study phase to the remaining amorphous and nanocrystalline phase, where the remaining of the amorphous phase crystallites increased significantly compared with crystallization temperature of the Cu-free alloy. The quantity of nanocrystalline phase, which can be formed at given temperature, depends on the FINEMET alloy replace Cu by Au or Ag. Not only the promising technological application but also the coexistence of various magnetic phases at elevated temperature makes than attractive for studding basic magnetic phenomena.

1.2 The Aim and Objective of Present Work

The main objectives of the present work is to investigate Fe-X-Nb-Si-B [X = Cu, Au & Ag] nanocrystalline ribbon and to study the phase constitution and magnetic properties for the composition $Fe_{73.5}X_1Nb_3Si_{13.5}B_9$ [X = Cu, Ag & Au] that's find out the optimum composition and grain distribution affecting the magnetic properties of the system.

The objectives of the research work as follows:

- Synthesis of the FINEMET alloys in the form of the ribbon with replacement Cu with Au or Ag in amorphous state by rapid solidification technique.
- Growth of nanocrystals on amorphous matrix by thermal treatment.
- The formation nanocrystals grain size distribution as affected by heat treatment with varying temperature and holding time will be studied by XRD.
- Correlation of the evaluation of nanograins with the magnetic properties
- Optimization of annealing temperature corresponding to the magnetization of this nanocrystalline ribbon.

1.3 Experimental Reason for Choosing this Research Works

In the present work, soft magnetic amorphous FINEMET type alloy nominal composition of $Fe_{73.5}X_1Nb_3Si_{13.5}B_9$ [X= Cu, Ag & Au] has been prepared by a melt spinning technique. To improve the magnetic properties of this amorphous ribbon microstructure is an important parameter that can be controlled by heat treatment condition.

In this research work the kinetics of crystallization amorphous FINEMET type alloys were investigated by the use of Differential Thermal Analysis (DTA) and X-ray

Diffraction (XRD) techniques. The combination of these two techniques is necessary for the complete description of the processes occurring during the nanocrystallization from amorphous precursors as well as micro structural evolution in FINEMET type alloys in its crystalline state, Results have been aid in interpreting the effect of heat treatment on magnetic properties and application type of alloys. Optimum annealing temperature would be ascertained through isothermal annealing over a wide range of temperature. An estimation of the volume fraction of the nanocrystalline Fe-Si phase has been ascertained from the thermo magnetic measurement depending on the annealing temperature.

The optimum heat treatment will be found out by trial and error to obtain nanocrystalline phase in a minority amorphous matrix. Amorphousity of the samples will be checked by X-Ray diffraction (XRD). A nanocrystallization of the amorphous samples would be realized upon isothermal annealing based on the knowledge of crystallization temperature obtain from differential thermal analysis (DTA). DTA will be used to evaluate the phase transformation and to determine the crystallization temperature. From DTA analyzing evaluation of the crystallization activation energy of various phases will be done. Crystalline phase size of crystallites will be determining X-Ray diffractometer on samples annealed at different temperature. All the annealing heat treatment would be performed in evaluated quartz tube in conjunction with a microprocessor controlled muffle furnace. Crystallization products will be determined by XRD. Thermomagnetic measurements will be performed to see the crystallization behavior of the amorphous ribbons and will be compared with other measurements such as DTA and XRD. Magnetization will be performed using vibrating sample magnetometer (VSM).

Magnetization of the sample has been measured as a function of field and temperature. The Curie temperature has been determined by specific magnetization versus temperature measurements with the help of oven using VSM. Finally it has been shown Cu replaced by Au and Ag substituted Fe-based nanocrystalline alloys of the above mentioned composition in the amorphous states by using rapid solidification technique and their magnetic properties with the evolution of different phases by verifying annealing condition. The experimental result has been analyzed and interpreted theoretically.

1.4 Application of Nanocrystalline Ribbons

Early discoveries of magnetic amorphous metallic glasses, their promise for soft magnetic applications has continued to be exploited. Soft magnetic ribbons produced by rapid quenching from the melt are already used in the industrial uses practices. Magnetic properties of specific composition greatly profit from the thermal treatment that leads to partial crystallization where nanoscale crystalline grain are embedded in the amorphous of the alloy. Recently, however, a revolution in the understanding of magnetic properties on a nanoscale and the discovery of exciting new nanocrystalline magnetic materials has led to be vital for application of these soft magnetic materials. It appears that a significant need for state of the art application of soft magnetic materials will include high temperature performance of soft magnetic materials.

Nanocrystallization of amorphous precursors has also required compaction to produce shapes and to improve mechanical properties as ribbon is quite brittle after nanocrystallization. Fe based nanocrystalline ribbons can be used to replace silicon steel, permalloy and ferrites. These are excellent materials to make transformers core for high frequency switch mode power supplies, current transformer cores, transformer cores for ground –fault-interrupters, cores for filters, storage inductors, and reactors, EMC common modes chokes ,sensor cores, cores for saturable reactors, magnetic amplifiers, beads ,and pulse compressors.

The soft magnetic properties required for rotor applications in more electric aircraft are in some senseless restrictive than those for the application of FINEMET. Permeability of 10^2 - 10^3 are sufficient for this application. The frequency requirements, based on 104 rpm rotor speeds and 6 flux changes per cycle, require this permeability to only 1 KHz.

The more electric aircraft integrated power unit (MEA-IPU) is a specific example of a component in which bulk magnets, both hard and soft are important. Such materials are critical to power generation, in power inversion (transformer), in magnetic bearing and magneto actuators. In the MEA-IPU, soft Fe-Co alloy laminate stakes are incorporated in the rotor and hard magnets in the IPU bearings. Operation of the IPU at the high temperatures associated with air cooling requires materials with excellent high temperature magnetic and mechanical properties. Realization of these exciting potentials will require:

- (i) Development of high permeability, large saturation and remnant induction, low loss, hysteresis and eddy current for soft magnets of operating at high temperature.
- (ii) Development of high energy product permanent magnets capable at operating at high temperatures.
- (iii) Improved mechanical properties and corrosion resistance at higher operating temperatures.
- (iv) Development of new magnetic device geometries which exploit the materials.

Nanocrystalline materials have no microstructural discontinuities such as dislocations, grain boundaries or precipitates. This significantly reduces the possible spinning sites for domain walls, reducing the coactivity.

1.5 Review of Research on FINEMET

Amorphous materials based on Fe-Si-B show good magnetic properties when they are heat treated below their crystallization temperature. While the Fe-Cu-Nb-Bi-B alloys exhibit extraordinary high permeability, two orders of magnitude higher than their conventional Fe-Si-B alloys due to heat treatment just above the crystallization temperature for a specific time. The great scope of technical application of this material $\text{Fe}_{73.5}\text{Cu}_1\text{Nb}_3\text{Si}_{13.5}\text{B}_9$ arises from this freedom of tailoring the magnetic properties [1.22-1.23]. The pioneer alloy composition of $\text{Fe}_{73.5}\text{Cu}_1\text{Nb}_3\text{Si}_{13.5}\text{B}_9$ known as FINEMET has been studied due to its novel magnetic properties.

The study of Yoshizawa *et. al.*[1.26] on the role of nucleating Cu on the crystallization behavior of the composition FINEMET revealed that the average grain size is relatively large at crystallization temperature due to lower crystallization rate with no addition of Cu and annealing of this Cu free alloy leads to simultaneous or sequential formation of several crystalline phase. Noh *et. al.*[1.27] studied the effect of Cu on the crystallization behavior in $\text{Fe}_{74.5-x}\text{Cu}_x\text{Nb}_3\text{Si}_{13.5}\text{B}_9$ for $x = 0$ and $x = 1$. The crystallization behavior of this $x = 0$ is quite different and leads to a severe degradation of the soft magnetic properties compare to the original amorphous state. They also found that the average grain size just after the onset of crystallization is relatively large up to about 60nm with broad scattered and show a distinct variation with the annealing temperature. This indicates the significantly lower nucleation rate

than in the Cu-doped alloy whose finer grain size is almost constant in wide range of annealing temperature. Mondal *et. al.* [1.28] shows a small Cu addition yields two clearly separated crystallization peaks corresponding to the primary crystallization of bcc Fe at T_{x_1} and subsequently to the precipitation of Fe-B compound at T_{x_2} .

Magnetic and structural properties of FINEMET alloy and with the substitution of Nb by Ta, Mo and Cr, W has been studied by several investigation [1.29-1.39]. Result show that FINEMET composition with Nb and Ta show similar soft characteristics while alloy with substitution of Nb and Cr, Mo and W display somewhat lower soft magnetic properties. Hakim *et. al.* [1.31] found with the Ta substituted alloy super paramagnetic and super ferromagnetic behavior depending upon the volume fraction of the nanocrystallinities from the temperature dependence of the permeability of the samples annealed in the temperature range 500⁰C - 575⁰C. Similar behavior of super paramagnetic has been observed in the FINEMET alloy with higher content of Cr content substituted for Fe [1.32-1.35].

Magnetic properties of partial substitution of Fe by Cr have been studied by several investigators with a limited concentration of Cr between 1 to 5 at % substitution for Fe in the FINEMET alloy [1.36-1.38]. The author found that Cr enhances the crystallization temperature, controls the volume fraction and particle size of α -Fe (Si) phase and reduces the Curie temperature. The influence of Cr-content with higher percentage of Cr on the magnetization behavior of Fe_{73.5-x}Cr_xCu₁Nb₃Si_{13.5}B₉ alloys have been studied [1.39]. It has been found that magnetic moment and the T_c decreases linearly with Cr-concentration.

Müller *et. al* [1.40] showed that like Nb, the atomic volume of the refractory element grows V or VI (Cr, V, Mo, W or Ta) are larger than that of Fe that reduces diffusion co-efficient and thus stabilizes the amorphous matrix and slows down the for grain size refinement increases in the order of their atomic volume i.e. Cr < V < Mo \approx W < Nb \approx Ta. Thus, finest grain structures and superior magnetic properties require a certain amount of elements Nb and Ta.

Inoue *et. al.* [1.41] observed that group V (a) or VI (a) transition metals extend the glass forming range at low S or B contents. The glass forming range is the widest for Hf containing alloys and decreases in order Zr > Nb \approx Ta > Mo \approx W > V > Cr. According to Suzuki *et. al.* [1.42-1.43] the glass forming ability is considerably improved with the addition of Hf or Zr.

Franco *et. al* [1.44] also studied the super magnetic relaxation in FINEMET type of alloy Fe-Cu-Nb-Si-B without adding any extra refractory element and they have demonstrated that this behavior is a general characteristics of this nanocrystalline alloys provided the volume fraction of crystallites are very low. If the size of the nanocrystals is small enough and intergranular amorphous matrix is sufficiently thick to minimize the magnetic interactions between them, the super paramagnetic behavior of the nanocrystalline particles is expected.

Ayer's *et. al* [1.45] reported that the presence of Nb promotes the formation of Cu rich clusters on a much finer scale than in Nb free alloy composition. Small grain size is required for good soft magnetic properties, but at the same time needs to maintain the absence of boron compounds. Herzer [1.46] reported that the separation between the primary crystallization to bcc Fe and precipitation of Fe-B compounds decreases with increasing boron content. So it is necessary to keep the boron concentration at a low or moderate level in order to obtain an optimum nanoscale structure.

Kubaschewski [1.47] showed that the thermodynamically equilibrium boron is practically insoluble in bcc Fe ($\ll 0.01$ at %); the solubility's of Cu and Nb are low; < 0.2 at % Cu < 0.1 at% Nb they also found that the average grain size just after the onset of crystallization is relatively large up to about 60 nm with a broad scatter and show a distinct variation with the annealing temperature. This indicates the signifying lower nucleation rate than in the Cu-doped alloy whose finer grain size is almost constant in a wider range of annealing temperature [1.48] containing efforts to improve the soft magnetic properties of FINEMET alloy have been made of modifying the alloy compositions. Ohnuma *et. al* [1.49] reported that the substitution of Fe by Co decreases the saturation magnetization in FINEMET type amorphous alloys. The magneto crystalline anisotropy of the small randomly oriented grains is averaged out of exchange integration.

Replacement of Cu by Au and Ag in the FINEMET with composition $Fe_{73.5}Cu_1Nb_3 Si_{13.5} B_9$ alloy on the crystallization behavior and magnetic properties is observed. In these materials it has been determined that an important averaging of the nanocrystalline anisotropy over many grains coupled within an exchange length is at the root of magnetic softness of these materials. The crystallization kinetics and chemical partitioning occurring during crystallization will be described essentially. The effect of replacement Cu by Au and Ag in FINEMET nanograin structure and

thermal stability of the alloy draws much interest for the present research from the view point of applications.

1.6 Organization of the Thesis

The thesis has been divided into six chapters.

Chapter I general introduction followed by the aim and objectives of the present work, reason for choosing on FINEMET and organization of the thesis.

Chapter II the theoretical background of the stability of amorphous alloys, theories of nanocrystalline substance and magnetization are discussed.

In chapter III, the preparation procedures of the nanocrystalline samples, experimental details including differential thermal analysis (DTA), X-ray diffraction (XRD) and vibrating sample magnetometer.

In Chapter IV, the details results regarding DTA, activation energy corresponding crystallization temperature, XRD method after heat treatment of the sample at different temperature, Field and temperatures dependence of specific magnetization are discussed and

Chapter V, contains conclusion and further suggestion of this work.

Finally a complete list of reference and publication has been given towards the end of this chapter.

EXPERIMENTAL DETAILS

3.1 Methods Used for Preparation of Nanocrystalline Alloy

There are various techniques in use to produce a metallic alloy in an amorphous state whose the atomic arrangement has no long range periodicity. The different experimental techniques developed to produce amorphous metallic glass can be classified into two groups:

- (i) The atomic deposition methods
- (ii) The fast cooling of the melt

As we know, controlled crystallization from the amorphous state is the only method which presently available to synthesize nanocrystalline alloys with superior soft magnetic properties. In this thesis work amorphous ribbons have been prepared by fast cooling of the melt.

3.1.1 The Fast Cooling of the Melt

For producing an amorphous state by any of the liquid quenching devices, the molten alloy must be cooled through the temperature range from the melting temperature (T_m) to the glass transition temperature (T_g) very fast allowing no time for crystallization. The factors controlling T_g and crystallization are both structural and kinetic. Atomic arrangement, bonding and atomic size effects are related in the structural factors. The structural factors as discussed Turnbull [3.1] are the nucleation, crystal growth rate and diffusion rate compared to the cooling rate. The interest in this method stems from the wide variety of alloys that can be made as well as from the potential low cost of preparation. In the pioneering work Duwez *et. al* [3.2], number of devices has been reported for obtaining the necessary high quenching rates and producing continuous filaments. The methods using the principle of fast cooling of melt techniques are:

- (i) The gun techniques
- (ii) Single roller rapid quenching techniques
- (iii) Double roller rapid quenching techniques
- (iv) Centrifuge and rotary splat quencher techniques
- (v) Torsion catapult techniques
- (vi) Plasma-jet spray techniques
- (vii) Filamentary casting techniques

- (viii) Melt extraction techniques
- (ix) Free-jet spinning techniques
- (x) The melt spinning techniques

Although the different methods used in preparing amorphous metallic ribbons are mentioned here, only the single roller rapid quenching technique, which is widely used to prepare the amorphous ribbons.

3.1.2 Sample for Master Alloy Preparation

Amorphous ribbons with the nominal composition $\text{Fe}_{73.5}\text{X}_1\text{Nb}_3\text{Si}_{13.5}\text{B}_9$ [X = Cu, Ag & Au] were prepared in an arc furnace on a water-cooled copper hearth under an atmosphere of pure Ar. Their purity and origin of the constituent elements were Fe (99.9%), Ag (99.9%), Au (99.9%), Nb (99.9%), Cu (99.9%), Si (99.9%) and B (99.9%) as obtained from Johnson Mathey (Alfa Aesar Inc.). The buttons prepared are about 50 grams each. Care is taken to ensure through mixing and homogeneity of the alloy composition, by turning over and remelting each button few times. The required amounts of the constituent elements were taken from pure metal bars or flakes, weighed carefully with a sensitive electronic balance and placed on the copper hearth inside the arc furnace. Before melting, the furnace chamber was evacuated (10^{-4} torr), and flashed with Ar gas. The process was repeated several times to get rid of residual air and finally the furnace chamber were kept in an Ar atmosphere. The mother alloys are formed in the form of buttons in a furnace by sudden cooling and is then cut into small pieces and is introduced in the quartz tube. The quartz tube is connected from the top by rubber 'O' rings and metal rings to the argon cylinder through a valve and a pressure gauge.

A substantial amount of pure Titanium getter, placed inside of the chamber on the side of the copper hearth was melted first in order to observe any oxygen present in the furnace chamber. The constituent elements were then melted in the shape of buttons. The arc melting facilities used to prepare the sample are installed at the Centre for Materials Science, National University of Hanoi, Vietnam. The arc furnace used in the preparation of master alloy is shown in Figure 3.1.

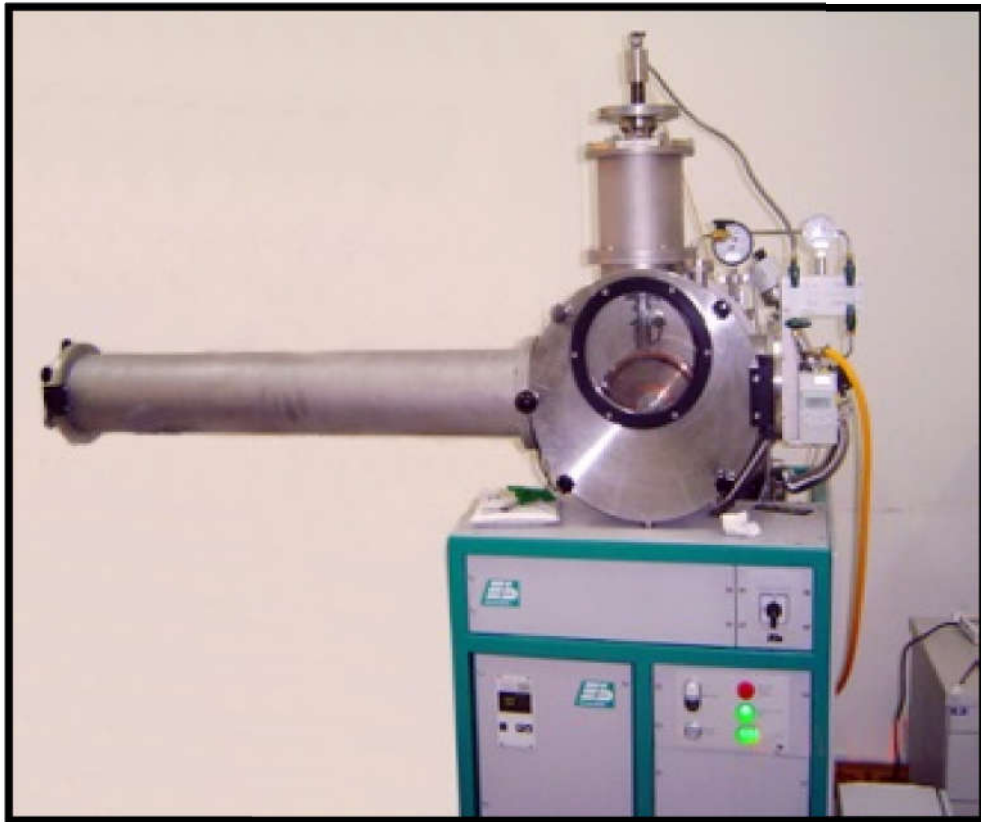


Figure 3.1 Vacuum Arc Melting Machine

3.1.3 Preparation of Ribbon by Melt Spinning Technique

Melt spinning is a widely used production method for rapidly solidifying materials as well as preparing amorphous metallic ribbon [3.3-3.4]. In order to prepare amorphous of $Fe_{73.5}X_1Nb_3Si_{13.5}B_9$ [$X = Cu, Ag \& Au$] alloys, the melt spinning facilities was used at the Centre for Materials Science, National University of Hanoi, Vietnam. After proper cleaning of the roller surface and adjusting its speed to the desired value, as measured by stroboscope the induction furnace is powered using high frequency generator. The arc melted master alloy was crashed into small pieces and put inside the quartz tube crucible for re-melting by induction furnace using a medium frequency generator with maximum power of 25kW at a nominal frequency of 10kHz. When the melting temperature is reached as observed through a protective spectacle, the injection pressure is applied by opening the pressure valve. To avoid the turbulence of the wind, arising from the high speed of the roller in disturbing the melt puddle, cotton pad and metallic shield are usually used just beneath the roller. To avoid oxidation of the ribbon during its formation an inert atmosphere can be created around the roller by a slow stream of Ar-gas.

Figure 3.2 shows schematic diagram and Figure 3.3 shows the pictorial view of the Melt-Spinning Machine. The Quartz crucible has in its bottom part, a rectangular nozzle tip of 8 mm length and 0.7 mm width. The position of the nozzle tip can be adjusted with respect to copper wheel surface, so that the molten alloy was perpendicularly ejected onto the wheel surface from a distance of about 0.3 mm. The small piece of the master alloy samples were inductively remelted inside the quartz tube crucible followed by ejecting the molten metal with an over pressure of 250 mbar of 99.9% pure Ar supplied from an external reservoir through a nozzle onto a rotating copper wheel with surface velocity of 30 m/sec. The temperature was monitored by an external pyrometer from the upper surface of the molten alloy through a quartz window.

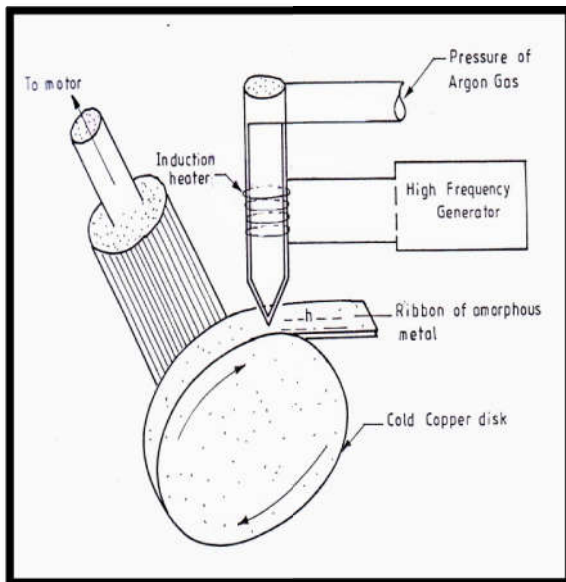


Figure 3.2 Schematic diagram



Figure 3.3 Melt-Spinning Machine

The metal alloys were ejected at a temperature of about 150 to 250 K above the melting point of the alloy. The resulting ribbon samples had thickness of about 20-25 μm and width ~ 6 mm. Processing parameters such as the thermal conductivity of the rotating quench wheel, wheel speed, ejection pressure, thermal history of the melt before ejection, distance between nozzle of quartz tube and rotating wheel, as well as processing atmosphere have influenced on the microstructure and properties of melt-spun ribbons. The lower pressure of 250 mbar as mentioned above stabilizes the turbulence between melt pull and rotating copper wheel enhancing the heat transfer resulting in a more uniform quenching. As a result, a more uniform ribbon microstructure can be obtained at relatively low wheel speed. With increasing wheel

speeds for a given ejection rate, the increasing extraction rate results in thinner ribbons. The speed of the roller, the volumetric flow rate, the orifice diameter, the substrate orifice distance, the injection angle etc. are adjusted by trial and error to get the best result in respect of the quality and geometry of the ribbons.

3.1.4 Important Factors to Control the Thickness of Ribbons

- (i) Rotating speed
 - Angular velocity $\omega = 2000\text{rev/min}$
 - Surface velocity $V = 20\text{ m/s to } 30\text{ m/s}$
- (ii) Gap between nozzle and rotating copper drum (h) = 200 to 300 μm
- (iii) Oscillations of the rotating copper drum both static and dynamic has maximum displacement 1.5 to 5 μm
- (iv) Pressure = 0.2 to 3.0 bar at argon atmosphere
- (v) Temperature of molten metal's $T_m \approx 1500^\circ\text{C}$; the temperature must not exceed 1800°C otherwise quartz tube would be melted.
- (vi) A steady flow of the molten metal's on the surface of the rotating drum needs to be ensured.

3.1.5 Confirmation of Amorphousity Ribbons

The amorphous state of the three ribbons has been confirmed by X-ray diffraction using BUKER D8 ADVANCE XRD system located at Bangladesh Council of Scientific and Industrial Research (BCSIR).

From the X-ray diffraction pattern of the samples in Figure 3.4, there have no peaks observed within the scanning range. The ribbons showed broad diffraction maximum and no low angle scattering. These ribbons were also ductile and those cases for which low angle scattering appear and the broad diffraction peak are subdued there is some presence of micro crystalline phase. Although there are few small humps shown in the diffraction pattern around $2\theta = 45^\circ$; but it cannot be regarded due to the crystalline effects. So from all the pattern of X-ray diffraction is confirmed that the samples are in pure amorphous state.

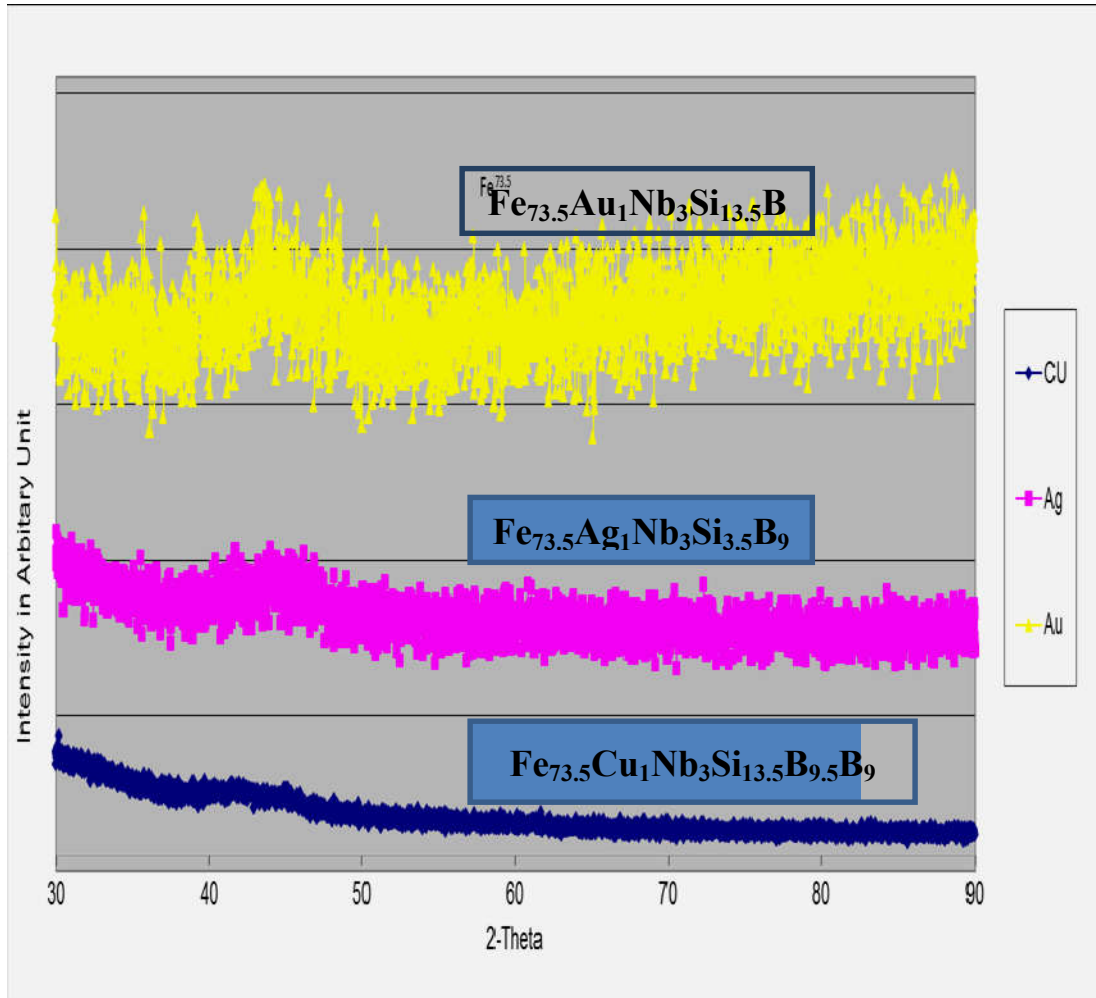


Figure 3.4 X-ray diffraction of as-cast nanocrystalline amorphous ribbons with composition $\text{Fe}_{73.5}\text{X}_1\text{Nb}_3\text{Si}_{13.5}\text{B}_9$ [X = Cu, Ag & Au]

3.2 Thermal Analysis Techniques

Thermal analysis comprises of a group of techniques in which a physical property of a substance is measured as a function of temperature, while the substance is subjected to a controlled temperature program. The Differential Thermal Analysis (DTA) is an important technique for studying the structural change occurring both in solid and liquid materials under heat treatment. These changes may be due to dehydration, transition from one crystalline variety to another, destruction of crystalline lattice, oxidation, decomposition etc. The principle of DTA consists of measuring the heat changes associated with the physical or chemical changes that occur when a standard substance is gradually heated. This technique can also be used to identify magnetic ordering of nanocrystalline amorphous ribbons. The related

technique of differential scanning calorimetry relies on difference in energy required to maintain the sample and reference at an identical temperature.

This technique has been used in determining the first crystallization temperature (T_{x_1}) and second crystallization temperature (T_{x_2}) of our nanocrystalline soft magnetic material. The first crystalline temperature is defined as the temperature at which the alloy passes from the solid to liquid state. For our study, it is sufficient to describe T_{x_1} as the temperature at which atomic mobility is great enough to allow diffusive rearrangement to occur in a matter of minutes. The crystallization temperature T_{x_2} is defined as the temperature at which crystallization occurs with long range ordering. Metallic nanocrystalline glasses ribbons usually are ductile in the as quenched condition, but may often embrittled by exposure to elevated temperature.

DTA technique have been used in determining T_{x_1} and T_{x_2} of our nanocrystalline ribbon of composition $\text{Fe}_{73.5}\text{X}_1\text{Nb}_3\text{Si}_{13.5}\text{B}_9$ [X = Cu, Ag & Au] based on Kissinger plots, crystallization activation energy of T_{x_1} and T_{x_2} phases have been evaluated.

3.2.1 The Principle of Differential Thermal Analysis

The DTA technique was first suggest by Le Chatelier [3.5] in 1887 and was applied to the study of clays and ceramics. DTA involves heating or cooling a test sample and inert reference under identical conditions, while recording any temperature difference between the sample and reference. DTA is the process of accurately measuring the difference in temperature between a thermocouple embedded in a sample and a thermocouple in a standard inert material such as aluminum oxide, while both are being heated at a uniform rate. These differences of temperature arise due to phase transition or chemical reactions in the sample involving the evolution of heat or absorption of heat due to exothermic reaction or endothermic reaction measured. The exothermic and endothermic reactions are generally shown data in the DTA trace as positive and negative deviations respectively from a baseline. Then this differential temperature is plotted against time, or against temperature. When a sample and reference substance are heated or cooled

at a constant rate under identical environment, their temperature differences are measured as a function of time or temperature as shown by the curve in Figure 3.5 (a).

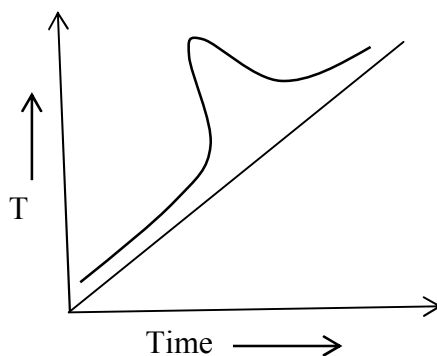


Figure 3.5(a) Heating curve of sample and reference substance

The temperature of the reference substance, which is thermally inactive, rises uniformly when heated, while the temperature of the sample under study changes anomalously when there is physical or a chemical change of the active specimen at a particular temperature. When there is an exothermic reaction there is a peak in the temperature versus time curve, heat supplied from outside is consumed by the reaction. And when the reaction is over, the sample temperature gradually catch up the temperature of the inactive specimen. The temperature difference ΔT is defined, amplified and recorded by a peak as shown in Figure 3.5 (b).

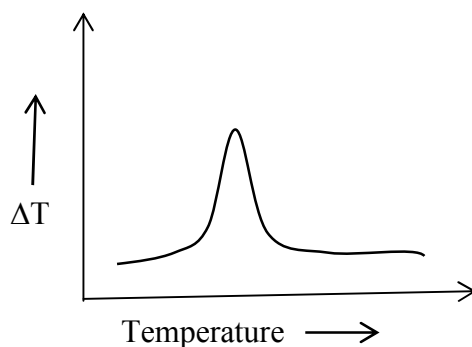


Figure 3.5(b) DTA Curve

For any endothermic reaction or change the active specimen absorbs heat which is reflected in the corresponding the trough in temperature versus time curve. Changes in the sample, which leads to the absorption or evolution of heat, can be detected relative to the inert reference. Differential temperatures can also arise between two inert samples when their response to the applied heat treatment is not identical. DTA can therefore be used to study thermal properties and phase changes which do not lead to a change in enthalpy.

Changes in the sample, either exothermic or endothermic, can be detected relative to the inert reference. Thus, a DTA curve provides data on the transformations that have occurred, such as glass transitions, crystallization, melting and sublimation. The baseline of the DTA curve showed then exhibit discontinuities at the transition temperatures and the slope of the curve at any point will depend on the microstructural constitution at that temperature. The area under a DTA peak can be related to the enthalpy change and is not affected by the heat capacity of the sample. DTA may be defined formally as a technique for recording the difference in temperature between a substance and a reference material against either time or temperature as the two specimens are subjected to identical temperature regimes in an environment either heated or cooled at a controlled rate.

3.2.2 Apparatus

The key features of a DTA kit are as shown in Figure 3.6 sample holder comprising thermocouples, sample containers and a ceramic or metallic block, a furnace, temperature programmer, recording system. The essential requirements of the furnace are that it should provide a stable and sufficiently large hot-zone and must be able to respond rapidly to commands from the temperature programmer. A temperature programmer is essential in order to obtain constant heating rates. The recording system must have a low inertia to faithfully reproduce variations in the experimental set-up.

The sample holder assembly consists of a thermocouple each for the sample and reference, surrounded by a block to ensure an even heat distribution. The sample is contained in a small crucible designed with an indentation on the base to ensure a snug fit over the thermocouple bead. The crucible may be made of materials such as Pyrex, Silica, Nickel or Platinum, depending on the temperature and nature of the tests involved. The thermocouples should not be placed in direct contact with the sample to avoid contamination and degradation, although sensitivity may be compromised. Metallic blocks are less prone to base-line drift when compared with ceramics which contain porosity. On the other hand, their high thermal conductivity leads to smaller DTA peaks. The sample assembly is isolated against electrical interference from the furnace wiring with an earthed sheath, often made of platinum-coated ceramic material. The sheath can also be used to contain the sample region within a controlled atmosphere or a vacuum.

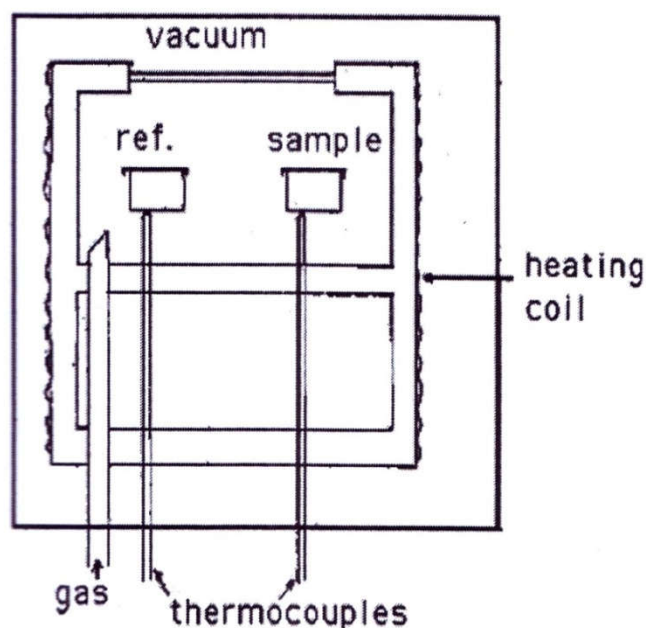


Figure 3.6 Schematic illustration of a DTA cell

The specimen holder is placed in the cavity of the heating block which is operated in the center of the cylindrical refractory tube of an electrical furnace. This supplies a uniform heating rate. The furnace is peked with calcined china clay. The input of current into the furnace is secured through the secondary of a Variac transformer, which controls the currents. Fine Chromelalumel wires (28 gauges) are used for thermocouples. A cold junction is used for thermocouple leads and the e.m.f. is recorded almost continuously, while the temperature of the inert material is measured at 3 minute intervals. It is essential to use perfectly dry materials, as otherwise errors will be introduced in the analysis. Approximately 0.1 gm anhydrous alumina is used in the reference cup and the sample weight varies over a range 0.05 to 0.125 gm; depending on their density. A heating rate of 10°C to 50°C per minute of the furnace is conveniently chosen and this gives satisfactory results in most case. A block diagram of DTA as shown in Figure 3.7

During experiments a temperature problems are encountered in transferring heat uniformly away from the specimen. These may be mitigated by using thermocouples in the form of flat discs to ensure optimum thermal contact with the new flat-bottomed sample container, made of aluminum or platinum foil. To ensure reproducibility, it is then necessary to ensure that the thermocouple and container are consistently located with respect to each other.

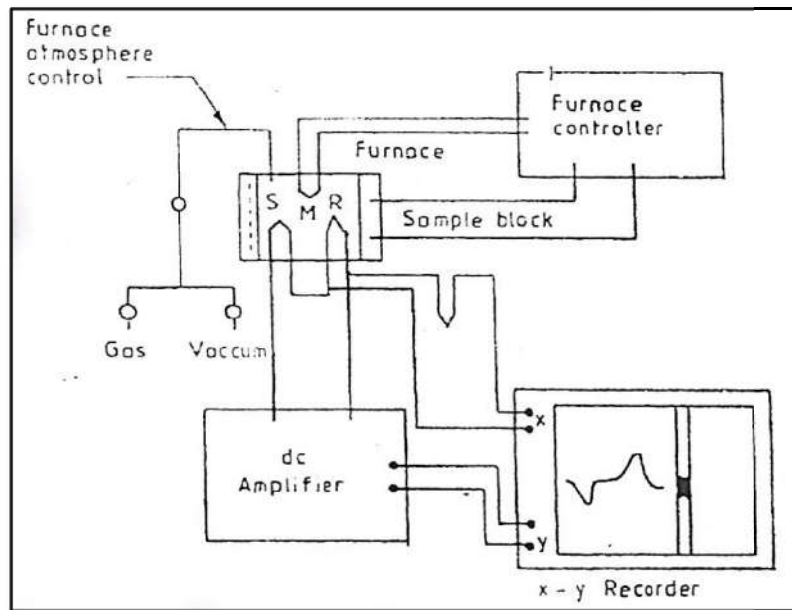


Figure 3.7 Block diagram of a DTA equipment, (S) sample thermocouple, (R) Reference thermocouple, (M) Monitor thermocouple

3.2.3 Experimental Factors

It is necessary in care to selecting the experimental parameters. For example, the effects of specimen environment, composition, size and surface to volume ratio all affect powder decomposition reactions, whereas these particular variables may not affect solid state phase changes. Experiments are frequently performed on powders so the resulting data may not be representative of bulk samples, where transformations may be controlled by the build-up of strain energy. The packing state of any powder sample becomes important in decomposition reactions and can lead to large variations between apparently identical samples.

In some circumstances, the rate of heat evolution may be high enough to saturate the response capability of the measuring system; it is better than to dilute the test sample with inert material. For the measurement of phase transformation temperatures, it is advisable to ensure that the peak temperature does not vary with sample size. The shape of a DTA peak does depend on sample weight and the heating rate used. The influence of heating rate on the peak shape and disposition can be used to advantage in the study of decomposition reactions, but for kinetic analysis it is important to minimize thermal gradients by reducing specimen size or heating rate.

3.2.4 Interpretation and Presentation of DTA

There are difficulties with the measurement of transition temperatures using DTA curves. The onset of the DTA peak in principle gives the start-temperature, but there may be temperature lags depending on the location of the thermocouple with respect to the reference and test samples or the DTA block. It is wise to calibrate the apparatus with materials of precisely known melting points. The peak area (A), which is related to enthalpy changes in the test sample, is that enclosed between the peak and the interpolated baseline. When the differential thermocouples are in thermal, but not in physical contact with the test and reference materials, it can be shown that A is given by,

$$A = \frac{mq}{gk} \quad (3.1)$$

where m is the sample mass, q is the enthalpy change per unit mass, g is a measured shape factor and k is the thermal conductivity of sample.

With porous, compacted or heaped samples, the gas filling the pores can alter the thermal conductivity of the atmosphere surrounding the DTA container and lead to large errors in the peak area. The situation is made worse when gases are evolved from the sample, making the thermal conductivity of the DTA-cell environment different from that used in calibration experiments. The DTA apparatus is calibrated for enthalpy by measuring peak areas on standard samples over specified temperature ranges. The calibration should be based upon at least two different samples, conducting both heating and cooling experiments.

In the present work, SEIKO Instruments Inc. (SII) EXSTAR 6000 TG/DTA 6300 has been used for thermal analysis shown in Figure 3.7. The Thermogravimetric/Differential Thermal Analyzer (TG/DTA) combine the flexibility of DTA with the proven capabilities of the TG measurement technology, providing property information for a variety of samples. Thus simultaneous TG/DTA System can be used for such application as oxidation, heat resistance, and the amount of water, compositional analysis and measurement of ash contents in a sample. This system is also used to cover such need as reaction rate and accelerated degrading tests.

All experiments are run at atmospheric pressure in continuous flow of purified inert gas Nitrogen. Gases are normally purged into the furnace chamber at the lower end through a purification train in which oxygen and water are removed by

heated copper wool and exhausted from the top into a condensate trap for collecting the condensable volatile products.



Figure 3.8 SII EXSTAR 6000 TG/DTA 6300 assembly

A. The Features are:

- (i) The TG/DTA can operate in either DSC or DTA mode. In DSC mode it displays heat flow signal.
- (ii) The horizontal differential balance provides high sensitivity and accuracy.
- (iii) Gas control unit automatically control the environment of the furnace between measurements.
- (iv) Auto sampler with 30 samples positions provides laboratory automation and increase productivity.
- (v) Through the utilization of an automatic cooling unit, the instrument is now automatically cooled to a set temperature after measurements, which raises the effectiveness of measurements.

B. Specification:

Temperature Range	: Room temperature to 1500°C (normally around 1300°C)
Balance Method	: Horizontal differential type

Maximal sample weight	: 200mg;
Program rate	: 0.01 to 100°C/min
Automatic Cooling unit	: Force Air Cooling
Gas flow rate	: 0 to 1000ml/min
Cooling rate	: less than 15 min from 1000 to 50°C
Atmosphere	: Air, Inert gas, Vacuum (10 ⁻² Torr)
Sample pan material	: Platinum, Alumina and Aluminum.
TG measurement Range/Sensitivity	: 200 mg /0.2µg
DTA measurement / Sensitivity	: +1000µV/ 0.06µV

3.3 Annealing

Annealing in metallurgy and materials science, is heat treatment wherein a material is altered, causing changes in its properties such as strength and hardness. It is a process that produces conditions by heating to above the critical temperature, maintaining a suitable temperature, and then cooling. Annealing is used to induce ductility, soften material, relieve internal stresses, refine the structure by making it homogeneous, and improve cold working properties.

In the cases of copper, steel, silver and brass, this process is performed by substantially heating the material (generally until glowing) for a while and allowing it to cool. Unlike ferrous metals, which must be cooled slowly to anneal, copper, silver and brass can be cooled slowly in air or quickly by quenching in water. In this fashion the metal is softened and prepared for future work such as shaping, stamping, or forming.

Annealing occurs by the diffusion of atoms within a solid material, so that the material progresses towards its equilibrium state. Heat is needed to increasing the rate of diffusion by providing the energy needed to break bonds. The movement of atoms has the effect of redistributing and destroying the dislocations in metals and (to a lesser extent) in ceramics. This alternation in dislocations allows metals to deform more easily, so increases their ductility.

3.3.1 Stages

There are three stages in the annealing process, with the first being the recovery phase, which results in softening of the metal through removal of crystal defects (the primary type of which is the linear defect called a dislocation) and the internal stresses which they cause. Recovery phase covers all annealing phenomena

that occur before the appearance of new strain-free grains. The second phase is recrystallization, where new strain-free grains nucleate and grow to replace those deformed by internal stresses. If annealing is allowed to continue once recrystallization has been completed, grain growth will occur, in which the microstructure starts to coarsen and may cause the metal to have less than satisfactory mechanical properties.

3.3.2 Setup and Equipment

Typically, large ovens are used for the annealing process. The inside of the oven is large enough to place the work piece in a position to receive maximum exposure to the circulating heated air. For high volume process annealing, gas fired conveyor furnaces are often used. For large work piece or high quantity parts, car-bottom furnaces will be used in order to move the parts in and out with ease. Once the annealing process has been successfully completed, the work pieces are sometimes left in the oven in order for the parts to have a controlled cooling process. While some work pieces are left in the oven to cool in a controlled fashion, other materials and alloys are removed from the oven. After being removed from the oven, the work pieces are often quickly cooled off in a process known as quench hardening. Some typical methods of quench hardening materials involve the use of media such as air, water, oil or salt. Quench hardening is generally applicable for some ferrous alloys, but not copper alloys.

3.4 Thermal Treatment of the Nanocrystalline Amorphous Ribbon

With a view to study nanocrystallization behavior by XRD and magnetic properties upon evaluation of nanocrystalline phase on amorphous matrix, thermal treatment, i.e. annealing is required to perform. For XRD, as prepared amorphous ribbon were cut into small pieces of about 2cm lengths for annealing treatment. MTI Corporation built GSL-1600x40 tube furnace used for this purpose shown in Figure 3.9. The samples were put into the tube and filled up with Nitrogen gas before the tube furnace heated to a predefined temperature and kept for the time (30 minute) required completing the annealing. In this way all the isothermal annealing as a function of time were performed.



Figure 3.9 MTI - GSL-1600x40 Tube Furnaces

3.5 Powder/ Polycrystalline Diffraction

About 90% of all solid materials can be described as crystalline. When X-ray interacts with a crystalline substance (phase) one get a diffraction pattern. The X-ray diffraction pattern of a pure substance is, therefore, like a fingerprint of the substance. The powder diffraction method is thus ideally suited for characterization and identification of polycrystalline phases. Today about 50000 inorganic and 25000 organic single components, crystalline phase and diffraction patterns have been collected and stored on magnetic or optical media as standers. The main use of powder diffraction is to identify components in a sample by a search match procedure. Furthermore, the areas under the peak are related to the amount of each phase present in the sample.

3.5.1 Theoretical Considerations of X-ray Diffraction (XRD)

The German Physicist Wilhelm Roentgen discovered X-rays in 1895. X-rays are electromagnetic waves of short wavelengths in the range of 10^{-2} to 10^2\AA . Unlike ordinary light, these rays are invisible, but they travel in straight lines and affect photographic film in the same way as light. On the other hand, they were much more

penetrating than light and could easily pass through the human body, wood, quite thick pieces of metal and other “opaque” objects.

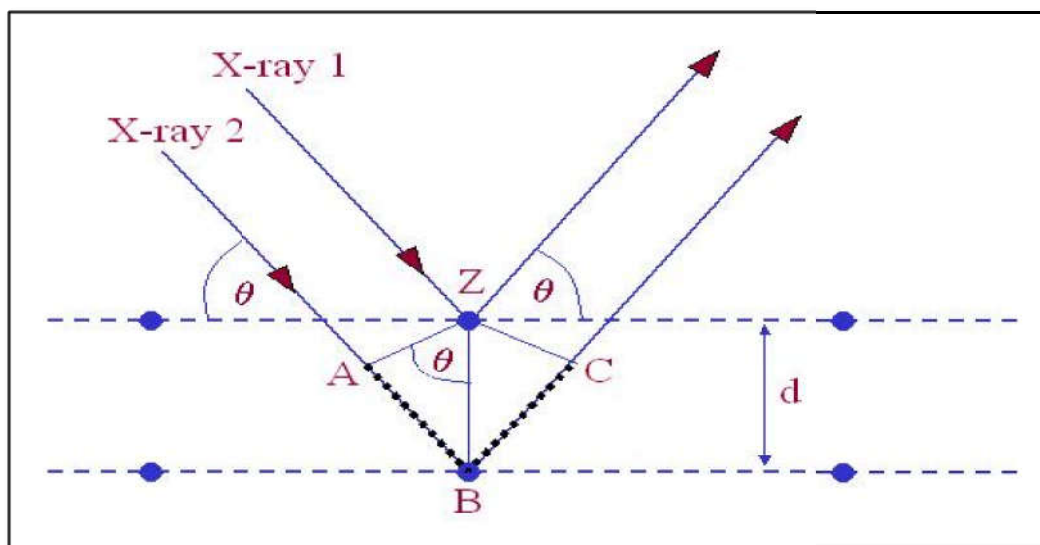


Figure 3.10 Bragg's diffraction pattern

The XRD provides substantial of information on the crystal structure. XRD is one of the oldest and effective tools for the determination of the atomic arrangement in a crystal. The wavelength (1\AA) of an X-ray is the same order of magnitude as the lattice constant of crystals and it is this which makes X-rays so useful in structural analysis of crystal. Whenever X-rays are incident on a crystal surface, they are reflected from it. The reflection abides by the Bragg's Law as given below

$$2d \sin \theta = n\lambda \quad (3.2)$$

Where d is the distance between crystal plane, θ is the incident angle, λ is the wavelength of the X-ray and n is a positive integer. Bragg's Law also suggested that the diffraction is only possible when $\lambda < 2d$.

X-ray diffractograms of all the samples were recorded using monochromatic Cu- K_{α} radiation ($\lambda = 1.54053 \text{\AA}$) to ensure the formation of single-phase nature of the product. XRD patterns information are: scanning speed 2° , chart speed 20 mm, starting from 20° and ending at 90° . Peak intensities are recorded corresponding to their 2θ values. The inter planner distance - d was calculated from these 2θ values of the diffraction peaks using the Bragg's Law (Figure 3.10).

Therefore the two possible values where we can have reflections are determined by the unit cell dimensions. However, the intensities of the reflection are determined by the distribution of the electrons in the unit cell. The highest electron

density is found around atoms. Therefore, the intensities depend on what kind of atoms we have and where in the unit cell they are located. Planes going through areas with high electron density will reflect strongly, planes with low electron density will give weak intensities.

3.5.2 X-ray Powder Method

Powder method is perhaps the most widely used X-ray diffraction technique for characterizing materials. The term ‘powder’ really means that the crystalline domains are randomly oriented in the sample. Therefore, when the 2-D diffraction pattern is recorded, it shows concentric rings of scattering peaks corresponding to the various d spacing in the crystal lattice. The positions and the intensities of the peaks are used for identifying the underlying structure (or phase) of the material. Powder diffraction data can be collected using either transmission or reflection geometry, as shown in Figure 3.11 below.

Because the particles in the powder sample are randomly oriented, these two methods will yield the same data. Powder diffraction data are measured using Bruker AXS D8 Advance diffractometer, which measures data in reflection mode and is used mostly with solid samples, or the custom built 4-circle diffractometer, which operates in transmission mode and is more suitable for liquid phase samples.

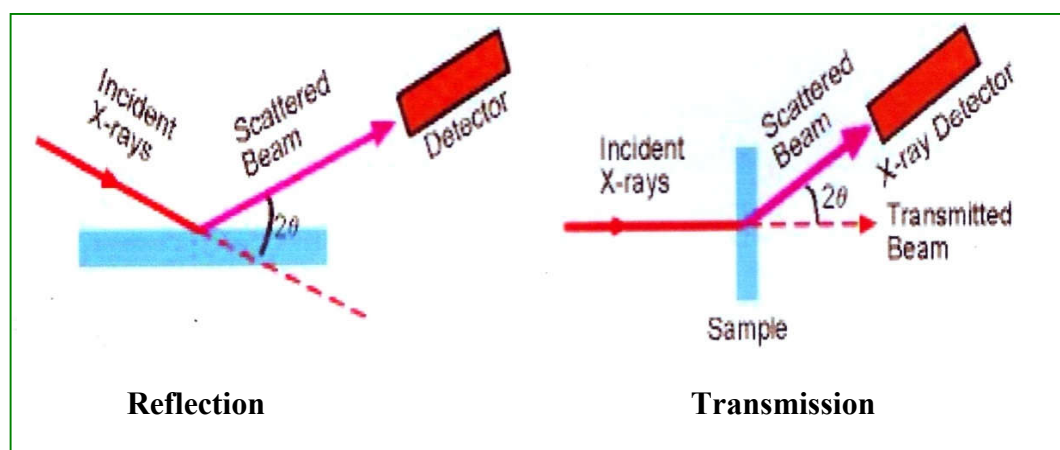


Figure 3.11 Reflection and Transmission geometry of powder diffraction

3.5.3 Experimental Technique for X-ray Diffractometer

X-ray diffraction (XRD) is a versatile non-destructive analytical technique for identification and quantitative determination of various crystalline phases of powdered or solid samples of any compound. For each set of composition, ribbons are cut into several pieces; each of length 20 mm. Heat treatment was performed on the amorphous ribbons using a tube furnace which filled by nitrogen gas. After the heat treatment, samples were removed from the furnace tube carefully and kept separately for XRD experiment.

For XRD experiment each sample was set on a glass slides and fixed the sample by putting adhesive tape at the two ends of the sample. After the pattern is obtained the value of 2θ is calculated for each diffraction line; set of 2θ values is the raw data for the determination of the lattice parameters of the unit cell. Figure 3.12: Shows the block diagram of Bruker AXS D8 Advance X-ray diffractometer. The Bucker AXS D8 Advance X-ray diffractometer was used for the lattice parameter determination in the PP&PDC, Materials Science Division, Bangladesh Council of Scientific and Industrial Research (BCSIR), Dhaka. Figure 3.13 shows the inside view of the Bucker AXS D8 Advance XRD system. The Bruker AXS D8 Advance diffraction system utilizes a modular system approach to provide performance for application ranging from routine characterization to in-depth research investigation.

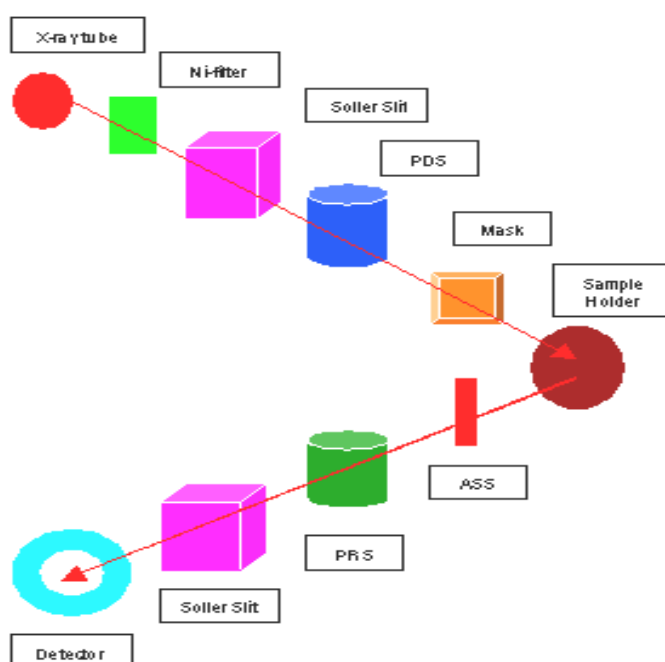


Figure 3.12 Block diagram of the Bruker AXS D8 Advance XRD system



Figure 3.13 Bruker AXS D8 Advance

The powder diffraction technique was used with a primary beam power of 40 kV and 40mA for Cu radiation. A nickel filter was used to reduce Cu-K_α radiation and finally Cu-K_α radiation was only used as the primary beam. A $(\theta - 2\theta)$ scan was taken from 30° to 90° to get possible fundamental peaks of the sample with the sampling pitch of 0.02° and time for each step data collection was 1.0 sec. Both the programmable divergence and receiving slits were used to control the irradiated beam area and output intensity from the sample respectively.

An anti-scatter slit was used just after the sample holder to reduce air scattering. Two solar slits were used just after the tube and in front of the detector to get parallel beam only. All the data of the samples were stored in the computer memory and later analyzed that using computer software “DIFFRAC^{plus}”.

The Bruker AXS D8 ADVANCE has the ability to perform a full range of applications, from qualitative and quantitative phase identification, under ambient or

non-ambient conditions, to crystal structure solution from powder samples, crystallite size determination, micro strain analysis, residual stress analysis, and preferred orientation.

Bruker AXS D8 Advance SPECIFICATIONS	
X-RAY SOURCE	2.2kW Cu and Co, Running condition (40kV, 40mA), Power stability is better than 0.01%
DETECTORS	Point detector, Vantec-1 detector
OPTICS	Gobel Mirror
GONIOMETER	High precision microprocessor controlled, two circle goniometer with independent stepper motors and optical encoders; Smallest angular step 0.0001°; Reproducibility +/- 0.0001°
SAMPLE STAGE	Centric ¼-Circle Eulerian Cradle. Motorized Chi (tilt) and Phi (rotation) rotations and X-Y-Z translations. The cradle accommodates bulky specimens, powders, thin-films, and wafers up to 80 x 50 x 20 mm and weighing up to 1 kg
ATTACHEMENTS	High Temperature MRI stage (RT-1400C), Thin Film Reflectometry, sample spinner, video camera, sample plate with 9-sample holders
SOFTWARE	LEPTOZ, TOPAZ, ICCD
Attributes	
Depth	1135 mm
Height	1868 mm
Width	1300 mm
Weight	770 kg
Additional Specifications	<p>Configurations: Vertical goniometer, Theta/2Theta or Theta/Theta geometry</p> <p>Measuring circle diameter: Predefined at 500 mm, 560 mm and 600 mm or any intermediate setting</p> <p>Angular range: 360°</p> <p>Max. usable angular range: -110° < 2Theta 168°</p> <p>Angle positioning: Stepper motors with optical encoders</p> <p>Smallest addressable increment: 0.0001°</p> <p>Instrument alignment: Equal or better than ± 0.01° 2Theta; NIST SRM 1976a always included</p> <p>Maximum angular speed: 20°/s</p> <p>Detectors:</p> <p>Point detectors: Scintillation counter</p> <p>SOL-XE energy dispersive</p> <p>1-D detectors: LYNXEYE, VANTEC-1</p> <p>All detectors guaranteed without defective/dead strips or areas</p> <p>Cooling water supply:</p> <p>Min. 4 l/min, pressure 4 bar to 7.5 bar, no pressure on outlet side, temperature: 10 °C to 20 °C</p> <p>Power supply:</p> <p>Single phase: 208 to 240 V, Three phases: 120 V, 230 V, 240V; 47 to 63 Hz</p>

3.5.4 Analysis of XRD data

The XRD data consisting of θ_{hkl} and d_{hkl} values corresponding to the different planes from which the following structural information of the nanocrystalline ribbon sample was evaluated.

- (i) Identification of phases
- (ii) Lattice parameter determination
- (iii) Average grain size determination
- (iv) Si- content determination in nanograins

(i) Identification of phases

The most common use of powder (polycrystalline) diffraction is chemical analysis. This can include phase identification (search/match), investigation of high/low temperature phase, solid solutions and determination of unit cell parameter of new materials.

XRD has become a very popular and useful instrument for routine X-ray analysis of nanocrystalline amorphous ribbon samples. In fact the diffractometer technique is often preferred to Debye-Scherrer technique owing to its several inherent merits. The most striking difference between the two methods is in the use of different intensity detection and measuring devices. XRD pattern of as-cast indicates just amorphous pattern of the given composition. The XRD patterns are identified as bcc α -Fe (Si) solid solution, which are developed on the nanocrystalline amorphous ribbon after heat treatment. The peak pattern is observed for all the samples at different heat treatment temperatures indicating the bcc α -Fe (Si) phase, which is developed on amorphous ribbons after heat treatment. Present experiment reveals that 450°C is not sufficient temperature to start forming of crystalline nanograins of bcc Fe (Si) on the amorphous ribbon of the studied alloy composition.

(ii) Lattice Parameter Determination

Lattice parameter of crystalline bcc Fe-Si nanograin has been determined for all the two different amorphous compositions at different heat treatment temperatures. Normally, lattice parameter of an alloy composition is determined by the Debye-Scherrer method after extrapolation of the curve. In the present case, only one reflection (110) is prominent in all XRD patterns and we would like to understand

how the value of lattice parameter changes with annealing temperature. We have, therefore, determined the lattice parameter using only that particular reflection using equation $2d \sin \theta = \lambda$ and $a_0 = d\sqrt{2}$, where $\lambda = 1.54178 \text{ \AA}$ for $\text{Cu} - K_\alpha$ radiation and a_0 is the determined lattice parameter within an error estimated to be $\pm 0.0001 \text{ \AA}$.

(iii) Grain Size Determination

The main aim (vital point) of the present study is to determine the nanocrystalline grain size for all the heat treated samples of the alloy composition by using Scherrer method. The XRD pattern of (110) reflection for different steps of heat treatment temperature of the alloy composition is used to calculate grain size. Grain size is determined using the following formula,

$$D_g = \frac{0.9\lambda}{\beta \cos \theta} \quad (3.3)$$

Where $\lambda = 1.54178 \text{ \AA}$ for $\text{Cu} - K_\alpha$ radiation and $\beta = \text{FWHM}$ (full width at half maximum) of the peak in radian. Considering β in degree we get the following relation

$$D_g = \frac{79.5}{\beta \cos \theta} \quad (3.4)$$

All the values of grain size for every steps of heat treatment temperature of the alloy composition were determined. The FWHM of the peak is large at the early heat treatment temperature and with the increase of heat treatment temperature the value of FWHM becomes smaller which means that the grain size is increasing gradually.

(iv) Si-content in Nanograins

Crystalline nanograins were formed on the amorphous matrix of the ribbon in the process of heat treatment having the composition of Fe-Si. It is, therefore important to determine the concentration of Fe and Si in the nanograin. As because the alloy consists of Fe and Si and we have experimentally determined the lattice parameter of the alloy nanograin for the two compositions at different temperatures. It is easy to calculate the Si content in the nanograins from the data of Pearsons who was established the relationship between the lattice parameter as dependent on Si content in Fe-Si alloys covering a wide range of composition [3.6]. From the relationship, we have constructed a simple equation to calculate Si content from lattice parameter. The equation is

$$X = \frac{(a_0 - 2.8812)}{0.0022} \quad (3.5)$$

where X is at. % Si in the nanograins, a_0 is the determined lattice parameter of nanograins. Si-contents for the nanograins develop during the isothermal annealing at various temperatures have been calculated.

3.6 Magnetization Measurement Techniques

In the present study magnetization has been performed using a Vibrating Sample Magnetometer (VSM).

3.6.1 Vibrating Sample Magnetometer (VSM)

A vibrating sample magnetometer (VSM) operates on Faraday's Law of Induction, which tells us that a changing magnetic field will produce an electric field. This electric field can be measured and can tell us information about the changing magnetic field. A VSM is used to measure the magnetic behavior of magnetic materials. VSM is a versatile and sensitive method of measuring magnetic properties developed by S. Foner [3.7-3.8] and is based on the flux change in a coil when the sample is vibrated near it. The VSM is designed to continuously measure the magnetic properties of materials as a function of temperature and field. In this type of magnetometer, the sample is vibrated up and down in a region surrounded by several pickup coils. The magnetic sample is thus acting as a time-changing magnetic flux, varying inside a particular region of fixed area. From Maxwell's law it is known that a time varying magnetic flux is accompanied by an electric field and the field induces a voltage in pickup coils. This alternating voltage signal is processed by a control unit system, in order to increase the signal to noise ratio. The result is a measure of the magnetization of the sample.

3.6.2 Principle of VSM

The principle of VSM is as follows: when the sample of a magnetic material is placed in a uniform magnetic field, a dipole moment proportional to the product of the sample susceptibility times the applied field is induced in sample. If the sample is made to undergo a sinusoidal motion, an electrical signal is induced in suitably located stationary pick-up coils. This signal which is at the vibrating frequency, is proportional to the magnetic moment, vibration amplitude and vibration frequency. In order to obtain the reading of the moment only, a capacitor is made to generate

another signal for comparison which varies in its moment, vibration amplitudes and vibration frequency in the same manner as does the signal from the pick-up coil. These two signals are applied to the two inputs of a differential amplifier, and because the differential amplifier passes only difference between the two signals, the effects of vibration amplitude and frequency changes are cancelled. Thus only the moment determines the amplitude of the signal at the output of the differential amplifier. This signal is in turns applied to a lock-in amplifier, where it is compared with the reference signal which is at its internal oscillator frequency and is also applied to transducer which oscillation the sample rod. Thus the output of the lock-in amplifier is proportional to the magnetic moment of the sample only avoiding any noise of frequency other than that of the signal. The lock-in action yields an accuracy of 0.05% of full scale. The absolute accuracy of this system is better than 2% and reproducibility is better than 1%. Least measurable moment is 5×10^{-4} emu.

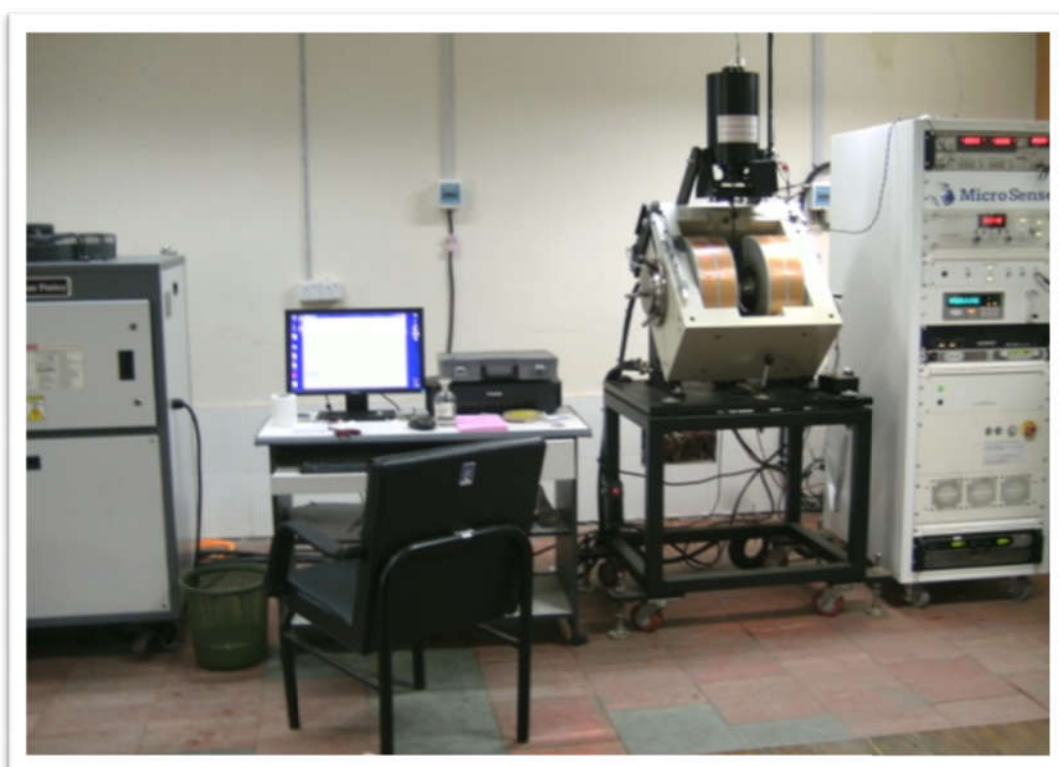


Figure 3.14 Vibrating Sample Magnetometer (VSM)

These measurements were carried out at Materials Science Division, Atomic Energy Center, Dhaka. We use Hirst VSM02 which is an automatic VSM for characterization of soft and hard magnetic materials manufactured by HIRST Magnetic Instruments Ltd. The Hirst VSM system arrangement is shown in the Figure 3.14.

The function of the associated electronic circuits is:

- (i) To permit accurate calibration of the signal output obtained from the detection coils.
- (ii) To produce a convenient AC output signal which is directly related to the input and which can be recorded.
- (iii) To produce sufficient amplification for high sensitivity operation.

The block diagram of the electronic circuit used for the VSM consists of a mechanical vibrator, a sine wave generator, an audio amplifier, a ratio transformer, a phase-shifter, a lock-in amplifier, a pick-up coil system, a reference coil system and an electromagnet.

The sample magnetized by the electromagnet generates an e.m.f in pick-up coils PC. The strength of this signal is proportional to the magnetization of the sample. The vibrating permanent magnet also generates an e.m.f of fixed amplitude in the surrounding reference coils. This reference signal is stepped down with the help of a ratio transformer so that its amplitude is equal to that the sample signals. The two signals are then brought in phase and put to the lock-in amplifier. The Lock-in amplifier works as a null detector. The ratio transformer reading is to be calibrated using spherical shape sample S of 99.99% pure Nickel.

THEORETICAL BACKGROUND

2.1 History of Nanocrystalline Materials

A new class of Fe-based alloys was introduced by Yoshizawa, Oguma and Yamauchi, in 1988 which exhibited superior soft magnetic behavior. The material was produced by crystallization of an amorphous Fe-Si-B alloy with small additions of Cu and Nb. The identifying characteristic of the new material is its ultrafine microstructure of Fe(Si) with grain sizes of 10-15nm from which their soft magnetic properties emerge. These include coercivities of 0.01Oe and permeabilities of $\sim 10^5$. The alloy system, originally proposed as Fe-Cu-Nb-Si-B alloys, was manufactured by Hitachi CO. Ltd. Under the trade names FINEMET [2.1]. The originally proposed composition was $\text{Fe}_{73.5}\text{Cu}_1\text{Nb}_3\text{Si}_{13.5}\text{B}_9$. The unique properties of FINEMET alloys include low losses, high permeability and near zero magnetostriction achieved by permelloy and Co-based amorphous alloys, but much higher saturation magnetization up to 1.3 Tesla, than these materials usually have ever offered.

Nanocrystalline materials can be considered as an off-shoot of amorphous material. In fact nanocrystalline amorphous ribbons are composite materials where nanocrystals are embedded in an amorphous matrix. Nanocrystalline materials represent one of the most active research areas in recent times for the atomic tailoring of materials with specific properties and property combinations. However, it is still in its infancy since its emergence as potential materials has just begun at this stage of development. In the conventional soft magnetic materials, “whose grain size is far larger than $1\mu\text{m}$ ”, it is well known that the soft magnetic properties become worse and coercive force increases when crystal grain becomes smaller. It is well known that the microstructure, noticeably the grain size, essentially determines the hysteresis loop of a ferromagnetic material.

From the nanometer regime to macroscopic grain sizes, the permeability shows an analogous behavior being essentially inversely proportional to H_c . Coercive force is thought to be inversely proportional to D_g . Lowest coercivities, however are again found for smallest structural correlation lengths like in amorphous alloys and in nanocrystalline alloys for grain sizes $< 20\text{nm}$. Therefore, main efforts to improve the

soft magnetic properties are directed to make the crystal grain size larger and / or to make the magnetic domain size smaller by annealing and working.

In magnetic materials, the ‘Ferromagnetic exchange length’ (L_{ex}) expresses the characteristic distance over which a magnetic atom influence its environment, and has values on the order of 100nm. If the magnet has a structure with grain diameters smaller than the average length, it becomes possible to “average” the anisotropy of the grains to a low bulk value. Under the sequence of this randomized anisotropy, such a material realizes the high saturation magnetization, M_s in the crystalline state and low coercivity, H_c due to randomized anisotropy. According magnetic softening should occur as soon as the structural correlation length or D_g becomes smaller than the E_{ex} which is in the order of domain wall width. In this case, the local anisotropies are randomly averaged out by exchange interaction so that there is no anisotropy net effect on the magnetization process. It is well accepted that good magnetic properties are obtained when $D_g \ll L_{ex}$ [2.2]. However, FINEMET demonstrated a new phenomenon; reduction of grain size, “to a nanometer level”, improves the soft magnetic properties significantly. In this nano-world, the H_c is directly proportional to D_g , D_g on the order of D_g^2 to D_g^6 .

2.2 Composition of the Nanocrystalline

Generally the optimum mechanical and magnetic properties of nanocrystalline soft magnetic materials are obtained for partially crystallized materials. This means that those materials are formed in two phases [2.3]. In general nanocrystalline alloys can be described as $TL_{1-x}(TE, M, NM)_x$ where

- TL denotes a late ferromagnetic transition metal element (TL= Co, Ni or Fe)
- TE denotes an early transition metal element (TE = Zr, Nb, Hf, Ta etc.)
- M is metalloid (M = B, P, Si, etc.) and
- NM is a noble metal (NM=Cu, Ag, Au etc.)

This composition usually has $x < 0.02$ i.e. with as much late ferromagnetic transition metal (TL of Fe, Co or Ni) as possible. The remaining early transition metals (TE = Zr, Nb, Hf, Ta, etc.) and metalloids (B, P, Si, etc.) are added to promote glass formation in the precursor. The noble metal elements (NM = Cu, Ag, Au, etc.) serve as nucleating agents for the ferromagnetic nanocrystalline phase. The compositions are limited by which glass formation can occur prior to the

nanocrystallization route. These alloys may be single phase (Type-I) but are generally two phase materials with a nanocrystalline ferromagnetic phase and a residual amorphous phase at the grain boundaries (Type-II). The type-II nanocrystalline alloys might have general properties:

- Relatively high resistivity (50 - 80 $\mu\Omega$ -cm)
- Low magnetocrystalline anisotropy and
- Increase mechanical strength

With properties such as these, nanocrystalline alloys have great potential as soft magnetic properties. In the ongoing research we are interested about the type-II.

One of the important features of this magnetic system is that one can play with different compositions, annealing temperatures and time to control the grain size and their distribution upon, which the magnetic properties of these new materials strongly depend. In choosing the composition, one has to consider the magnetic component like Fe, Co or Ni, the crystallization initiating component e.g. Cu and the component Nb for stabilizing the nanocrystal by inhibiting the grain growth and glass forming materials like Si, B, etc.

Nanocrystalline soft magnetic alloys have received considerable attention due to their excellent soft magnetic properties [2.4]. Small addition of Cu and Nb into Fe-Si-B amorphous materials changes considerably their crystallization process, which is executed under appropriately controlled conditions and the specific purpose of these additions are

- The element is used for helping the formation of nuclei and ultra-fine grain and
- The element is used to impede the growth of the crystallites.

In this material, the nanocrystalline state is composed of a fine structure of α -Fe(Si) and is usually around 10nm. For such as average grain size the exchange interaction dominates the magnetic behavior of randomly oriented crystallites guided by random anisotropy [2.4]. In the present thesis work nanocrystalline alloys are prepared by Cu replacement Ag and Au of FINEMET composition with $\text{Fe}_{73.5}\text{Cu}_1\text{Nb}_3\text{Si}_{13.5}\text{B}_9$.

2.2.1 An overview of Nanocrystalline Materials

In a single phase nanocrystalline alloy, as long as the first criterion is met, and the alloy is below Curie temperature, the model holds. This is not necessarily the case for multiphase system such as we find in many of the nanocrystalline alloys that are produced from amorphous precursors. For a two phase microstructures with a ferromagnetic intergranular amorphous phase and a single ferromagnetic nanocrystalline phase, the nature of the nanocrystal-amorphous-nanocrystal coupling is of the paramount importance to the properties of these materials. This coupling depends upon the size of the nanocrystallites, and more importantly upon the amount, chemistry and thickness of the amorphous phase. The best properties, of course, are when both criteria are met, below presumably the lower Curie temperature of the amorphous phase.

Slawska - Waniewska *et. al.* [2.5] have observed T-dependent magnetic response in partially and fully nanocrystallized FINEMET materials. They concluded that for sufficiently small nanocrystals with enough intergranular material between them to diminish or destroy coupling between grains that super paramagnetic response would be observed. This would not be the case for properly annealed samples with sufficient volume fraction of the nanocrystalline ferromagnetic. Characteristic of super paramagnetic response, first proposed by Bean *et. al.* [2.6] includes

- (i) a Langevin function scaling of magnetization data
- (ii) disappearance of the coercivity above a blocking temperature and
- (iii) time dependent magnetization, due to thermally activated switching of the magnetization.

Nanocrystalline amorphous ribbon can be considered as an off-shoot of amorphous materials. In fact nanocrystalline amorphous ribbon is a composite material where nanocrystals are embedded in an amorphous matrix. Nanocrystalline materials represent one of the most active research areas in recent times for the atomic tailoring of materials with specific properties and property combinations. However, it is still in its infancy since its emergence as potential material has just began at this stage of development. There have been glimpses of exciting new properties like super plasticity, giant magneto resistance (GMR), transparency in opaque ceramics, enhanced homogeneity, unusual soft ferromagnetic and giant magnetocaloric effects,

processed by these material where reduced to nanometer dimension. In addition to the understanding of the usual properties possessed by nanophase materials, there are three other associated areas, which need serious attention:

- (i) Identification and development of suitable preparation methods, especially those which are capable of providing large industrial quantities of nanometer scale materials.
- (ii) Development of processing methods for manufacturing these materials into useful size and shapes without losing their desirable nanometer size feature and
- (iii) Identification of proper characterization methods, where the nanometer size range of these materials falls just below or at the resolution limit of the conventional tools.

2.2.2 Alloy Design Issues

Alloy design issues include issues of chemistry and processing designed to:

- (i) Optimize one of a number of important intrinsic and or extrinsic magnetic properties and
- (ii) Optimize structural or microstructural features which promote important magnetic properties.

The first of these issues concerns the choice of chemistry so as to impact the intrinsic magnetization of the material. The second issue pertinent to alloy additions designed at aiding formation of an amorphous phase.

As intrinsic properties we take to mean microstructure insensitive properties including the saturation magnetization, Curie temperature, magnetocrystalline anisotropy and magnetostrictive co-efficient are all important. Also it includes magnetic dipole moment and exchange interaction. Extrinsic magnetic properties important in soft magnetic materials include the magnetic permeability and coercivity, which typically have an inverse relationship. Also include magnetic anisotropy and magnetic coupling through amorphous phases are included to these properties. Magnetic anisotropy and magnetostriction can be considered as extrinsic (microstructure sensitive) in the same that for a two phase material (in aggregate) they depend on microstructure.

Since microstructure of alloy in influence extrinsic magnetic properties, the important microstructure features should be recognized including grain size, shape

and orientation, defect concentration, compositional in homogeneities, magnetic domain and domain wall. The development of soft magnetic materials for application requires attention to a variety of intrinsic magnetic properties as well as development extrinsic magnetic properties though an appropriate optimization of the microstructure.

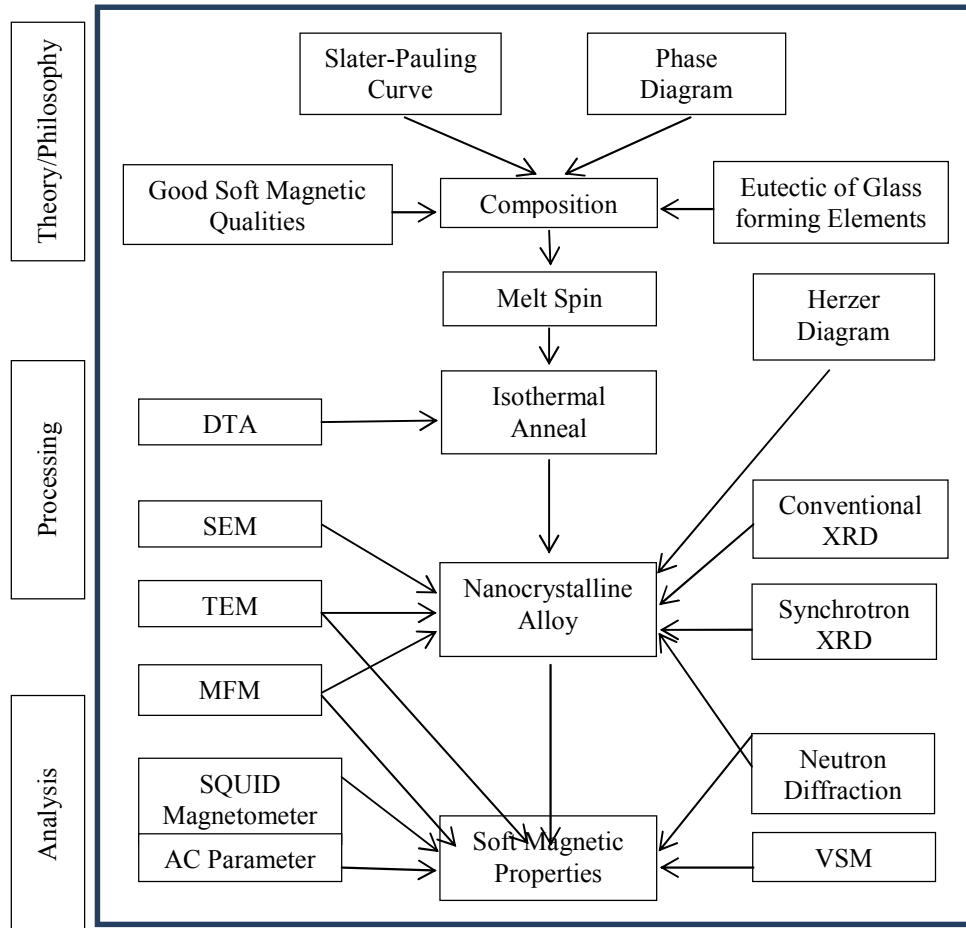


Figure 2.1 Flowchart for the consideration in designing and developing nanocrystalline soft magnetic material from an amorphous precursor route

Alloy design issues are influenced by processing routes used to achieve desired microstructures. In Figure 2.1 illustrates a flowchart for the considerations in designing and developing nanocrystalline soft magnetic material from an amorphous precursor route as an example of the design process. Here we consider first, the effects of alloy composition on intrinsic magnetic properties. This is followed by consideration of alloying additions necessary to produce an appropriate amorphous precursor. Typical experimental steps used to identify the structure and properties of the resulting materials are also illustrated.

2.2.3 Stages of Evolution of Microstructure

The basic principle for the crystallization method from amorphous solids is to control the crystallization kinetics by optimizing the heat treatment conditions such as annealing temperature and time, heating rate, etc. so that the amorphous phase crystallizes completely in to a polycrystalline material with ultrafine crystallites nanocrystallization can be realized upon either isothermal or an isothermal annealing in various amorphous metallic alloys in the form of ribbons. Formation of the nanocrystalline microstructure in the amorphous phase was depicted by Herzer in the ‘nanocrystalline of soft magnetic alloys’[2.7]. Figure 2.2 presents the steps of formation of the nanocrystalline microstructure from the amorphous state. Controlled crystallization of FINEMET type of Fe-Cu-Nb-Si-B alloys can be used to obtain partially crystallized materials with nanometer size crystallite embedded in residual amorphous matrix. These special nanocrystal/amorphous composite structures with appropriate compositions allow the material to exhibit extraordinary soft magnetic properties [2.8-2.11].

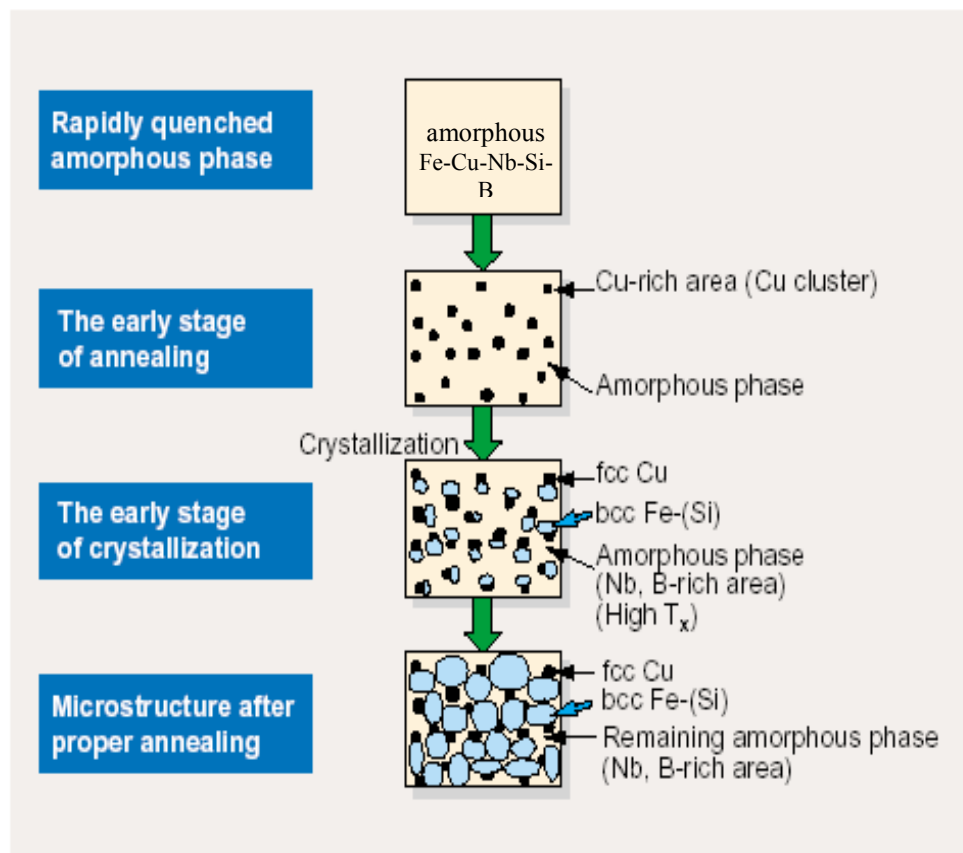


Figure 2.2 Schematic illustration of the formation of nanocrystalline structure

The formation of the particular nanocrystalline structure is essentially related to the combined addition of Cu and Nb (or other group IV or VI elements) and their low solubility in Fe-Si (< 0.2 at % Cu, < 0.1 at % Nb). Copper enhances the nucleation of bcc grains while Nb impedes grain coarsening and at the same time, inhibits the formation of Boride compounds. The microstructure evolution is schematically illustrated in Figure 2.2 can be summarized.

Annealing at temperatures in general between about 500°C to 600°C leads to primary crystallization of the bcc Fe. At the initial stage of annealing, before the onset of crystallization, the phase separation tendency between Cu and Fe leads to the formation of Cu-rich clusters, with 5 nm size and probably still amorphous [2.12-2.13]. The presence of Nb seems to promote the formation of these Cu-rich clusters on a much finer scale than in an Nb free alloy composition [2.14]. This happens when the annealing treatment is carried out at around 550°C when Cu clusters are formed with a few nanometer diameters. Because the investigators [2.15] observed that Cu clusters and bcc phase simultaneously at the early stage of the nanocrystallization.

This cluster formation causes a concentration fluctuation of Fe, since Cu substitutes for Fe. Thus, the regions in between Cu-rich clusters provide a significantly increased density of nucleation sites for the crystallization of Fe. The consequence is an extremely fine nucleation of Fe-Si crystallites at high rate which subsequently grow in a diffusion controlled process [2.16] as the annealing proceeds further. Slightly annealing at higher temperature at the initial stage of crystallization α -Fe(Si) phase forms. At this stage Nb and B are excluded from α -Fe(Si) and are enriched in the remaining amorphous phase, because they are insoluble in the α -Fe(Si) phase.

Thus the regions in between the Cu rich clusters provide a significantly increased density of nucleation sites for the crystallization of bcc Fe. The consequence is an extremely fine nucleation of bcc Fe-Si crystallites at a high rate, which subsequently grow in a diffusion-controlled process as the annealing proceeds further as annealing goes on the grain size of the α -Fe(Si) increases. At the same time the Si content of this phase keeps increasing since Si tends to be partitioned to the bcc α -Fe(Si) phase. Since the Nb and B enrichment in the amorphous phase stabilizes the remaining state, the grain growth of the bcc phase eventually stops. The presence of Nb at the same time inhibits the formation of Fe-B compounds. The Cu concentration of the clusters also increases as the crystallization proceeds.

At the optimum stage, three distinct phases are present based on the chemical composition. As the bcc Fe-Si phase forms, Nb and B are excluded from the crystallite because of their low solubility in bcc Fe and are enriched in the residual amorphous matrix. At a time all the Si tends effectively to be partitioned into the bcc Fe-Si phase [2.17-2.18]. The particular enrichment with B and Nb increasingly stabilizes the residual amorphous matrix, thus, hinders coarsening of the bcc grains. The presence of Nb at the time inhibits the formation of iron boride compounds. The transformation finally ceases in a metastable two-phase microstructure of bcc Fe-Si embedded in an amorphous Fe-Nb-B matrix. Only annealing at more elevated temperature above about 600°C leads to the precipitations of small fractions of boride compounds like Fe₂B or Fe₃B with typical dimensions of 50nm to 100nm, while the ultra-fine grain structure bcc Fe-Si still persists. Further increase of the annealing temperature above about 700°C finally yields grain coarsening. Both the formation of Fe-borides phase and grain coarsening deteriorates the soft magnetic properties significantly.

2.2.4 Advantages of Soft Nanocrystalline Alloys

The unique properties of FINEMET alloys include low losses, high permeability and near zero magnetostriction achieved by permalloys and Co-based amorphous alloys, but much higher saturation magnetization up to 1.3 Tesla, than these materials usually have ever offered. Nanocrystalline amorphous ribbons are produced by the melt-spinning technique to produce an amorphous metal and then heat treating this alloy at temperature higher than its crystallization temperature. The choice of soft magnetic materials for applications has been guided by recent developments in the field of soft magnetic materials. Amorphous and nanocrystalline magnetic materials, in terms of combined induction and permeability are now competitive with Fe-Si bulk alloys and the Fe-Co alloys. In Figure 2.3 [2.19], figures of merit for Fe-based amorphous alloys, Co-based amorphous alloys and nanocrystalline alloys are summarized. Co-based amorphous alloys, Fe-based amorphous alloys and nanocrystalline alloys have evolved over the past decades with soft magnetic properties which now exceed those of the bulk alloys based on Fe, Co and Fe-Co.

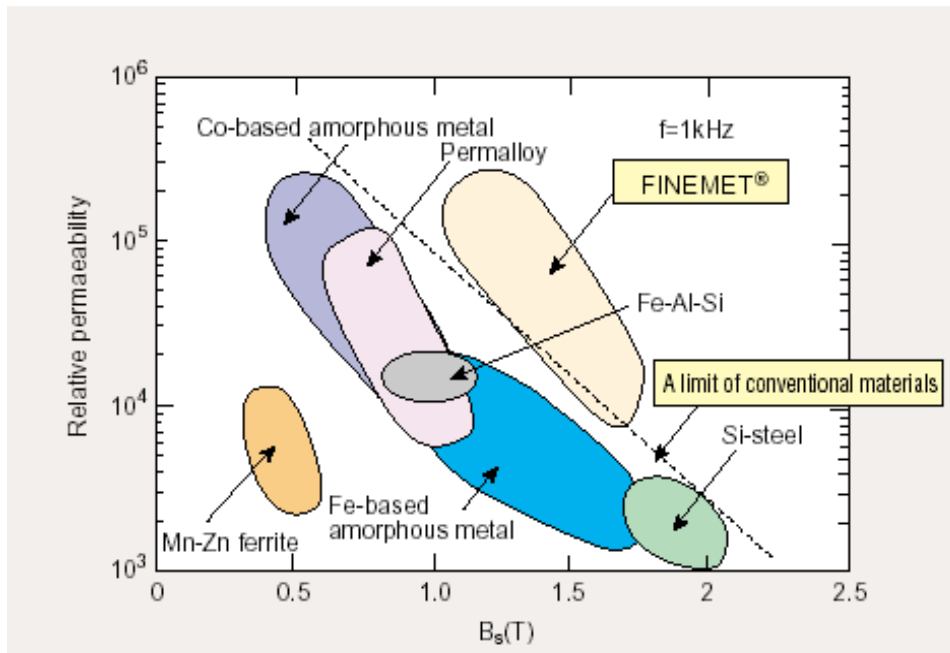


Figure 2.3 FINEMET is superior compared to conventional materials

This FINEMET material is still in its immaturity since its emergence although much research work has been carried out for the potential utility of this unique material.

At the stage of development, this material has the following advantages:

- High saturation magnetic flux density more than 1 Tesla or 10 kOe.
- High permeability over $\mu_i \approx 10,000$ at 100 kHz.
- Excellent temperature characteristics.
- Less affected by mechanical stress.
- Audio noise emission is very low, lower magnetostriction significantly reduces audible noise emission when the voltage and current is applied to the core at audible frequency range.
- Flexible to control the magnetic properties, “B-H curve shape” during the annealing, and three types of B-H curve squareness, high, middle and ion resonance ratio, corresponding to various application.

2.2.5 Viscosity Condition for the Formation of Metallic Glass

We find the condition for the formation of metallic glass in the terms of viscosity and diffusion co-efficient are as follows:

- (i) Metallic atomic bonding of the metals; the viscosity is lower than the diffusion co-efficient and mobility is high.
- (ii) Viscosity becomes high and the diffusion co-efficient decreases in the amorphous state. An atomic bond tends to be covalent as in the case of Silicate (SiO₂).

2.2.6 Conditions for the Formation of Nanocrystalline Alloys

The essential conditions for preparing of nanocrystalline materials are.

- (i) The magnetic properties are highly dependent on the grain size; if the grain size is larger; the magnetic anisotropy would be very high, which in turn will have diverse effect on the soft magnetic properties specially the permeability.
- (ii) For the crystallization process there should be nucleation centers initiated to be distributed throughout the bulk of amorphous matrix.
- (iii) For stabilizing the crystallites there must be a nucleation.
- (iv) Nanocrystalline materials obtained from crystallization must be controlled that crystallites do not grow too big. The grain growth should be controlled so that the grain diameter is within 15-20nm.
- (v) The size of the grain can be limited to nanometer scale by doping group-II metals are
 - Cu (Au, Ag
 - Nb, W, Mo, Cr, Ta etc.
- (vi) The stability must be lower and the crystallization must be higher.

There is additional understanding of the unusual properties possessed by nanophase materials; there are three other associated areas, which need serious attention:

- Identification and development of suitable preparation methods, especially which are capable of providing large industrial quantities of nanometer scale.
- For manufacturing of these materials processing methods should be developed useful size and shape without losing their nanometer size feature.
- Identification of proper crystallization methods, where the nanometer size range of these materials falls just below or at the resolution limit of the conventional tools.

2.3 Factors Contributing to Glass Formation and Stability

Apart from the lack of long range order, an important characteristic of any amorphous structure is the glass transition temperature (T_g). The T_g is the phenomenon in which a glass exhibits a more or less abrupt change in derivative thermodynamic modulus from crystal like to liquid like values with change of temperature. There are three interrelated factors that determine glass-forming tendency. These are:

- (i) Thermodynamic conditions that favor the liquid phase relative to the crystalline phase.
- (ii) The kinetic conditions that inhibit crystallization and
- (iii) The processing factors that arise due to experiential conditions.

The thermodynamic factors for glass formation are liquids temperature (T_m) at which the alloy melts, the heat of vaporization and the free energy of all the phases that arise or could potentially arise during solidification process. Viscosity of the melt, the T_g and the homogeneous nucleation rate belongs to kinetic parameters. The glass transition temperature is defined as the temperature at which the super cooled liquid takes on the rigidity of a solid or more specifically at which the viscosity approaches 15 Poise. Processing parameters are the cooling rate, the heterogeneous nucleation rate and the super cooling temperature interval. The temperature of the glass transition is slightly dependent on the cooling rate. At each cooling rate the glass will freeze in a different state of internal energy.

One of the following two events may occur when a liquid is cooled, either crystallization may take place at the T_m or the liquid will become super-cooled below T_m . If the liquid is super cooled sufficiently, its density gradually falls and its viscosity gradually rises. Thus macroscopic flow of the liquid becomes progressively more difficult. These changes can be observed by monitoring the volume of the super cooled liquid as a function of temperature and a typical result is shown in Figure 2.4 [2.20]. The crystallization process is manifested by an abrupt change in volume at T_m , where glass formation is characterized by a gradual break in slope. The region over which the change of slope occurs is termed the T_g .

The point at which the alloy finally solidifies with frozen in amorphous atomic structure is the T_g . Freezing the amorphous structure at the T_g is a kinetic rather than a thermodynamic transition. The cooling rate decreases gives more time for atomic motion, allowing the liquid to maintain its equilibrium structure to lower the T_g , with

a denser, lower entropy structure. The T_g is not a constant of the material but is a function of experimental conditions. The volume (ΔV) and entropy (ΔS) difference between the liquid and the crystal decrease as the temperature progressively falls, and approach zero at a temperature called the ideal glass transition temperature (T_g^0).

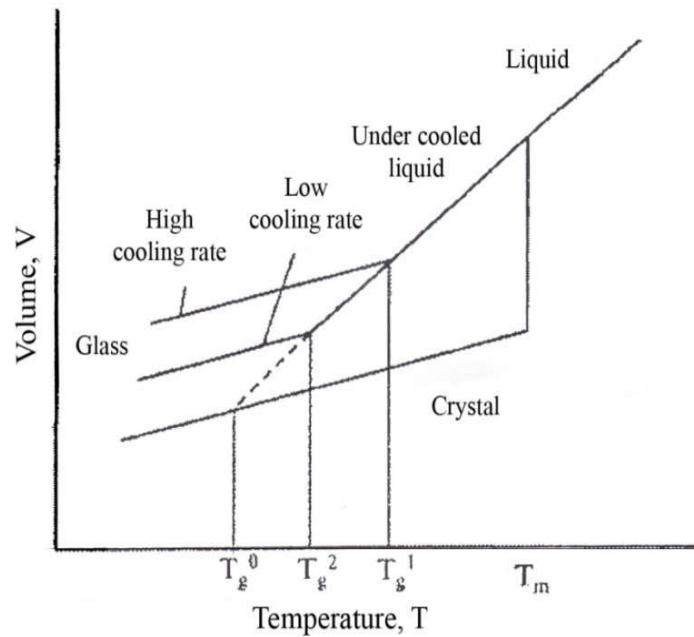


Figure 2.4 Volume-Temperature relationship in solid, liquid and glass state

An amorphous structure with higher density and lower entropy than the corresponding crystal is impossible [2.21]. So T_g^0 is the natural limit of the range of possible T_g , corresponding to a condition of an infinitely slow cooling rate. In general, T_g is defined as the temperature at which an amorphous solid such as glass or a polymer, becomes brittle on cooling, or soft on heating. More specifically it defines a pseudo second order phase transition in which a super-cooled melt yields, on cooling, a glassy structure and properties are similar to those of crystalline materials e.g. of an isotropic solid material [2.22]. The observed T_g , thus, is determined by the heating rates employed in measurement and is less susceptible to previous heat treatment. Now we can measure the glass transition temperature by using Differential Thermal Analysis (DTA).

2.3.1 Stability of the Amorphous and Nanocrystalline Materials

Amorphous materials are always metastable state which leads to transform into more stable crystalline phase. There are three kinds of stability of significance for magnetic ribbons;

- (i) Their resistance to the initiation of crystallization.
- (ii) Structural relaxation effect, and
- (iii) The relaxation or reorientation of directional order.

At temperature below the crystallization temperature, structural relaxation takes place due to atomic rearrangement. It is very difficult to get pure metals in the amorphous state. It is necessary to add glass forming materials to pure metals or alloys to get amorphous state and to bring cooling rate within a reasonable rate. Usually around 20% glass forming materials like B, Si, P, C etc. within a which have atomic radii comparatively small compared to those of metallic atoms occupy the voids left between the bigger atoms of metals when they are closely packed. It can be showed that when there is random close packing of hard spheres, there is about 20% voids created between these atoms.

The glass forming materials the melting point of the alloys and thereby the separation between the glass forming temperature and the crystallization temperature is reduced. Controlled crystallization seems from the amorphous state to be the only method presently available to synthesize nanocrystalline alloys with attractive soft magnetic properties. The formation and the resultant stability of amorphous alloys are important topic both for theoretical understanding and technically. The theoretical analyses of the factors controlling the case of formation and the stability of the resultant amorphous alloys have been extensively reviewed [2.23 - 2.24]. From the thermodynamic view point [2.25 - 2.26], the ability of an alloy to be quenched into the glassy state is generally measured by the magnitude of the quantity.

$$\Delta T_g = T_m - T_g \quad (2.1)$$

Where T_m and T_g are the melting and glass temperature respectively. The stability of the glass after formation in a similar manner is generally measured by the magnitude of the quantity.

$$\Delta T_x = T_x - T_g \quad (2.2)$$

Where T_x is the temperature for the onset of crystallization. As the temperature decrease from T_m , the rate of crystallization will increase rapidly but then fall rapidly as the temperature decrease below T_g . So that if we quenched a molten alloy rapidly enough to temperature below T_g a quasi-equilibrium amorphous phase is obtained. There is no direct relation between the easy of formation and the resultant stability of an amorphous alloy. The amorphous alloy composition most favorable for glass formation is near eutectic i.e. the composition in which the transformation from the liquid state to solid state takes place instantaneously without passing through liquid plus solid mixed phase. The deeper the eutectic the better is the glass formation ability [2.27]. There have been three approaches for relating the stability of the glass, i.e. its microstructure:

- (i) Barnaul's model of randomly packed hard sphere's [2.28]. The atoms of the metal are assumed to form a random network of close packed hard spheres and the smaller metalloid atoms fill the holes inherent in such structure.
- (ii) The effect of atomic sizes and inter atomic interactions [2.29], i.e. Chemical bonding suggested that it is chemical bonds which are dominating factors in glass formation and stability.
- (iii) The third approach [2.30] is based on the role of the electron gas and showed that under certain circumstances a nearly free electron gas will produce a barrier against crystallization.

The transition to the glassy state and the crystalline state is accompanied by an exothermic heat effect giving rise to a sharp peak in temperature dependence of the heat flow. Therefore, DTA is a widely used technique to study thermally induced transformations in amorphous alloys and to determine T_g and T_x . The magnitude of T_g and T_x are very different for amorphous materials and depend strongly on composition. The activation energy ranges typically between 2 and 6 eV [2.31].

2.3.2 Characteristics of the Glass Transition Temperature

When the time scale of molecular rearrangements occurs glass transition temperature (T_g) are too long for equilibrium to be maintained:

- (i) T_g means the time scale of the experiment matters.

- (ii) A high frequency/short time scale experiment allows less long for equilibrium to be established – even for an identical cooling rate.
- (iii) NMR (high frequency technique 10^{15} Hz.) always measures a higher T_g than DTA (1 Hz.).
- (iv) In the glass itself, entropy is similar to the crystal and original in vibrational modes, which are still present.
- (v) Long range transitional motions are frozen out. The temperature T_g configuration relaxation (including translational motion) but vibrational relaxations are still in equilibrium.
- (vi) T_g decreases as melt cooled more and more slowly.
- (vii) When the timescale of the experiment and the configuration relaxation time coincide, begin to see departure from equilibrium.
- (viii) The time scale for configuration relaxation will be related to rotational or translational diffusion coefficient.
- (ix) Optional definition of T_g is when the viscosity of the super-cooled liquid exceeds 10^{13} NSm⁻². Where as in the liquid there is an Arrhenius type with a Boltzmann factor containing activation energy.

2.4 Differential Thermal Analysis and its Application

Differential thermal Analysis (DTA) is an important technique for the study of structural change both in solid and liquid materials under heat treatment. During this process, the temperature difference between a substance and reference material is measured as a function of temperature whilst the subject and the reference material are subjected to some controlled temperature program. The transition of an amorphous or glassy state to crystalline state is accompanied by an exothermic heat effect that gives rise to a sharp peak in temperature dependence of the heat flow. To study this thermally induced transformation in amorphous alloys, DTA is a widely used technique. DTA detects the release or absorption as they are heated or cooled. Such information is essential for understanding thermal properties of materials. Analysis of decomposition of glass materials, crystalline phase changes, chemical reactions and glass transition temperature are some of the properties with DTA.

Amorphous alloys are in a metastable state and tend to transition into stable crystalline phases. At temperature below the crystallization temperature, structural

relaxation effect takes place which are caused by atomic rearrangements. DTA is an important technique for the study of structural change both in solid and liquid materials under heat treatment. The principle of DTA is widely used to understand the crystallization nature of the amorphous. Differential thermal analysis is a direct and effective technique for analyzing the kinetics of amorphous materials and stability with respect to crystallization process.

The crystallization is associated with the nucleation and growth process. Since the formation of an amorphous alloy depends on the absence of LRO, change of composition is expected to affect T_g and T_x . This is because long range ordering of atoms depends on the free energy difference between the crystalline state and the amorphous state. The magnitude of T_g and T_x are very different for amorphous materials and depend strongly on composition. Using DTA technique it is possible to determine T_g and T_x . Nanocrystalline amorphous ribbons prepared by rapid quenching method have been subjected to DTA using a Shimadzu Thermal Analyzer. Different peaks, crystallization temperatures, crystallization activation energies are obtained from this analysis.

2.4.1 Evaluation of Activation Energy Based on DTA Technique

Based on the work of Murray and White [2.32 – 2.34], the kinetics of materials can be understood by interpretation of DTA patterns of the materials. The dependence of T_x on the heating rate $\beta = \frac{dT}{dt}$ can be used to determine the activation energy of crystallization [2.35]. Considering the fraction x of amorphous material transformed into the crystalline state in time t and at temperature T obtains for the first-order rate process [2.36 - 2.37]

$$\left(\frac{\delta x}{\delta t}\right)_T = K(1 - x) \quad (2.3)$$

For thermally activated process, the rate constant K obeys an Arrhenius type of equations

$$K = K_o e^{-\left(\frac{\Delta E}{RT}\right)} \quad (2.4)$$

where K_o is a constant and ΔE is the activation energy. Combining equation (2.3) and (2.4) and using $dx = \left(\frac{\delta x}{\delta t}\right)_T dt + \left(\frac{\delta x}{\delta t}\right)_t dT$ with $\left(\frac{\delta x}{\delta t}\right)_t dt \cong 0$, are obtains

$$\frac{dx}{dt} = K_o(1-x)e^{-\left(\frac{\Delta E}{RT}\right)} \quad (2.5)$$

$$\begin{aligned} \frac{d^2x}{dt^2} &= \frac{d}{dt} \left[K_o(1-x)e^{-\left(\frac{\Delta E}{RT}\right)} \right] \\ &= -K_o \frac{dx}{dt} e^{-\left(\frac{\Delta E}{RT}\right)} + K_o(1-x) \frac{d}{dT} \left\{ e^{-\left(\frac{\Delta E}{RT}\right)} \right\} \frac{dT}{dt} \\ &= -K_o \frac{dx}{dt} e^{-\left(\frac{\Delta E}{RT}\right)} + \frac{dx}{dt} \left(\frac{\Delta E}{RT^2} \right) \beta \end{aligned}$$

At the peak of the exothermic heat, the change of the reaction rate $\frac{d^2x}{dt^2} = 0$, yielding with $T = T_x$ but $\frac{dx}{dt} \neq 0$

$$K_o e^{-\left(\frac{\Delta E}{RT_x}\right)} = \left(\frac{\Delta E}{RT_x^2} \right) \beta \quad (2.6)$$

From equation (2.6) it is easily seen that

$$\frac{d\left(\ln \frac{\beta}{T_x^2}\right)}{d\left(\frac{1}{T_x}\right)} = -\frac{\Delta E}{R} \quad (2.7)$$

Here $\beta = \frac{dT}{dt}$ the heating rate. ΔT_x for the stability of amorphous alloys as given by equation (2.5) and is obtained from DTA. Similar correlation between thermal stability as measured by ΔT_x and ΔE appears too small.

From the measured data of the heating rate (β) and the respective crystallization temperature (ΔT_x), the activation energy can be deduced from the slope of a plot $\ln \frac{\beta}{T_x^2}$ versus $\frac{1}{T_x}$ from equation (2.7) can be derived from transformation theory, where ΔE is the activation energy for versus flow and other terms have been omitted because they an insignificant temperature dependence in this region of temperature. The values of ΔE also appear to correlate well with the number of atomic species in the alloy; the more complex the alloy the grater is ΔE .

2.5 Determination of Nanometric Grain Size by X-Ray Diffraction

Nanocrystalline alloys are basically crystalline and because of their crystallinity and they exhibit Bragg scattering peaks in X-ray diffraction experiments. However, due to their small size, significant fine particle broadening is observed in

the Bragg peaks. The X-ray scattering from a crystalline solid is given by Bragg's law:

$$2d \sin \theta = n\lambda \quad (2.8)$$

This equates the path difference scattered from parallel crystalline planes spaced $d = d_{hkl}$ apart to an integral number (n) of X-Ray wavelength λ . Here θ is the X-Ray angle of incidence (and of diffraction) measured with respect to the crystalline planes. Bragg scattering occurs at discrete values of 2θ satisfying the Bragg condition for an infinite crystal, i.e. Bragg peaks are δ -functions. The peaks are broadened over a range of angles for finite sized crystals as shown in Figure 2.5.

The better understand of the phenomenon of fine particle broadening following argument of Cullity [2.38] is outlined below. We consider a finite crystal of thickness, $D_g = md$, where m is an integer and d is the distance between crystalline planes, i.e., there are m planes in D_g . considering Figure 2.5, if the broadened Bragg peak begins at an angle $2\theta_2$ and ends at $2\theta_1$, the breadth of the peak or full width at half maximum is given as:

$$\beta = \frac{1}{2}(2\theta_1 - 2\theta_2) = \theta_1 - \theta_2 \quad (2.9)$$

Now consider the path differences for each of the two angles θ_1 and θ_2 , for X-rays travelling the full thickness of the crystal. The width β is usually measured in radians; intensity is equal to half the maximum intensity. As a rough measure of β , we can take half the difference between the two extreme angles at which the intensity is zero, which amounts to assuming that the diffraction line triangular in shape.

We now write the path difference equations for those two angles related to the entire thickness of the crystal rather to the distance between adjacent planes.

$$2D_g \sin \theta_1 = (m + 1)\lambda \quad (2.10)$$

$$2D_g \sin \theta_2 = (m - 1)\lambda \quad (2.11)$$

By the subtraction;

$$D_g (\sin \theta_1 - \sin \theta_2) = \lambda \quad (2.12)$$

$$2D_g \cos \left(\frac{\theta_1 + \theta_2}{2} \right) \sin \left(\frac{\theta_1 - \theta_2}{2} \right) = \lambda \quad (2.13)$$

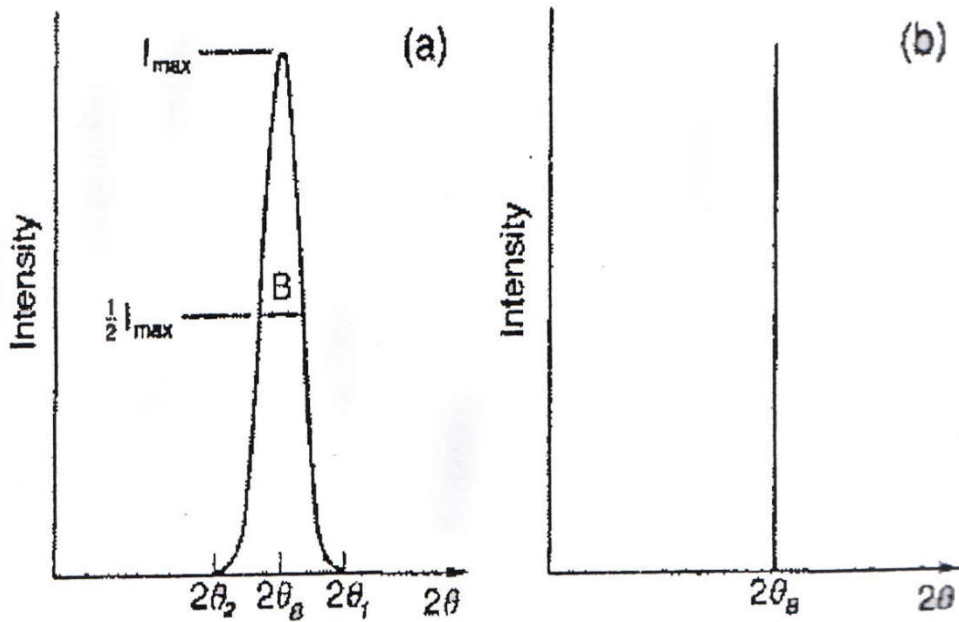


Figure 2.5 Effect of fine particle broadening in XRD (a) fine particle and (b) perfect crystal

But θ_1 and θ_2 are both very nearly equal to θ , so that $\theta_1 + \theta_2 \approx 2\theta$ and $\sin\left(\frac{\theta_1 - \theta_2}{2}\right) \approx \left(\frac{\theta_1 - \theta_2}{2}\right)$ thus the equation(2.13) can be written as:

$$2D_g \cos\theta \cdot \left(\frac{\theta_1 - \theta_2}{2}\right) = \lambda \quad (2.14)$$

From the equation (2.9) and equation (2.14) we get:

$$\beta \cdot D_g \cos\theta = \lambda \quad (2.15)$$

$$D_g = \frac{\lambda}{\beta \cos\theta} \quad (2.16)$$

A more exact empirical treatment yields:

$$D_g = \frac{0.9\lambda}{\beta \cos\theta} \quad (2.17)$$

This is known as the Scherer's formula. It is used to estimate the particle size of very small crystals from the measured width of their diffraction curves.

2.5.1 Random Anisotropy Model (RAM)

The degree to which the magnetocrystalline anisotropy is finally averaged out has been explained in detail in terms of the ‘Random Anisotropy Model (RAM)’ is proposed by Herzer [2.39 - 2.40] for the soft magnetic properties based on FINEMET type of nanocrystalline alloys. Soft magnetic properties of nanocrystalline alloys are strongly dependent on the grain size and grain boundary structure. In order to interpret the behavior of the magnetic properties for atomic scale grains, the RAM was originally proposed by Alben *et al.* [2.40] for amorphous ferromagnets. A theoretically more sophisticated treatment can be found in the paper of [2.42]. The basic idea is sketched in Figure 2.6 and starts from an assembly of ferromagnetically coupled grains of size D_g with magneto crystalline anisotropies K_1 oriented at random.

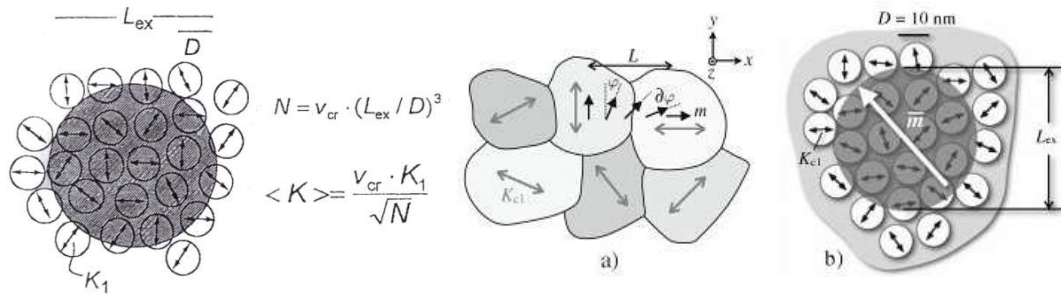


Figure 2.6 Schematic representation of Random Anisotropy Model (RAM) (a) Assembly of grains, each of them is having a randomly fluctuating anisotropy axis (b) The correlation volume of size L_{ex} in nanocrystalline material consisting of grains

The concept of a magnetic exchange length (L_{ex}) and its relationship to the domain wall width (δ_w) and nano domain size is important in the consideration of magnetic anisotropy in nanocrystalline soft magnetic materials [2.43]. These can be defined by applying to a Helmholtz free energy function as described by Coey [2.44]. These length scales are:

$$\delta_w = \pi \sqrt{\frac{A}{K_1}} \text{ And } L_{ex} = \sqrt{\frac{A}{4\pi M_s^2}} \quad (2.17)$$

Herzer consider a characteristic volume whose linear dimension is the magnetic exchange length $L_{ex} \sim \left(\frac{A}{K_1}\right)^{\frac{1}{2}}$, where K_1 is the nanocrystalline anisotropy. The unstated constant of proportionality should be $\left(\frac{k}{\pi}\right)$ which for materials with very

small K_1 can in fact be quite large. Ignoring this constant of proportionality, the Herzer's argument considers N grains, with random easy axes, within a volume of L_{ex}^3 to be exchange coupled. Since the easy axes are randomly oriented, a random walk all over N grains will yield an effective anisotropy which is reduced by a factor of $\left(\frac{1}{N}\right)^{\frac{1}{2}}$ from the value K_1 for any one grain, thus $K_{eff} \approx \frac{K_1}{\sqrt{N}}$. Now the number of grains in this exchange coupled volume is just $N \approx \left(\frac{L_{ex}}{D_g}\right)^3$, where D_g is the average diameter of individual grains. The ferromagnetic correlation volume $V = L_{ex}^3$ is determined by the exchange length L_{ex} . The results from averaging over the $N = V_{cr} \left(\frac{L_{ex}}{D_g}\right)^3$ grains, volume fraction V_{cr} relevant to the magnetization process with magnetocrystalline anisotropy oriented at random. Treating the anisotropy self-consistently, then

$$K_{eff} = V_{cr} \frac{K_1}{\sqrt{N}} = V_{cr}^{\frac{1}{2}} K_1 \left(\frac{D_g}{L_{ex}}\right)^{\frac{3}{2}} \quad (2.18)$$

The ferromagnetic exchange length $L_o = \sqrt{\frac{A}{K_1}}$, the exchange length L_{ex} has to be normalized by substituting $4\pi M_s^2 = K_{eff}$ in equation (2.17) i.e. L_{ex} is self-consistently related to the average anisotropy by

$$L_{ex} = \left(\frac{A}{K_{eff}}\right)^{\frac{1}{2}} \quad (2.19)$$

Combining equation (2.18) and equation (2.19), we get

$$K_{eff} = \sqrt{V_{cr}} K_1 \left[\frac{D_g}{\sqrt{\frac{A}{K_{eff}}}} \right]^{1/2}$$

or $K_{eff} = \sqrt{V_{cr}} K_1 \left[\frac{D_g \sqrt{K_{eff}}}{\sqrt{A}} \right]^{3/2}$

or $K_{eff} = \sqrt{V_{cr}} K_1 \left[\frac{D_g \sqrt{K_{eff}}}{L_o \sqrt{K_1}} \right]^{3/2}$

or $K_{eff}^4 = V_{cr}^2 K_1^4 \frac{D_g^6 (\sqrt{K_{eff}})^6}{L_o^6 (\sqrt{K_1})^6}$

$$\begin{aligned}
\text{or } K_{eff}^4 &= V_{cr}^2 K_1^4 \frac{D_g^6 \sqrt{K_{eff}}^3}{L_0^6 K_1^3} \\
\text{or } K_{eff} &= V_{cr}^2 K_1 \left(\frac{D_g}{L_0}\right)^6 \\
\text{or } K_{eff} &= V_{cr}^2 K_1 \frac{D_g^6}{\left(\frac{A}{\sqrt{K_1}}\right)^6} \\
\text{or } K_{eff} &= V_{cr}^2 K_1 \frac{D_g^6}{A^3} K_1^3 \\
\text{or } K_{eff} &= V_{cr}^2 D_g^6 \frac{K_1^4}{A^3} \\
\text{or } K_{eff} &= \frac{V_{cr}^2 D_g^6 K_1^4}{A^3} \tag{2.20}
\end{aligned}$$

Since the coercivity can be taken as proportional to the effective anisotropy. This analysis leads to Herzer's prediction that the effective anisotropy and therefore the coercivity should grow as the 6th power of the grain size:

$$H_c \sim D_g^6 \tag{2.21}$$

Herzer noted that the Nanocrystalline grains must be exchange coupled for such a reduction in the coercivity to be realized. This to be contrasted with uncoupled particles that have an exchange length, comparable to the particle diameter are susceptible to super paramagnetic response.

The most significant feature predicted by the RAM is the strong variation K_{eff} with the 6th power of the grain size. Thus for $D_g \approx \frac{L_0}{3}$. i.e. grain sizes in the order of 10-15 nm, the magnetocrystalline anisotropy is reduced by three order magnitude towards a few J/m^3 , i.e. small enough to enable superior soft magnetic behavior.

The K_{eff} , essentially determines the magnetic softness, since H_c and inverse of initial permeability (μ) are proportional to K_{eff} . Therefore it is expected that these quantities have similar dependence on grain size and have been confirmed experimentally [2.44]. Herzer explained the size dependence of the H_c based on RAM considering the nanocrystalline materials as single phase magnetic system. Hernando *et. al.* [2.46] extended this model for two phase materials and was able to explain the thermal dependence of the coercivity [2.47 – 2.48]. Hernando has generalized RAM, taking into account the two phase character of nanocrystalline materials and it

explained the previously maintained hardening as well as other features which could not be understood without the generalization. Since the dimensions of the crystallites dictate the unique properties by controlling the annealing temperature of the specimens. The magnetic softness or hardness in respect of permeability is determined by the grain size, grain distribution and the volume fraction, which are developed on the amorphous matrix in the nanostructure system.

2.6 Magnetic Dipole Moments and Magnetization

The vast majority of soft magnetic materials have one or more of the ferromagnetic transition metal elements Fe, Co or Ni, or the rare earth metal Gd as a majority component. The vast majority of soft magnetic materials have one or more of the ferromagnetic transition metal element. The magnetic dipole moments of the elemental and alloy magnets are almost completely understood through the Band Theory of Solids [2.49]. The band theory of solids considers the broadening of localized atomic states with discrete eigen values into a continuum of states for more itinerant electrons over arrange of energies. The theory allows for calculation of energy dispersion (i.e. energy as a function of wave vector) and orbital angular momentum specific and spin-resolved densities of states. The calculation of spin-resolved energy band and densities of states allows for the dispersion of atom resolved magnetic dipole moments, therefore spontaneous magnetization of element and alloy magnetic solids. Among the success of the band theory descriptions of magnetic properties are:

- (i) The prediction of non-integral or half integral atomic dipole moments and resulting ground state magnetization in the metals and alloys.
- (ii) The prediction that band widths and exchange splitting (energy differences between spin up and spin down bands) are intimately dependent on magnetic coordination number and atomic volume.

The electronic potential is more accurately, but still not at the level of consideration of all individual electron-electron interactions. In densities of states are more structures within free electron model and in more accurate description of the magnetic states in solids. The results of band theory, in describing alloying affects on magnetic dipole moment in solid.

The variation of the mean atomic magnetic dipole moment as a function of composition in the transition metal alloy system. Spin resolved densities of states $g_+(E)$ and $g_-(E)$ for Co and Fe atoms, in an equi-atomic Fe Co alloy, as a function of energy (where the Fermi energy, E_F is taken as the Zero of energy). The number of spin up, n_+ and spin down, n_- electrons in each band can be calculated again by integrating these densities of state:

$$n_+ = \int_0^{E_F^+} g_+(E) dE \quad (2.22)$$

$$\text{and } n_- = \int_0^{E_F^-} g_-(E) dE \quad (2.23)$$

Here the Fermi energies, E_F , are the same and the zero's of energy are different for the two spin bands and the atom resolved (i.e. Fe and Co) magnetic dipole moments can be calculated as:

$$\mu_m = (n_+ - n_-)\mu_B \quad (2.24)$$

Knowledge of atomic values or alloy density, then allows for the direct calculation of the alloy magnetization

Table 2.1, summarizes the absolute zero and room temperature (where applicable) magnetizations and atomic dipole moments for some important transition metal and rare earth elemental magnets. Also shown Curie temperatures i.e. ferromagnetic ordering temperatures which are not ground state properties that directly calculable from the band theory [2.50].

Table 2.1 Spontaneous and room temperature magnetizations, magnetic dipole moments and Curie temperature for elemental ferromagnets

Element	$\mu_m@0K(\mu_B)$	$M_S@0K$ (G)	$M_S@RT$ (G)	$T_c(K)$
Fe	2.22	1740	1707	1043
Co	1.72	1446	1400	1388
Ni	0.606	510	485	627
Gd	7.63	2060	--	292
Dy	10.2	2920	--	88

2.6.1 Magnetization of the Nanocrystalline Ribbon

The saturation magnetization of a material at a temperature of 0 K is one of its basic properties. Measurements are usually expressed as average moment per magnetic atom in units of the Bohr magneton, μ_B as specific saturation magnetization for the amorphous alloy, σ_s in units for Am²/kg. The moments of most amorphous alloys are lower than those of the structural disorder on the moments is very small. This points out the importance of chemical instead of structural disorder. The reduction is least in B-based and highest in p-based glass. The observed moments on TM-M glasses can approximately fitted to a formula [2.49].

$$\mu = \left(\frac{\mu_{TM} C_{TM} - C_B - 2C_{sc} - 3C_{\rho}}{C_{Tm}} \right) \quad (2.25)$$

Where μ_{TM} is the magnetic moment of TM-M atoms, taken as 2.6, 1.6 and 0.6 respectively in Bohr magneto for Fe, Co and Ni. C's are respective concentrations. This clearly demonstrates the charge transfer from metalloid to d-band of transition metal and seems to suggest that 1, 2 or 3 electrons are transferred from each of B, Si (C, Ge) or P atom. The relative number of electrons donated can be listed as $-P_{13}C_7 > -S_{15}B_{10} > -P_{16}B_6AI_3 > -P_{14}B_{13} > -B_{20}$ Based on the relative magnitudes of M_s .

2.6.2 Ferromagnetic ordering (Curie) Temperatures

Ferromagnetism is a collective phenomenon since individual atomic moments interact so as to promote alignment with one another. This collective interaction gives rise to the temperature dependence of the magnetization. Two models have explained the interaction between atomic moments. Mean Field Theory considers the existence of a non-local internal magnetic field, called the Weiss field, which acts to align magnetic dipole moments even in the absence of an applied field H_a . Heisenberg Exchange Theory considers a local (usually nearest neighbor) interaction between atomic moments (spins) which acts to align adjacent moments even in the absence of a field.

The basic assumption of the mean field theory is that this internal field is non-local and is directly proportional to the sample magnetization.

$$H_{INT} = \lambda_w M \quad (2.27)$$

Where the constant of proportionality, λ_w , is called the Weiss molecular field constant.

To consider ferromagnetic response in applied field, H_a , as well as the randomizing effects of temperature, we consider the superposition of the applied and internal magnetic fields. By analogy with the problem of paramagnetic moments, the average atomic dipole moment can be expressed in terms of the Brillouin function

$$\langle \mu_m \rangle = \mu_m^{atom} B_J(\alpha') \quad (2.28)$$

where $\alpha' = -\left(\frac{\mu_0 \mu_m^{atom}}{K_B T}\right)(H + \lambda_w M)$ for a collection of classical dipole moments. The saturation magnetization

$$M_s = N_m \langle \mu_m^{atom} \rangle \quad (2.29)$$

$$\frac{M}{N_m \mu_m^{atom}} = \frac{M}{M_s} = B_J[H + \lambda_w M] \quad (2.30)$$

Under appropriate conditions, this leads to solutions for which there is a non-zero magnetization (spontaneous magnetization) even in the absence of an applied field.

For $T > T_c$, the ferromagnetic T_c the only solution to equation (2.30) is $M = 0$, i.e., no spontaneous magnetization and thus paramagnetic response. For $T < T_c$, we obtain solutions with a non-zero, spontaneous magnetization, the defining feature of a ferromagnet.

The Heisenberg model considers ferromagnetism and the defining spontaneous magnetization to result from nearest neighbor exchange interactions, which acts to align spins in a parallel configuration, instead of a non-local, mean field. The Heisenberg model can be further generalized to account for atomic moments of different magnitude and signs, i.e. in alloys, and for exchange interactions which act to align nearest neighbor moments in an anti-parallel fashion or in a noncollinear relationship. Consider Heisenberg ferromagnet; assume that the atomic moments due to a spin vector S on nearest neighbor sites are coupled by a nearest neighbor exchange interaction that gives rise to a potential energy

$$E_p = -J_{ex} S_i \times S_{i+1}, \quad (2.31)$$

That for $J_{ex} > 0$ favors parallel alignment of the spins. The exchange suitably scaled, replaces the Weiss molecular field constant in the mean field theory of ferromagnetism to explain the temperature dependence magnetization.

Ferromagnetic exchange interactions set the scale for T_c in ferromagnetic alloys. Inter atomic exchange couplings can be calculated from first principles by considering the energy change associated with rotation of individual spins in the host material. These exchange interactions can be used within a mean field theory to estimate the T_c . Empirical descriptions of the variations of the exchange energy with inter atomic spacing called the Bethe-Slater curve is instructive in describing the effect of alloying on ferromagnetic T_c . The interplay between electron-electron Coulomb interactions and the constraints of the Pauli's exclusion principle determine the sign of the exchange interaction.

In transition metal solids a measure of the overlap between nearest neighbor d-orbital is given by the ratio of the atomic to the 3d ionic (or nearest neighbor) radius. In mean field theory the T_c can be related to the exchange energy as follows:

$$T_C = \frac{2S(S+1)}{3K_B} \sum_{ij} T_{ij}, \quad (2.32)$$

where S is the total spin angular momentum, K_B is the Boltzmann's constant and T_{ij} is the exchange interaction between atoms at the position r_i and r_j .

In first case, a unique constant exchange interaction between the magnetic atoms is assumed and the amorphous nature of the alloy is taken into account by calculating a random distribution of the local anisotropy field [2.51]. In the second approach is treating this problem of distribution of exchange integrals assumed in order to reflect the structural fluctuations in the amorphous alloy [2.52]. Both approaches predict that M vs. T curve will flat below that for the crystalline counterpart.

RESULTS AND DISCUSSION

4.1 Crystallization Behavior of Fe-X-Nb-Si-B Alloys

The microstructural changes and crystallization processes in Fe-Si-B amorphous alloys in order to elucidate the roles of combined additions of Cu and Nb to Fe-Si-B alloys. If the amorphous alloy is used as a production of nanocrystalline FINEMET of composition Fe-X-Nb-B-Si [$X = \text{Cu, Au \& Ag}$] then the primary and secondary crystallization temperatures are of importance. Koster and Meinhardt [4.1] have studied primary crystallization of FINEMET and shown that a size dependent growth rate can be observed to the changing chemistry of the amorphous phase during the evolution of the microstructure. Microstructural control is achieved through the additions of slow diffusing species such as Nb while small Cu or Au or Ag additions increase the nucleation rate. Kulik *et. al.* [4.2] have also investigated B substitutions for Si in FINEMET type. The softest magnets corresponds to those in which primary crystallization of $\alpha\text{-Fe(Si)}$ and Fe_3Si occurred. Secondary crystallization of Fe_2B caused magnetic hardening of the nanocrystalline alloy. Mechanical hardening of the amorphous precursor was also observed in incipient primary crystallization and attributed to Cu or Au or Ag nucleation or clustering.

The structure of the beneficial ferromagnetic nanocrystalline phase is composed of $\alpha\text{-Fe(Si)}$, which is the product of primary crystallization. The change of composition affects the growth kinetics in a complicated way, which can only be determined experimentally. The composition of the alloy affects both the primary and secondary crystallization phases, because the time needed for the constituent atom to have long range order depends on their bond energies [4.3-4.4]. Good soft magnetic properties of the materials require not only small grain size but at the same time the absence of boron compound. The separation between the primary crystallization of $\alpha\text{-Fe(Si)}$ phase and the secondary crystallization product of Fe_2B phase not only is determined by the Cu or Au or Ag and Nb addition but also on boron content, with the increase of boron content the separation between the two products decreases [4.5]. We kept at a moderate level of boron content in the nominal composition in order to obtain an optimum nanoscaled structure.

Crystallization kinetics is often determined from Differential Scanning Calorimetry (DSC), Differential Thermal Analysis (DTA) and magnetic materials form Thermomagnetic Analysis (TMA) [4.6-4.8]. In the present investigation DTA

technique has been used to study the crystallization behavior of nanocrystalline amorphous alloys $\text{Fe}_{73.5}\text{X}_1\text{Nb}_3\text{Si}_{13.5}\text{B}_9$ [$\text{X} = \text{Cu}, \text{Au} \ \& \ \text{Ag}$]. DTA is a direct and effective technique for analyzing the kinetics of crystallization of amorphous materials. DTA has been performed to identify the crystallization temperatures as well as a activation energy required for crystallization. The X-ray diffraction experiment was undergone to identify the revolution of phases with heat treatment.

4.2 DTA Results of Fe-X-Nb-Si-B ribbons as affected by X = Cu, Au & Ag content

Crystallization is a non-reversible, exothermic process [4.9]. DTA is a direct and effective way to analyze the kinetics of nanocrystalline materials in respect of phase transition. Figure 4.1 displays the DTA traces with a heating rate of $50^\circ\text{C}/\text{min}$, where the primary crystallization and secondary crystallization peak temperature are well demonstrated for the $\text{Fe}_{73.5}\text{X}_1\text{Nb}_3\text{Si}_{13.5}\text{B}_9$ [$\text{X} = \text{Cu}, \text{Au} \ \& \ \text{Ag}$] nanocrystalline amorphous alloys in the form of ribbons, prepared by melt spinning technique. In each of the curves, two exothermic peaks are distinctly observed. Corresponding to different crystallization events initiated at temperature T_{x_1} and T_{x_2} respectively. The primary crystallization temperature T_{x_1} corresponds to evolution of nanocrystalline α -Fe(Si) phase which provides the expected soft magnetic properties. The secondary crystallization temperature T_{x_2} corresponds to the boride phase i.e. Fe_2B phase which cause magnetic hardening of nanocrystalline alloy. Thus, the identification of these two temperatures is necessary to understand the appropriate temperature range for the heat treatment in order to achieve the nanocrystalline phase and thereby, suitable range of temperature for the application of this alloy. The numerical values of T_{x_1} and T_{x_2} for all the samples are shown in Table 4.1.

It is observed from figure 4.1, that the crystallization of each phase has occurred over a wide range of temperatures and the primary crystallization temperature shifts higher temperatures as the replace $\text{Ag} > \text{Cu} > \text{Au}$ concentration. The crystallization temperature (T_{x_1} and T_{x_2}) and the peak temperatures (T_{p_1} and T_{p_2}) are for this condition $\text{Au} < \text{Cu} < \text{Ag}$. Both are the samples display exothermic peak, i.e. release of heat during the crystallization of α -Fe(Si) and Fe_2B phase since the transition from amorphous solid to crystalline solid is an exothermic process.

Table 4.1 Onset temperature of 1st and 2nd crystallization states of the nanocrystalline amorphous ribbons with composition $\text{Fe}_{73.5}\text{X}_1\text{Nb}_3\text{Si}_{13.5}\text{B}_9$ [X = Cu, Au & Ag] alloy during continuous heating rate $50^\circ\text{C}/\text{min}$.

Samples	1 st starting T_{x_1} °C	1 st Peak T_{p_1} °C	2 nd starting T_{x_2} °C	2 nd Peak T_{p_2} °C	$T_{x_2}-T_{x_1}$ in °C	$\Delta T = T_{p_2}-T_{p_1}$ in °C
X = Cu	530.1	558	689.9	710.2	159.8	152.2
X = Au	516	583	668	699	152	116
X = Ag	571	614.2	750	780	179	165.8

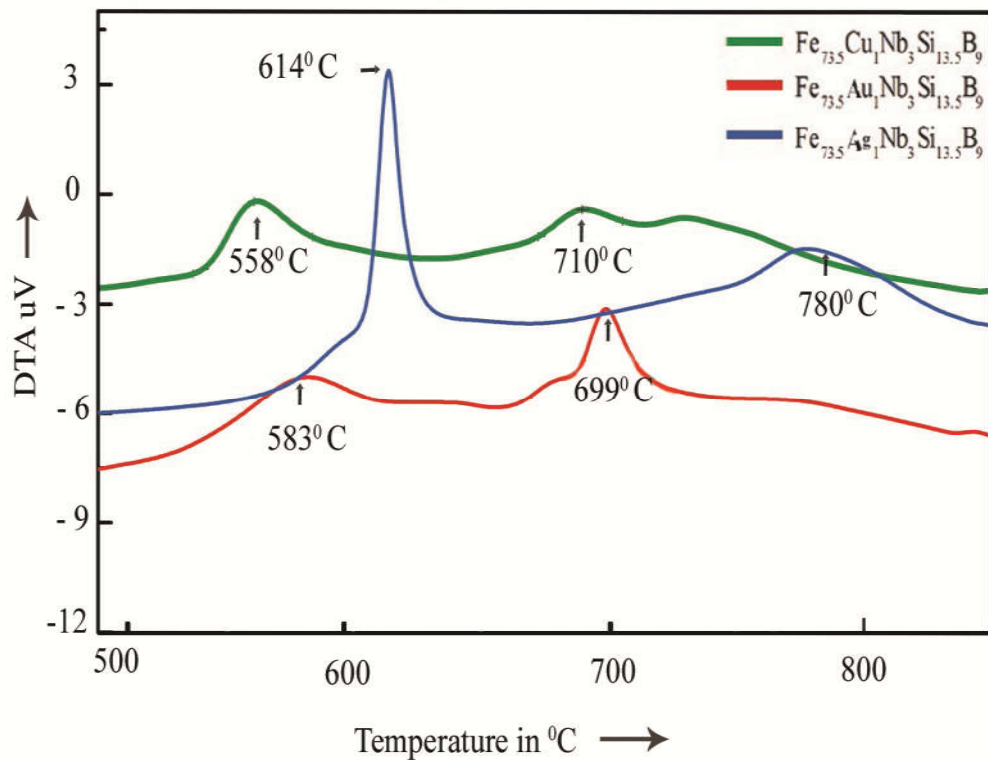


Figure 4.1 DTA traces of as-cast nanocrystalline amorphous ribbon $\text{Fe}_{73.5}\text{X}_1\text{Nb}_3\text{Si}_{13.5}\text{B}_9$ [X = Cu, Au & Ag] at the heating rate of $50^\circ\text{C}/\text{min}$.

From the DTA data it is also understood that the temperature difference between the two crystallization peaks (ΔT) process are Au ($\Delta T = 116^\circ\text{C}$) <

$\text{Cu}(\Delta T = 152.2^\circ\text{C}) < \text{Ag}(\Delta T = 165.8^\circ\text{C})$. This large difference is due to Ag content in sample $\text{Fe}_{73.5}\text{Ag}_1\text{Nb}_3\text{Si}_{13.5}\text{B}_9$, which influenced the shift of T_{p_2} to higher temperature. Since Cu helps nucleation of $\alpha\text{-Fe}(\text{Si})$ phase and Nb delays the formation of Fe_2B phase [4.10], the observed anomalies of crystallization temperature in this studied samples are clearly understood from their constant Cu content replace with Ag or Au. These are noted that the whole process of crystallization takes place over a wide range of temperatures. This signifies that the nucleation and growth of crystallites are faster in the initial stage of crystallization, which gradually becomes sluggish with the increase of volume fraction of crystallites with condition $\text{Ag} > \text{Cu} > \text{Au}$. The growth of crystallites involves diverse processes due to which the exothermic peaks are asymmetric as affected by various growth rates. Therefore the role of Cu replace by Ag or Au in FINEMET on the crystallization behavior in these three samples is well understood nanocrystalline amorphous ribbons.

4.2.1 DTA Results of Nanocrystalline Amorphous Ribbons with Composition $\text{Fe}_{73.5}\text{Cu}_1\text{Nb}_3\text{Si}_{13.5}\text{B}_9$

DTA traces of as-cast nanocrystalline amorphous ribbon $\text{Fe}_{73.5}\text{Cu}_1\text{Nb}_3\text{Si}_{13.5}\text{B}_9$ alloy taken in nitrogen atmosphere with the heating rates of $10^\circ\text{C} - 50^\circ\text{C}/\text{min}$. at the step of 10°C with continuous heating from room temperature to 800°C , are presented in Figure 4.2(a) to Figure 4.2(e) respectively. In each of the figure, two exothermic peaks are distinctly observed which corresponds to two different crystallization events at temperature T_{x_1} and T_{x_2} respectively. The softest magnetic ribbon corresponds to those in which primary crystallization (T_{x_1}) of $\alpha\text{-Fe}(\text{Si})$ takes place. Secondary crystallization (T_{x_2}) of Fe_2B caused magnetic hardening of the nanocrystalline alloy. Two anomalies observed in the DTA are followed by sharp peaks, which corresponds to the release of heat at these temperatures due to change in the ordering of atoms. Mechanical hardening of the amorphous precursor has been observed in incipient primary crystallization and attributed to Cu nucleation. Phase identification cannot be done from a DTA scan. XRD has been used for the identification of phases and would be discussed later on.

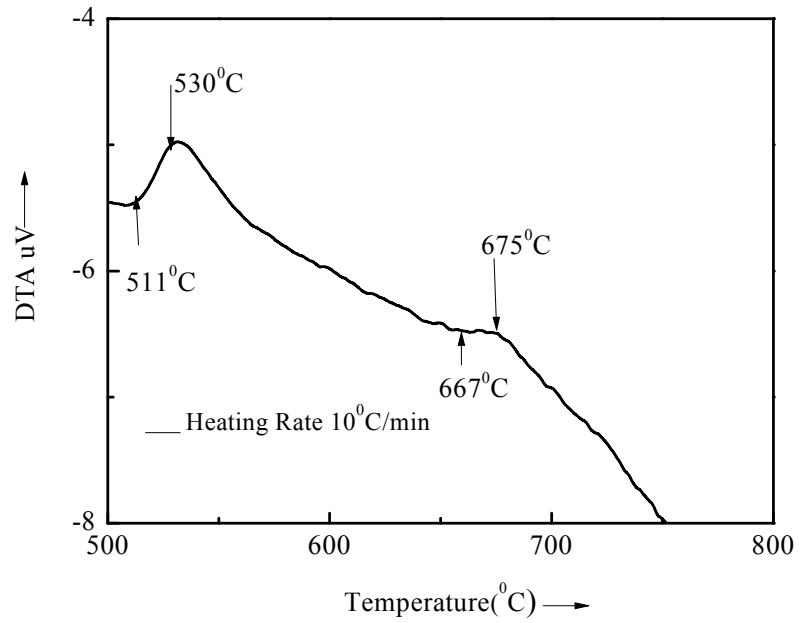


Figure 4.2(a) DTA trace of as-cast nanocrystalline amorphous ribbon $\text{Fe}_{73.5}\text{Cu}_1\text{Nb}_3\text{Si}_{13.5}\text{B}_9$ at the heating rate of $10^\circ\text{C}/\text{min}$

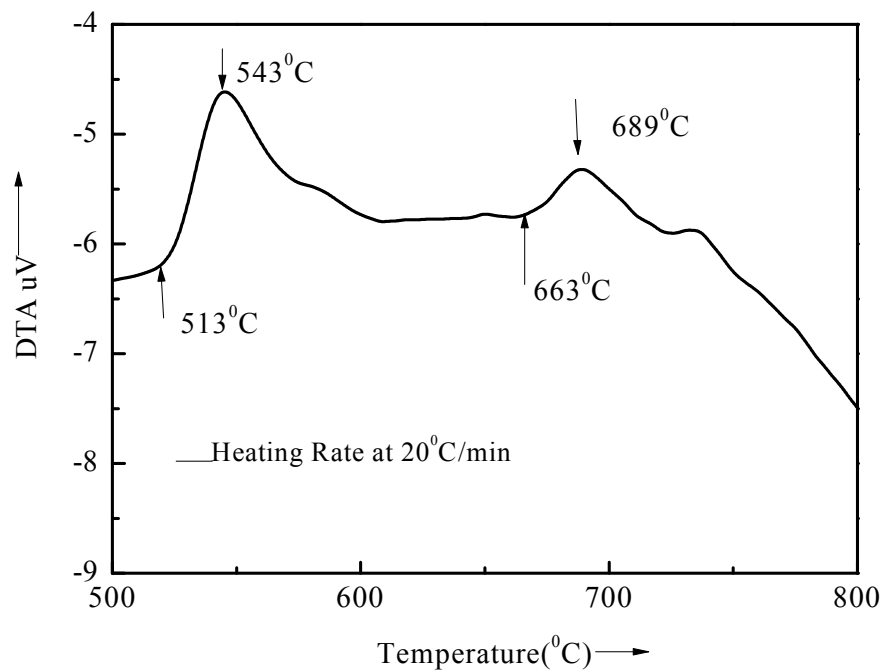


Figure 4.2(b) DTA trace of as-cast nanocrystalline amorphous ribbon $\text{Fe}_{73.5}\text{Cu}_1\text{Nb}_3\text{Si}_{13.5}\text{B}_9$ at the heating rate of $20^\circ\text{C}/\text{min}$

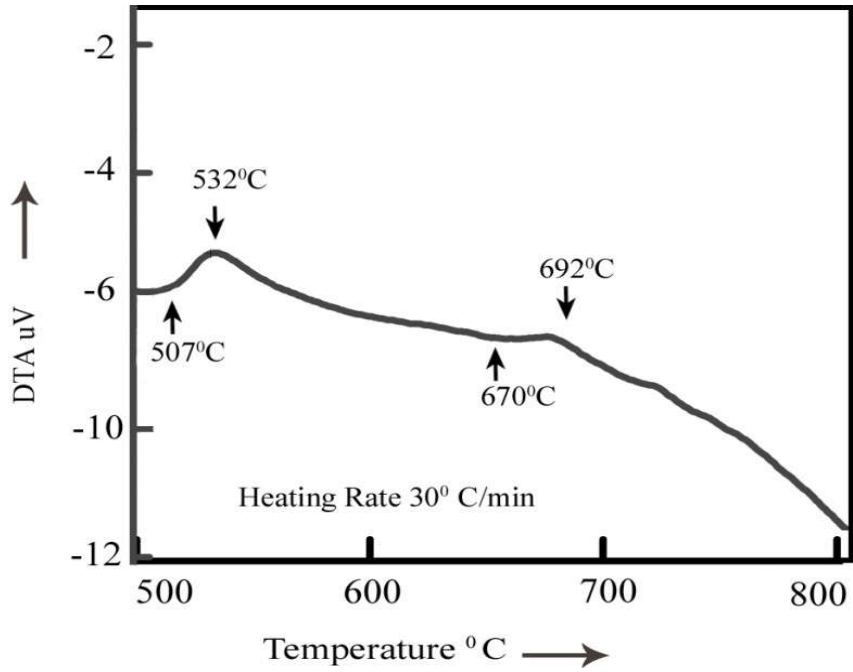


Figure 4.2(c) DTA trace of as-cast nanocrystalline amorphous ribbon $\text{Fe}_{73.5}\text{Cu}_1\text{Nb}_3\text{Si}_{13.5}\text{B}_9$ at the heating rate of $30^\circ\text{C}/\text{min}$

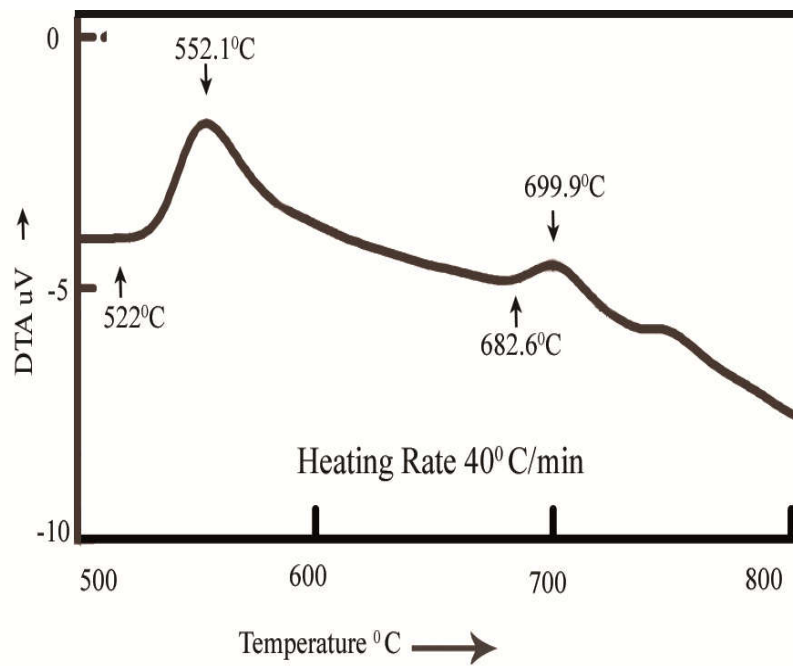


Figure 4.2(d) DTA trace of as-cast nanocrystalline amorphous ribbon $\text{Fe}_{73.5}\text{Cu}_1\text{Nb}_3\text{Si}_{13.5}\text{B}_9$ at the heating rate of $40^\circ\text{C}/\text{min}$

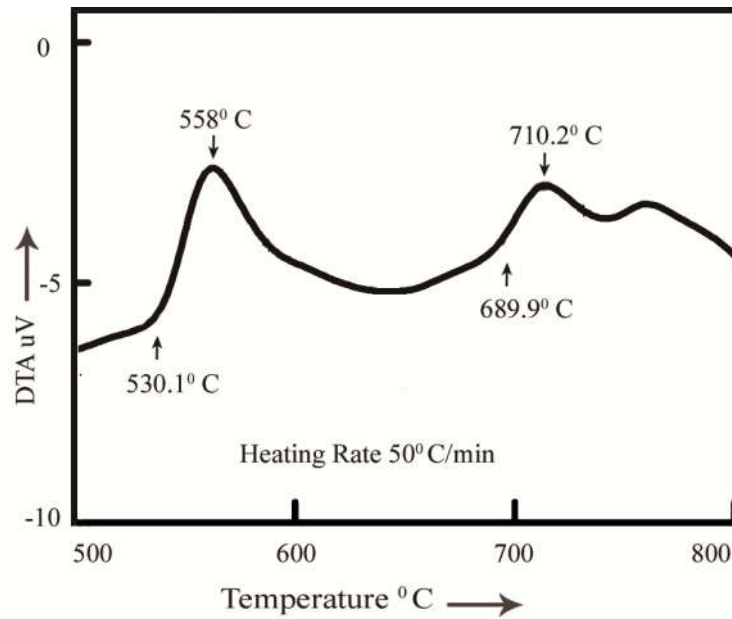


Figure 4.2(e) DTA trace of as-cast nanocrystalline amorphous ribbon $\text{Fe}_{73.5}\text{Cu}_1\text{Nb}_3\text{Si}_{13.5}\text{B}_9$ at the heating rate of $50^\circ\text{C}/\text{min}$

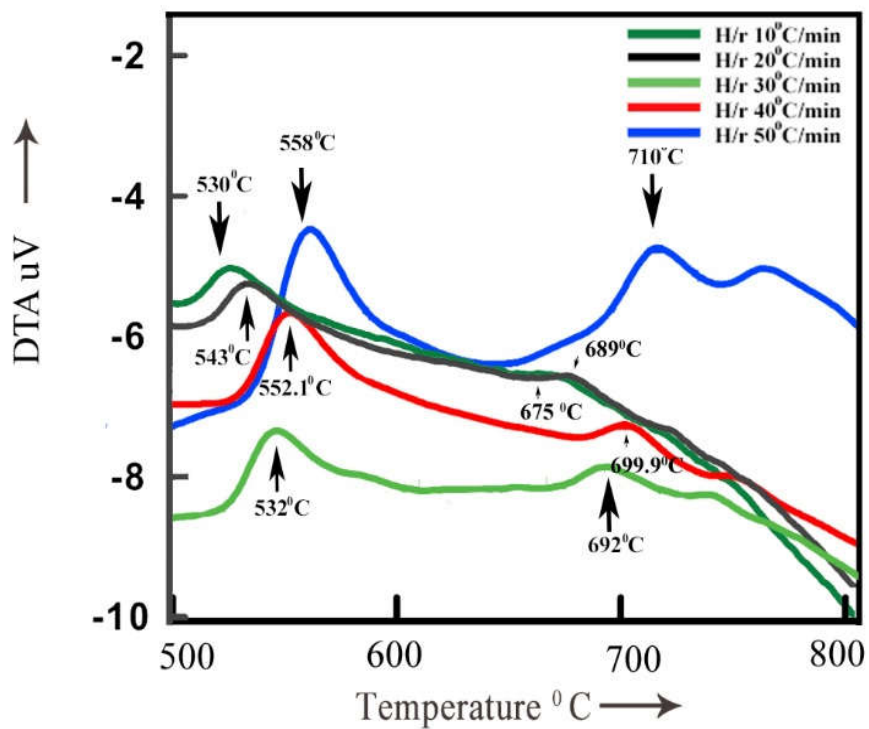


Figure 4.3 Effects of heating rate on DTA traces of nanocrystalline amorphous ribbons $\text{Fe}_{73.5}\text{Cu}_1\text{Nb}_3\text{Si}_{13.5}\text{B}_9$ at the heating rate of 10°C to $50^\circ\text{C}/\text{min}$

From Figure 4.3 represents a combination of all DTA traces of amorphous $\text{Fe}_{73.5}\text{Cu}_1\text{Nb}_3\text{Si}_{13.5}\text{B}_9$ ribbons. It is observed that the crystallization of each phase has occurred over a wide range temperatures and that the peak temperatures shift to higher values with the increase of heating rate. That means, it is requires more heat energy for the formation of crystalline phases with increasing heating rates. That means, it is requires more heat energy for the formation of crystalline phases with increasing heating rates.

From each of the DTA traces, it is obvious that the area under the first crystallization peak is larger than the area covered by the second crystallization peak. In the Table 4.2 crystallization peak temperatures of two phases (T_{p1} and T_{p2}) and crystallization onset temperatures of two phases (T_{x1} and T_{x2}) are given for different heating rates. It has been observed that the crystallization temperature range of first phase occurred within 19°C to 30.1°C but this range for the second crystallization phase is 18°C to 26°C . So it is notable that the crystallization temperature range for first peak is always larger than the second peak. It is also observed that the peak temperature shift to higher values and crystallization temperature range increase with the heating rates. From figure 4.3 it is seen that two crystallization phenomena have taken place within a large temperature gap of around 145°C to 160°C .

Table 4.2 Effect of heating rate on 1st and 2nd crystallization states of the nanocrystalline amorphous ribbon with composition $\text{Fe}_{73.5}\text{Cu}_1\text{Nb}_3\text{Si}_{13.5}\text{B}_9$

Heating rate $\beta^\circ\text{C}/\text{min}$	1 st starting $T_{x1}^\circ\text{C}$	1 st Peak $T_{p1}^\circ\text{C}$	Temperature range of 1 st state in $^\circ\text{C}$	2 nd starting $T_{x2}^\circ\text{C}$	2 nd Peak $T_{p2}^\circ\text{C}$	Temperature range of 2 nd state in $^\circ\text{C}$	T_{x2} - T_{x1} In $^\circ\text{C}$	T_{p2} - T_{p1} In $^\circ\text{C}$
10	511	530	19	667	675	18	127	145
20	513	543	30	663	689	26	150	146
30	507	532	25	670	692	22	163	160
40	522	552.1	30.1	682.6	699.9	17.3	160.0	147.8
50	530.1	558	27.9	689.9	710.2	20.3	159.8	152.2

The activation energy of crystallization of T_{x1} and T_{x2} phases have been calculated using Kissinger equation [4.11].

$$\beta = T_p^2 e^{-E/KT_p}$$

$$\ln\left(\frac{\beta}{T_p^2}\right) = -\frac{E}{KT_p}$$

$$E = -KT_p \ln\left(\frac{\beta}{T_p^2}\right) \quad (4.1)$$

Where β is the heating rate, T_p is the crystallization temperature, E is the activation energy and K is the Boltzmann constant. The activation energy of $T_{x1}[\alpha\text{-Fe (Si)}]$ and $T_{x2}[\text{Fe}_2\text{B}]$ phases has been calculated from table 4.3 and using Kissinger's plot shown in figure 4.4(a) and figure 4.4(b). It shows that first thermal crystallization activation energy of $\alpha\text{-Fe (Si)}$ phase E_1 is 2.18 eV and second Fe_2B phase E_2 is 3.62 eV.

Table 4.3 Effect of heating rate on 1st and 2nd crystallization of the nanocrystalline amorphous ribbon with composition $\text{Fe}_{73.5}\text{Cu}_1\text{Nb}_3\text{Si}_{13.5}\text{B}_9$ state's calculative data for activation energy

Heating rate β °C/min	Heating rate β °K/min	1 st Peak T_{p1} °K	$\frac{1}{T_{p1}} \times 10^3$	$\ln(\beta/T_{p1}^2)$	2 nd Peak T_{p2} °K	$\frac{1}{T_{p2}} \times 10^3$	$\ln(\beta/T_{p2}^2)$
10	13.41	803.16	1.245	-10.78	948.16	1.055	-11.11
20	26.89	816.16	1.225	-10.12	962.16	1.039	-10.45
30	40.24	805.16	1.242	-9.69	965.16	1.036	-10.05
40	53.66	825.26	1.212	-9.45	973.16	1.028	-9.78
50	67.07	831.16	1.202	-9.24	983.16	1.107	-9.58

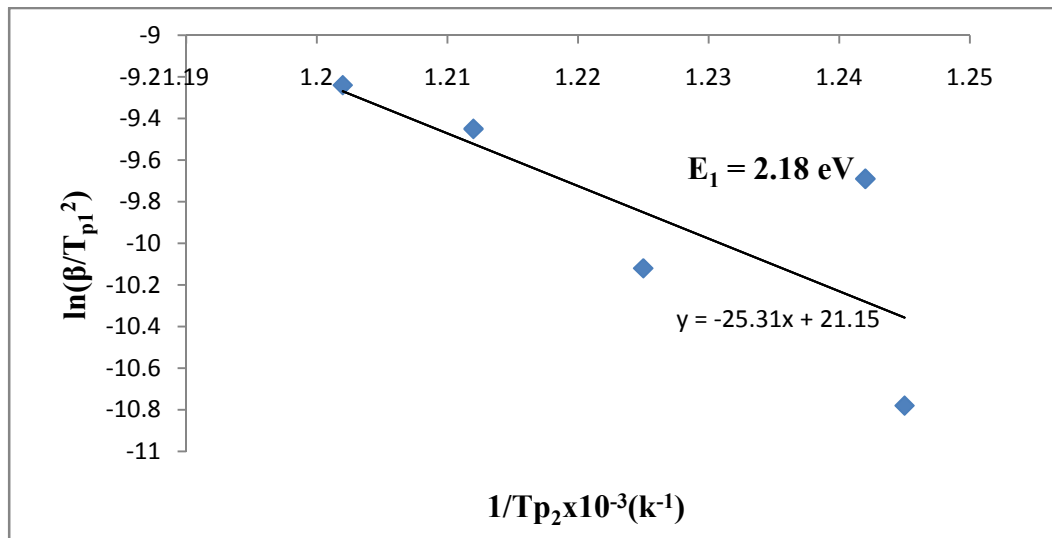


Figure 4.4(a) Kissinger's plot to determine the activation energy of Fe (Si) phase for $\text{Fe}_{73.5}\text{Cu}_1\text{Nb}_3\text{Si}_{13.5}\text{B}_9$ alloy

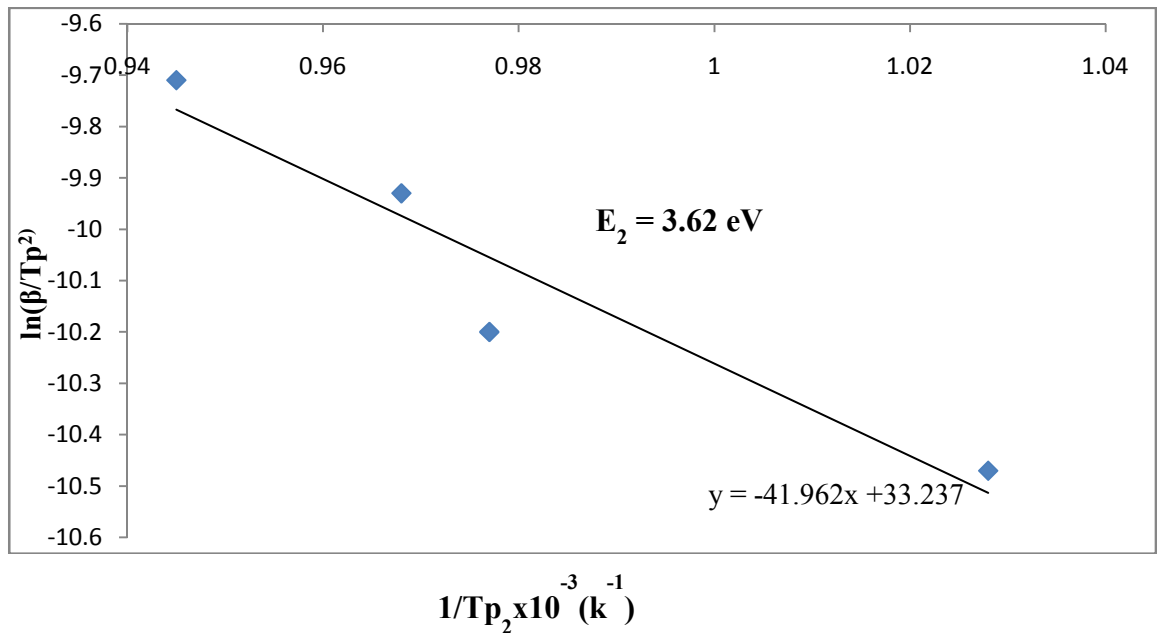


Figure 4.4(b) Kissinger's plot to determine the activation energy of Fe_2B phase for $\text{Fe}_{73.5}\text{Cu}_1\text{Nb}_3\text{Si}_{13.5}\text{B}_9$ alloy

4.2.2 DTA Results of Nanocrystalline Amorphous Ribbons with Composition $\text{Fe}_{73.5}\text{Au}_1\text{Nb}_3\text{Si}_{13.5}\text{B}_9$

DTA traces of as-cast nanocrystalline amorphous ribbon $\text{Fe}_{73.5}\text{Au}_1\text{Nb}_3\text{Si}_{13.5}\text{B}_9$ alloy taken in the nitrogen atmosphere with the heating rates of $10^\circ\text{C} - 50^\circ\text{C}/\text{minute}$ at the step of 10°C with continuous heating from room temperature to 800°C , are presented in figure 4.5(a) to figure 4.5(e) respectively. Two well defined exothermic peaks typical for two steps of crystallization processes are manifested from the DTA traces. The first one corresponds to the crystallization of $\alpha\text{-Fe(Si)}$ phase and the second one is related to the crystallization of Fe_2B . From figure 4.6 represents a combination of all DTA traces of amorphous $\text{Fe}_{73.5}\text{Au}_1\text{Nb}_3\text{Si}_{13.5}\text{B}_9$ ribbons. From each of the DTA traces, it is obvious that the area under the first crystallization peak is larger than the area covered by the second crystallization peak. In the Table 4.4 crystallization peak temperatures of two phases (T_{p1} and T_{p2}) and

crystallization onset temperatures of two phases (T_{x1} and T_{x2}) are given for different heating rates.

It is observed that the crystallization temperature range of first phase occurred within 31°C to 67°C but this range for the second crystallization phase is 8°C to 31°C . So it is notable that the crystallization temperature range for first peak is always larger than the second peak. It is also observed that the peak temperature shift to higher values and crystallization temperature range increase with the heating rates. From figure 4.5 it is seen that two crystallization phenomena have taken place within a temperature gap of around with in 112°C to 133°C . This temperature gap is smaller than the Cu replace Au substituted counterpart.

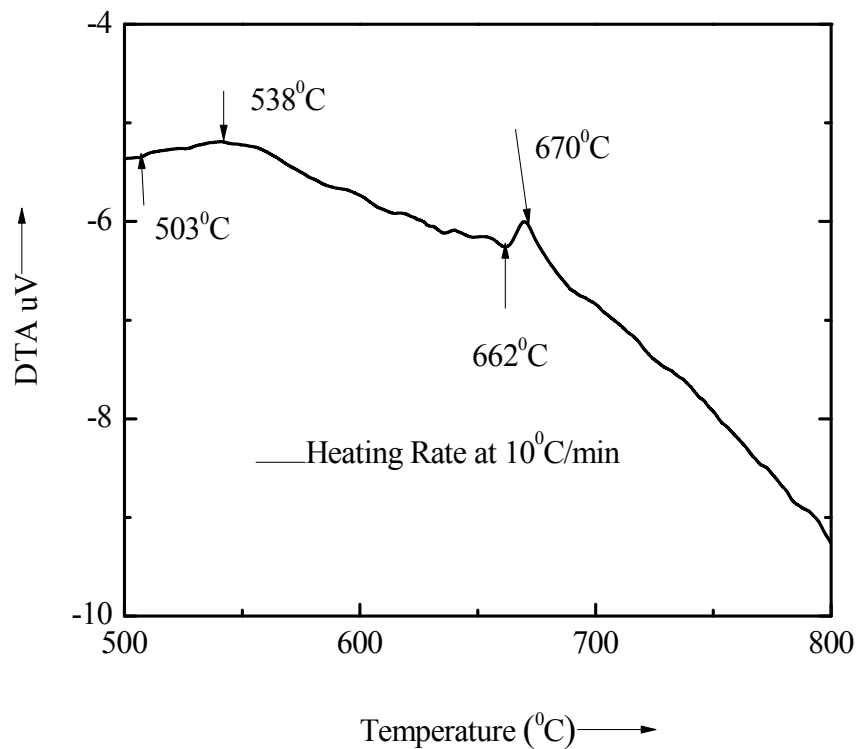


Figure 4.5(a) DTA trace of as-cast nanocrystalline amorphous ribbon $\text{Fe}_{73.5}\text{Au}_1\text{Nb}_3\text{Si}_{13.5}\text{B}_9$ at the heating rate of $10^{\circ}\text{C}/\text{min}$

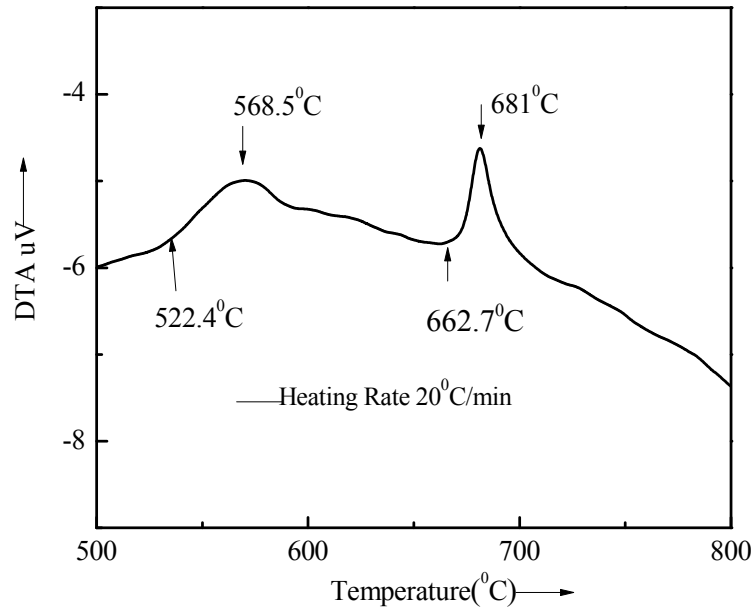


Figure 4.5(b) DTA trace of as-cast nanocrystalline amorphous ribbon $\text{Fe}_{73.5}\text{Au}_1\text{Nb}_3\text{Si}_{13.5}\text{B}_9$ at the heating rate of $20^\circ\text{C}/\text{min}$

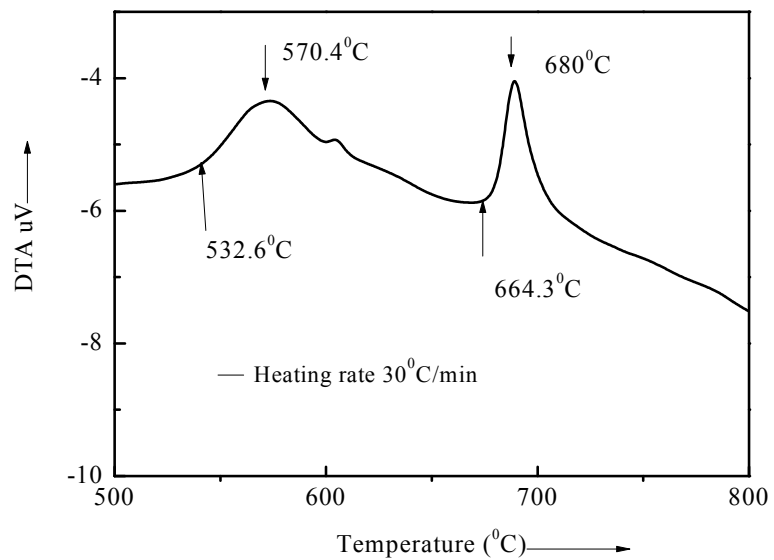


Figure 4.5(c) DTA trace of as-cast nanocrystalline amorphous ribbon $\text{Fe}_{73.5}\text{Au}_1\text{Nb}_3\text{Si}_{13.5}\text{B}_9$ at the heating rate of $30^\circ\text{C}/\text{min}$

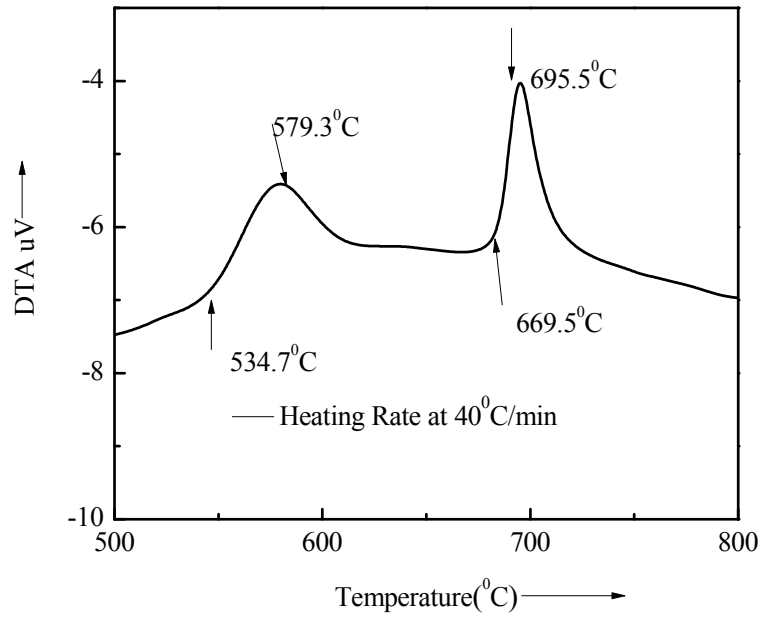


Figure 4.5(d) DTA trace of as-cast nanocrystalline amorphous ribbon $\text{Fe}_{73.5}\text{Au}_1\text{Nb}_3\text{Si}_{13.5}\text{B}_9$ at the heating rate of $40^\circ\text{C}/\text{min}$

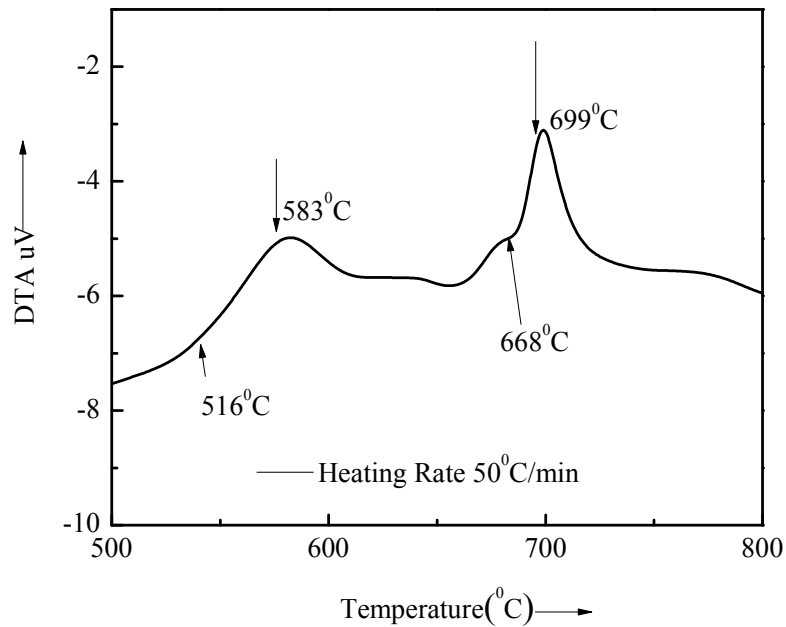


Figure 4.5(e) DTA trace of as-cast nanocrystalline amorphous ribbon $\text{Fe}_{73.5}\text{Au}_1\text{Nb}_3\text{Si}_{13.5}\text{B}_9$ at the heating rate of $50^\circ\text{C}/\text{min}$

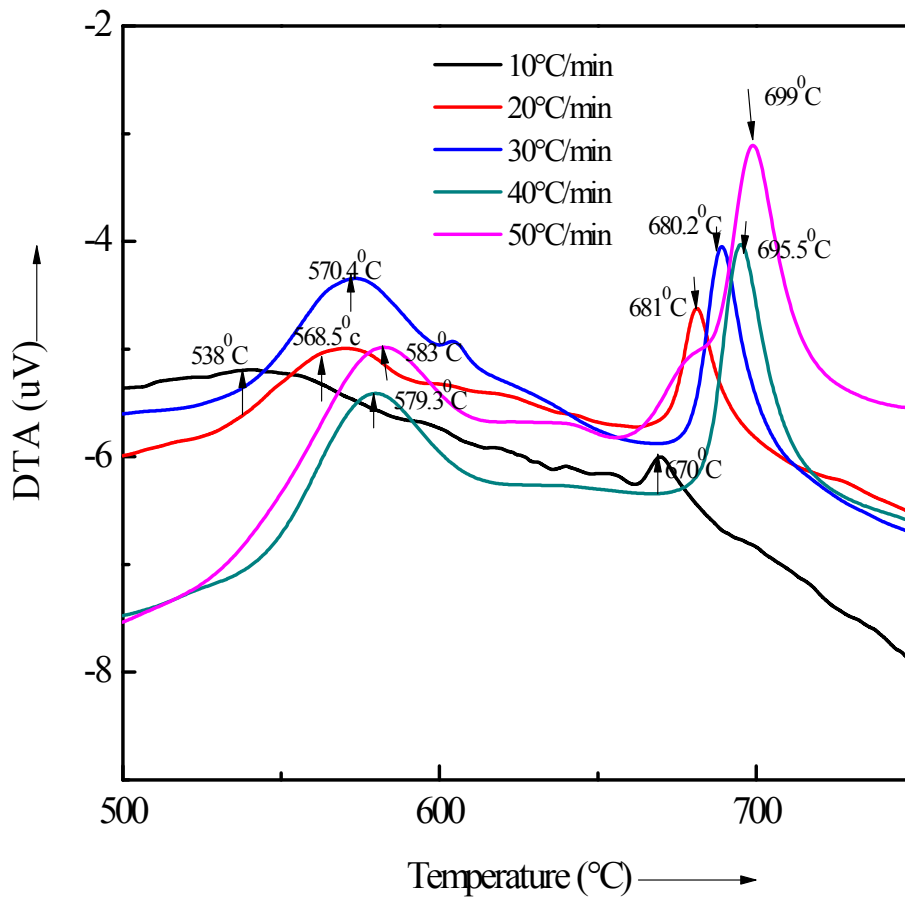


Figure 4.6 Effects of heating rate on DTA traces of nanocrystalline amorphous ribbon with composition $\text{Fe}_{73.5}\text{Au}_1\text{Nb}_3\text{Si}_{13.5}\text{B}_9$ at the heating rate of 10°C to $50^\circ\text{C}/\text{min}$

Table 4.4 Effect of heating rate on 1st and 2nd crystallization states of the nanocrystalline amorphous ribbon with composition $\text{Fe}_{73.5}\text{Au}_1\text{Nb}_3\text{Si}_{13.5}\text{B}_9$

Heating rate $\beta^\circ\text{C}/\text{min}$	1 st starting $T_{x_1}^\circ\text{C}$	1 st Peak $T_{p_1}^\circ\text{C}$	Temperature range of 1 st state in $^\circ\text{C}$	2 nd starting $T_{x_2}^\circ\text{C}$	2 nd Peak $T_{p_2}^\circ\text{C}$	Temperature range of 2 nd state in $^\circ\text{C}$	$T_{x_2} - T_{x_1}$ in $^\circ\text{C}$	$T_{p_2} - T_{p_1}$ in $^\circ\text{C}$
10	503	538	35	662	670	8	159	132
20	522.4	568.5	41.1	662.7	681	18.3	140.3	112.5
30	532.6	570.4	31.8	664.3	680.2	15.9	132.7	116.8
40	534.7	579.3	44.6	669.5	695.5	26	140.8	116.2
50	516	583	67	668	699	31	152	116

Table 4.5 Effect of heating rate on 1st and 2nd crystallization of the nanocrystalline amorphous ribbon with composition $Fe_{73.5}Au_1Nb_3Si_{13.5}B_9$ state's calculative data for activation energy

Heating rate $\beta^\circ C/min$	Heating rate $\beta^\circ K/min$	1 st Peak $T_{p_1}^\circ K$	$\frac{1}{Tp_1} \times 10^3$	$\ln(\beta/Tp_1^2)$	2 nd Peak $T_{p_2}^\circ K$	$\frac{1}{Tp_2} \times 10^3$	$\ln(\beta/Tp_2^2)$
10	13.41	811.16	1.233	-10.8	943.16	1.060	-11.10
20	26.89	841.66	1.188	-10.18	954.16	1.048	-10.43
30	40.24	843.56	1.181	-9.76	953.16	1.045	-10.03
40	53.66	852.46	1.173	-9.51	968.66	1.032	-9.77
50	67.07	856.16	1.132	-9.30	972.16	1.029	-9.55

The activation energy of $T_{x_1}[\alpha-Fe(Si)]$ and $T_{x_2}[Fe_2B]$ phases has been calculated from table 4.5 and using Kissinger's plot shown in figure 4.7(a) and figure 4.7(b). It shows that first thermal crystallization activation energy of $\alpha-Fe(Si)$ phase E_1 is 2.52 eV and second Fe_2B phase E_2 is 4.06 eV.

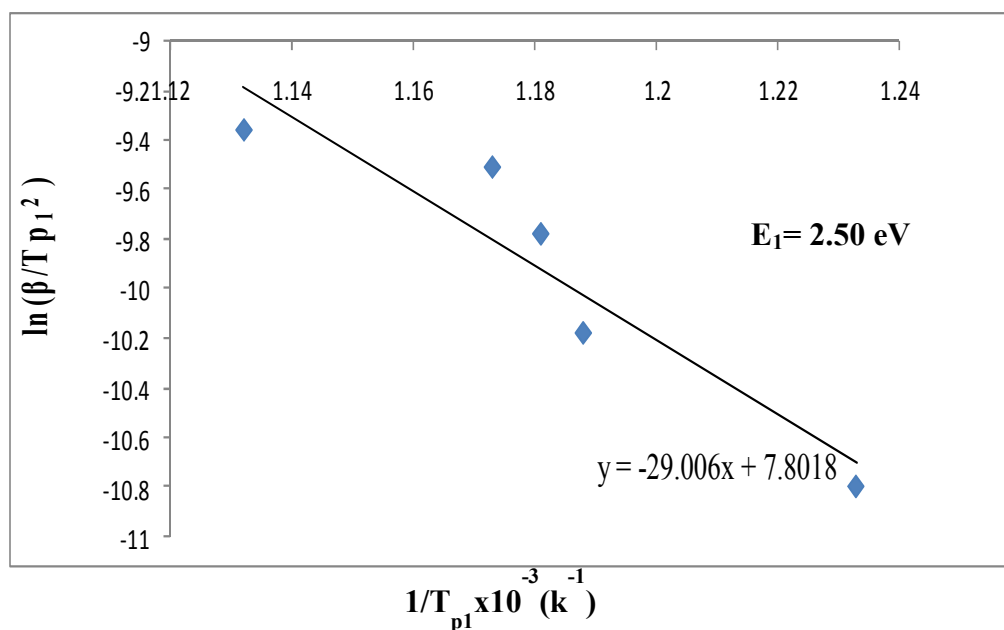


Figure 4.7(a) Kissinger's plot to determine the activation energy of $\alpha-Fe(Si)$ phase for $Fe_{73.5}Au_1Nb_3Si_{13.5}B_9$ alloy

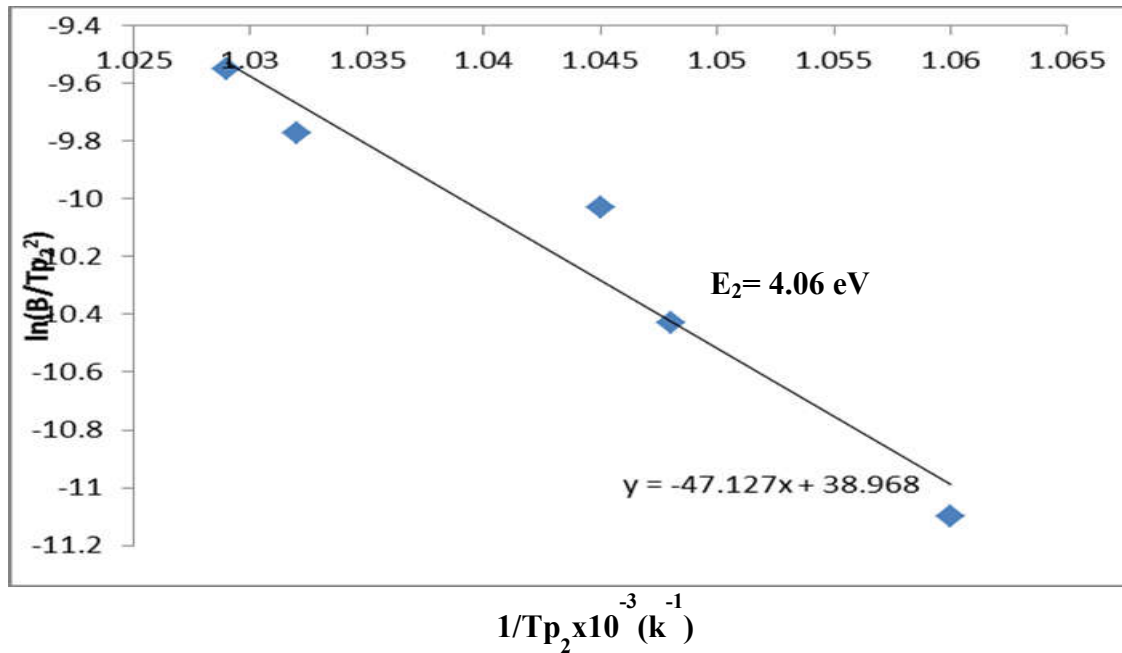


Figure 4.7(b) Kissinger's plot to determine the activation energy of Fe₂B phase for Fe_{73.5}Au₁Nb₃Si_{13.5}B₉ alloy

4.2.3 DTA Results of Nanocrystalline Amorphous Ribbons with Composition Fe_{73.5}Ag₁Nb₃Si_{13.5}B₉

DTA traces of as-cast nanocrystalline amorphous ribbon Fe_{73.5}Ag₁Nb₃Si_{13.5}B₉ alloy taken in the Nitrogen atmosphere with the heating rates of 10°C - 50°C/minute at the step of 10°C with continuous heating from room temperature to 800°C, are presented in Figure 4.8(a) to figure 4.8(e) respectively. Two well defined exothermic peaks typical for two steps of crystallization processes are manifested from the DTA traces. The first one corresponds to the crystallization of α-Fe(Si) phase and the second one is related to the crystallization of Fe₂B. The onset of crystallization temperatures T_{x1} and T_{x2} have been estimated from DTA traces.

From Figure 4.9 represents a combination of all DTA traces of amorphous Fe_{73.5}Ag₁Nb₃Si_{13.5}B₉ ribbon alloy. It is observed that the crystallization of each phase has occurred over a wide range temperature and that the peak temperatures shift to higher values with the increase of heating rate. That means it requires more that energy for the formation of crystalline phases with increasing heating rates. Table 4.6

crystallization peak temperatures of two phases (T_{p1} and T_{p2}) and crystallization starting temperatures of two phases (T_{x1} and T_{x2}) are given for different heating rates.

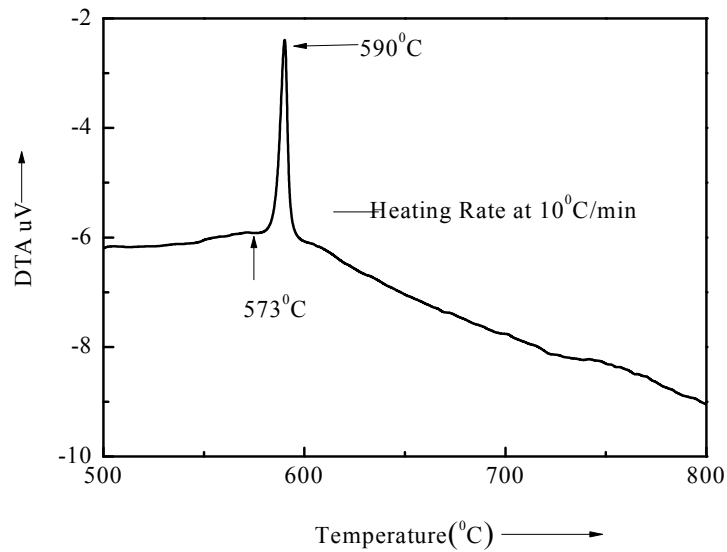


Figure 4.8(a) DTA trace of as-cast nanocrystalline amorphous ribbon $Fe_{73.5}Ag_1Nb_3Si_{13.5}B_9$ at the heating rate of $10^\circ C / min$

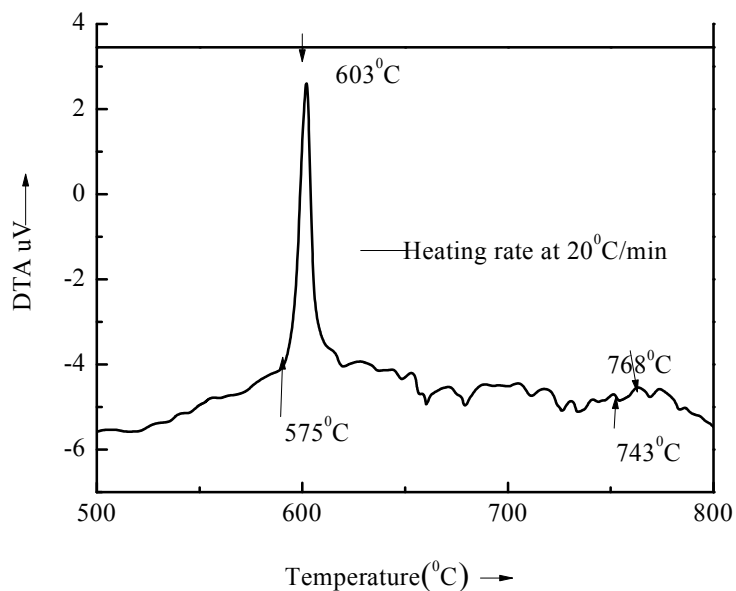


Figure 4.8(b) DTA trace of as-cast nanocrystalline amorphous ribbon $Fe_{73.5}Ag_1Nb_3Si_{13.5}B_9$ at the heating rate of $20^\circ C / min$

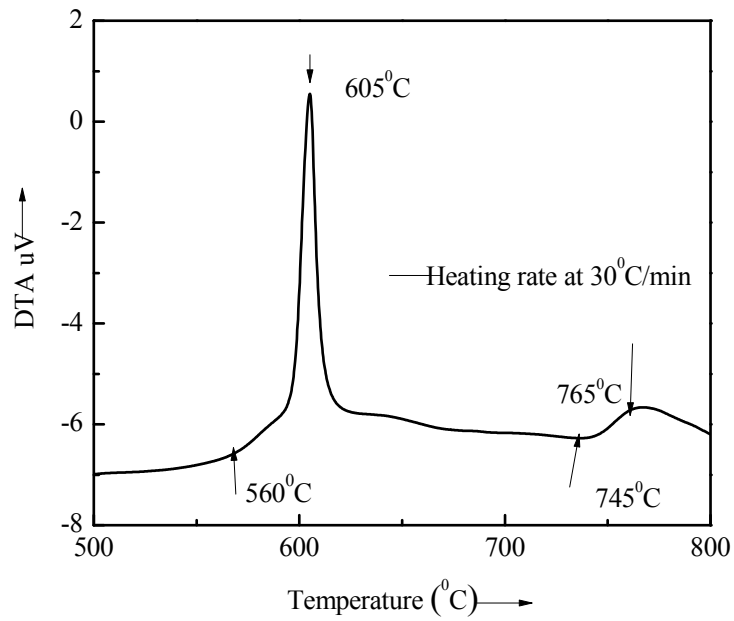


Figure 4.8(c) DTA trace of as-cast nanocrystalline amorphous ribbon $\text{Fe}_{73.5}\text{Ag}_1\text{Nb}_3\text{Si}_{13.5}\text{B}_9$ at the heating rate of $30^\circ\text{C}/\text{min}$

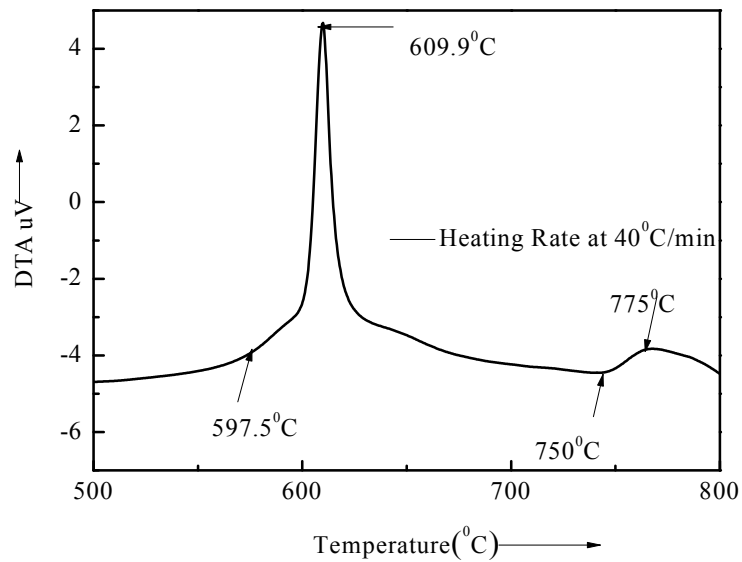


Figure 4.8(d) DTA trace of as-cast nanocrystalline amorphous ribbon $\text{Fe}_{73.5}\text{Ag}_1\text{Nb}_3\text{Si}_{13.5}\text{B}_9$ at the heating rate of $40^\circ\text{C}/\text{min}$

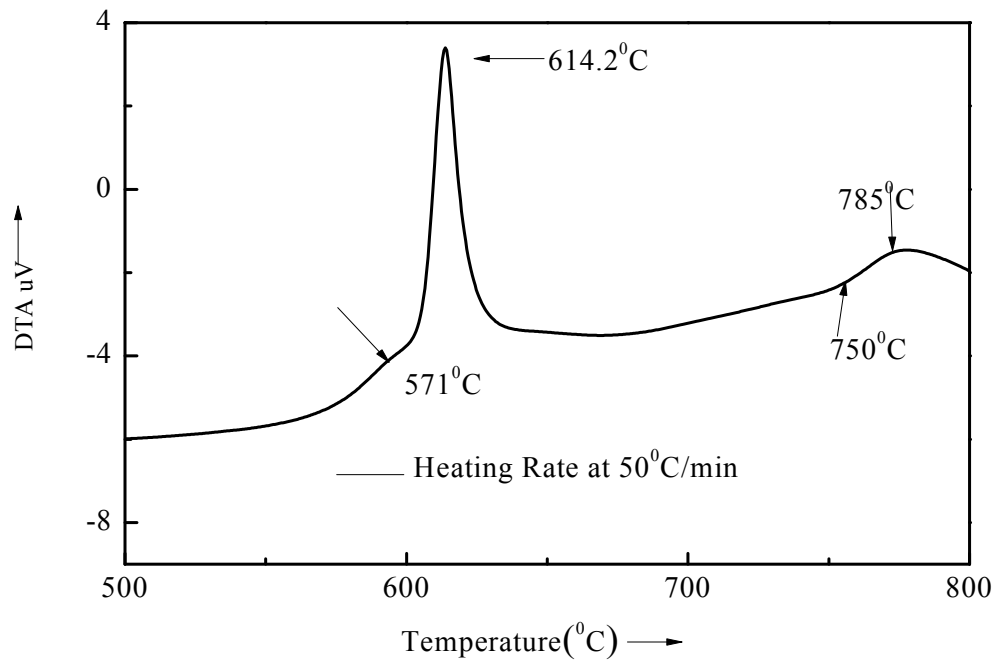


Figure 4.8(e) DTA trace of as-cast nanocrystalline amorphous ribbon $\text{Fe}_{73.5}\text{Ag}_1\text{Nb}_3\text{Si}_{13.5}\text{B}_9$ at the heating rate of $50^\circ\text{C}/\text{min}$

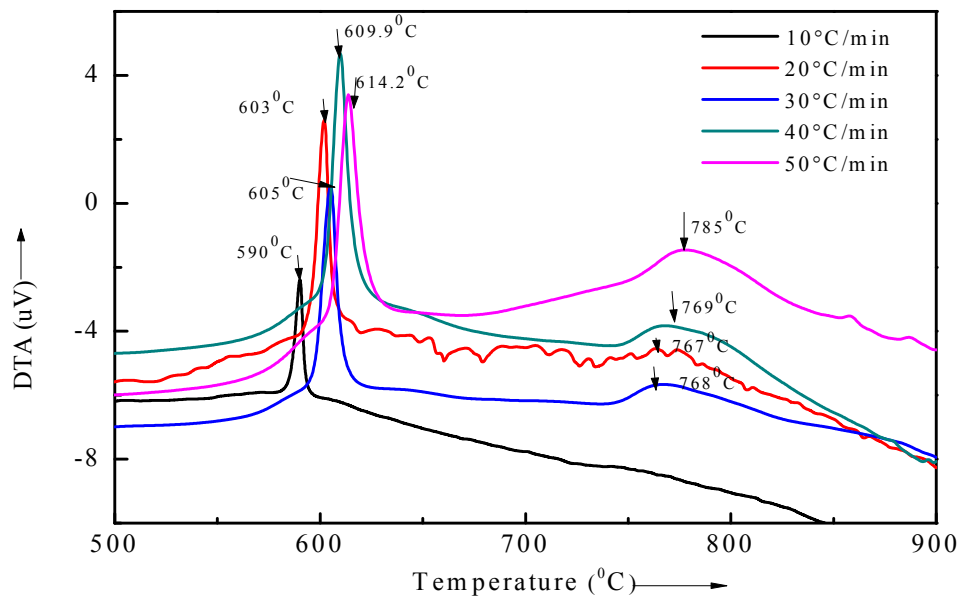


Figure 4.9 Effects of heating rate on DTA traces of nanocrystalline amorphous ribbon with composition $\text{Fe}_{73.5}\text{Ag}_1\text{Nb}_3\text{Si}_{13.5}\text{B}_9$ at the heating rate of 10°C to $50^\circ\text{C}/\text{min}$

Table 4.6 Effect of heating rate on 1st and 2nd crystallization states of the nanocrystalline amorphous ribbon with composition Fe_{73.5}Ag₁Nb₃Si_{13.5}B₉

Heating rate β °C/min	1 st starting T_{x_1} °C	1 st Peak T_{p_1} °C	Temperature range of 1 st state in °C	2 nd starting T_{x_2} °C	2 nd Peak T_{p_2} °C	Temperature range of 2 nd state in °C	T_{x_2} - T_{x_1} In °C	T_{p_2} - T_{p_1} In °C
10	573	590	17	----	----	----	----	----
20	575	603	28	743	768	25	168	165
30	560	605	45	745	767	22	185	162
40	597.5	609.9	12.4	750	769	19	152.2	159.1
50	571	614.2	43.2	750	785	35	179	170.8

It has been observed that the crystallization temperature range of first phase occurred within 12.4°C to 45°C. But this range for second crystallization phase is 19°C to 35°C. So it is notable that the crystallization temperature range for first peak is always larger than the second peak but except heating rate 40°C/minute; i.e. is experimental error. It is also observed that the peak temperature shifts to higher values and the crystallization temperature range increases with the increase of heating rates.

Table 4.7 Effect of heating rate on 1st and 2nd crystallization of the nanocrystalline amorphous ribbon with composition Fe_{73.5}Ag₁Nb₃Si_{13.5}B₉ for activation energy calculation data

Heating rate β °C/min	Heating rate β °K/min	1 st Peak T_{p_1} °K	$\frac{1}{T_{p_1}} \times 10^3$	$\ln(\beta/T_{p_1})$	2 nd Peak T_{p_2} °K	$\frac{1}{T_{p_2}} \times 10^3$	$\ln(\beta/T_{p_2})$
10	13.41	863.16	1.159	-10.93	----	----	-----
20	26.89	876.16	1.141	-10.26	1041.16	0.96	-10.60
30	40.24	878.16	1.139	-9.86	1040.16	0.961	-10.20
40	53.66	882.16	1.134	-9.58	1042.16	0.959	-9.92
50	67.07	887.36	1.127	-9.37	1048.16	0.954	-9.70

The activation energy of T_{x_1} [α -Fe (Si)] and T_{x_2} [Fe₂B] phases have been calculated from Table 4.7 and using Kissinger's plot shown in figure 4.10(a) and

figure 4.10(b). It shows that first thermal crystallization activation energy of α -Fe(Si) phase E_1 is 4.37 eV and second Fe₂B phase E_2 is 4.45 eV.

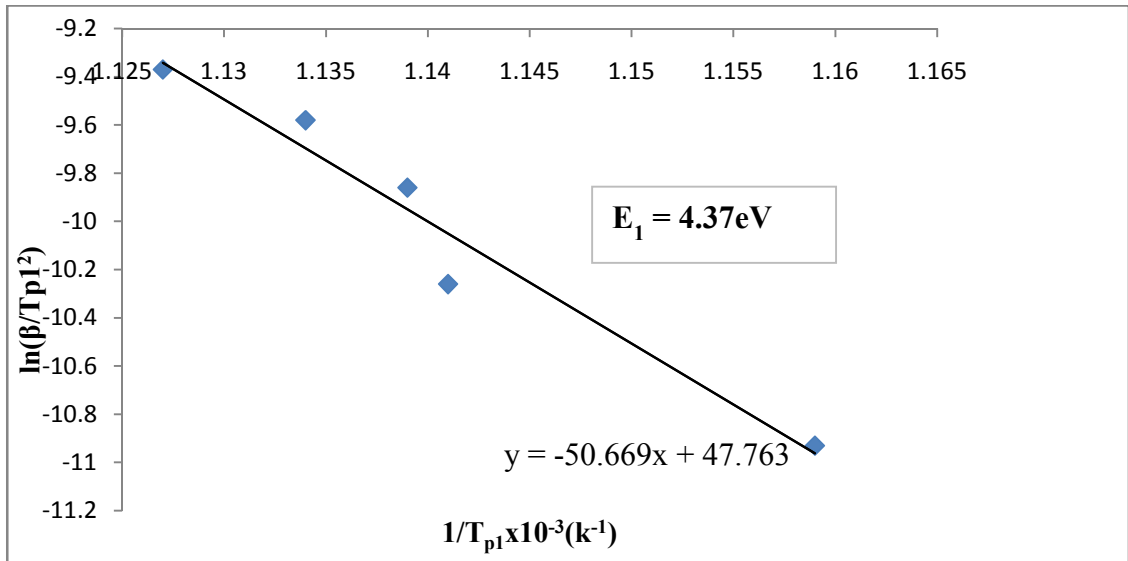


Figure 4.10(a) Kissinger's plot to determine the activation energy of Fe(Si) phase for Fe_{73.5}Ag₁Nb₃Si_{13.5}B₉ alloy

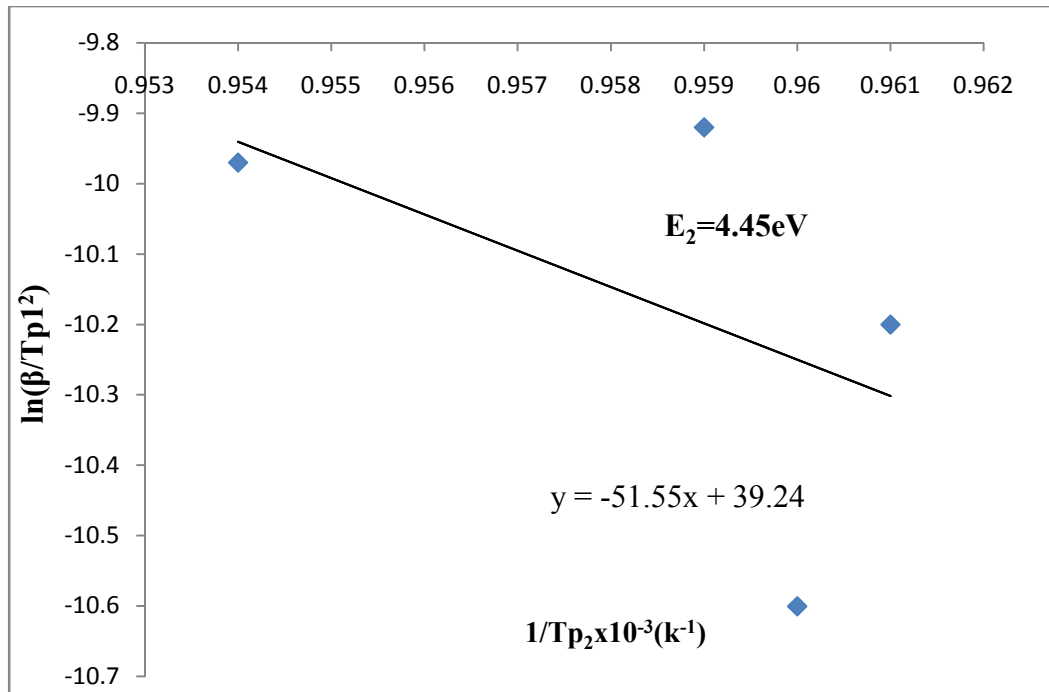


Figure 4.10(b) Kissinger's plot to determine the activation energy of Fe₂B phase for Fe_{73.5}Ag₁Nb₃Si_{13.5}B₉ alloy

4.3 Comparison between DTA of Fe-X-Nb-Si-B [X = Cu, Au & Ag]

From the DTA study it is well accepted that the crystallization characteristics of amorphous nanocrystalline alloys are strongly dependent on heating rate, temperature and also the alloy compositions. The 1st starting and peak crystallization temperature for the three samples are different. The order of the three sample with respect to their crystallization temperature range and peak temperature can be arranged



And 2nd crystallization peak temperature can be arranged

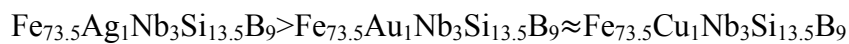


Table 4.8 crystallization states (heating rate 20^oC/min) and activation energy of different phases of nanocrystalline amorphous ribbons with composition $\text{Fe}_{73.5}\text{X}_1\text{Nb}_3\text{Si}_{13.5}\text{B}_9$ [X = Cu, Au & Ag]

X-content	1 st starting T_{x_1} °C	1 st Peak T_{p_1} °C	2 nd starting T_{x_2} °C	2 nd Peak T_{p_2} °C	Activation energy of Fe (Si) phase E_1 in eV	Activation energy of Fe_2B phase E_1 in eV
X = Cu	513	543	663	689	2.18	3.62
X= Au	522.4	568.5	662.7	681	2.52	4.06
X = Ag	575	603	743	768	4.37	4.45

From all the DTA curve it is observed that 1st peak is greater than 2nd one. It is evident that the 1st peak associated always with the primary crystallization becomes more prominent than the 2nd one, with the increase of heating rate something that has already been observed through DSC measure that [4.12]. In Table 4.8 the experimental value of DTA parameters of three samples are given. Activation energy of the 1st crystallization phase of all the samples are shown in the range 2.18eV – 4.37eV. But for the present the sample FINEMET value 2.18eV which higher than the above range in Cu replacement with Au or Ag. The nature of the 2nd crystallization phase is also maintains this order. The composition of the alloy affects both the primary and secondary crystallization process, because the time needed for the constituent atom to have long range order depends on their bond energies [4.13-4.14].

The formation of nucleation centers and their growth need to be inhibited to avoid crystallization on the stability of the crystalline amorphous state is thus studied keeping the heating rate constant. It should be stresses that good soft magnetic properties require not only good soft magnetic properties require but all so a small grain size but at the sometime the absence of boron compounds.

The amorphous state maintain amorphousity against annealing temperature is said to be stable i.e. a sample with higher crystallization temperature is said to be stable. From this stability condition the stability of these three samples can be expressed



The primary crystallization temperature T_{x_1} represents the upper limit of use for an amorphous material. For synthesis of a nanocrystalline material this is the useful crystallization event. In the amorphous precursor route to producing nanocrystalline materials secondary crystallization is typically of a terminal boride phase. These Fe_2B phase is typically deleterious in that it lowers magnetic permeability by domain wall pinning. The secondary crystallization temperature T_{x_2} represents the upper limit of use for nanocrystalline materials. All these activation energies are two crystallization phases of the samples are represent such as the observation of nanocrystallization products.

4.4 Microstructural Analysis of Amorphous and Nanocrystalline Fe-X- Nb-Si-B [X = Cu, Au & Ag] Alloy by XRD Analysis

A key tool in both the routine characterization and the in depth study of nanocrystalline materials has been X-ray diffraction techniques. From the melt spinning process, an amorphous alloy with tiny copper clustering is produced. In the early stages of annealing at an optimum temperature, new Cu-rich as well as replacement Au or Ag clusters are formed, the growth of existing Cu or Au or Ag clusters. The concept of heterogeneous nucleation $\alpha\text{-Fe}(\text{Si})$ on the Cu or Au or Ag-rich cluster is based on the minimization of the interfacial energy. Finally the growth of $\alpha\text{-Fe}(\text{Si})$ grain used as nucleation sites grow the larger sizes $> 5\text{nm}$. Nanocrystalline alloys above crystalline and because crystallinity they exhibit Bragg scattering peaks in XRD experiments. In the present work of three experimental nanocrystalline

amorphous alloy ribbon were prepared by rapid quenching technique and the amorphous state was confirmed by XRD. However, the appearance of the best properties is sensitive to the alloys annealing temperature.

In the present work, in order to study the crystallization onset temperature, XRD spectra have been recorded for the nominal composition $Fe_{73.5}X_1Nb_3Si_{13.5}B_9$ [$X = Cu, Au \& Ag$] annealed at 450° to 800° for 30 minutes. The approximately annealed samples were subjected to XRD by using a MTI Corporation built GSL-1600X40 tube furnace to examine the micro structural evaluation as a function of annealing temperature. From the experiment, three samples are annealed at different temperature for 30 minute and every sample was taken under XRD analysis. From the output of XRD analysis three structural parameters such as:

- (i) Lattice Parameter (a_o)
- (ii) Grain Size (D_g)
- (iii) Silicon Content (Si)

(i) Lattice Parameter Calculation

Lattice Parameter of crystalline α -Fe(Si) nanograin was determined at different annealing temperature of the experimental alloys. Structure of the α -Fe(Si) grains depends on the annealing temperature. Normally lattice Parameter of an alloy composition is determined by the Debye-Scherrer method after extrapolation of the diffraction curve for the sample. Generally for an accurate determination of the lattice parameter a number of fundamental peaks are required but in this type of tailored materials upon crystallization only major fundamental peaks (110) is used in calculation of a_o . Determined the lattice parameter using only that particular reflection using equation:

$$2d \sin\theta = n\lambda \text{ and } a_o = d\sqrt{2} \tag{4.2}$$

Where $\lambda = 1.54053 \text{ \AA}$ is the wavelength of Cu- K_α radiation and a_o is determined lattice parameter of the grain, d is the inter-planar spacing and θ is the diffraction angle.

(ii) Grain Size Determination

One of the most important aim of this study was to determine crystalline grain size for all the annealing temperatures. When these nanometric grains are consolidated to form a nanostructured material, the magnetic properties are largely determined by the grain size and the exchange interaction between the adjacent grains. Herzer [4.15] successfully established the theoretical explanation on the grain size dependence of superior soft magnetic properties based on his Random Anisotropy Model (RAM) after the pioneer experimental invention of FINEMET alloy by Yoshizawa *et al.* [4.16].

Grain size was determined from XRD pattern of (110) reflection for different annealing temperature at constant annealing time 30 minutes from which grain size was determined using the formula

$$D_g = \frac{0.9 \lambda}{\beta \cos \theta} \quad (4.3)$$

Where $\lambda = 1.54178 \text{ \AA}$ is the wavelength of $Cu-K_\alpha$ radiation, θ is the diffraction angle and β is the full width at half maximum (FWHM) of diffraction peak in radian for different steps of annealing temperature.

(iii) Si Content in Nanograins

The major elements of the amorphous ribbon were Fe and Si with concentration of 73.5at.%Fe and 13.5 at.% Si. Crystalline nanograins were formed on the ribbon in the process of annealing temperature with the alloy composition of Fe-Si. It is therefore important to determine the concentration of Fe and Si and we have experimentally determined the lattice parameter of the alloy nanograins for the compositions of different annealing temperatures. It is easy to calculate the Si content in the nanograin from the Pearson hand book relationship [4.17]. From this relationship we have considered a simple equation to calculate Si-content from lattice parameter. This equation is

$$b = -467a_0 + 1342.8 \quad (4.4)$$

where b is at. % Si in the nanograins, a_0 is the lattice parameter of nanograins.

4.4.1 XRD Analysis of the Nanocrystalline Ribbon with Composition $\text{Fe}_{73.5}\text{Cu}_1\text{Nb}_3\text{Si}_{13.5}\text{B}_9$

In the present work, structure of the $\text{Fe}_{73.5}\text{Cu}_1\text{Nb}_3\text{Si}_{13.5}\text{B}_9$ nanocrystalline ribbon alloys annealed at temperature (T_a) from 450°C to 800°C for annealing time 30 minutes are investigated by the XRD method are presented in figure 4.11. In the figure 4.11, the indices of the reflecting planes are shown in the parenthesis XRD results indicate that no α -Fe(Si) phases are present in the alloys annealed below 600°C for 30 minutes. When the alloys were annealed at or above 600°C, crystalline phase is developed on the amorphous ribbon. Patterns of $T_a = 600^\circ\text{C}$ indicates a clear α -Fe(Si) phase of said composition after heat treatment for 30 minutes. The same pattern observed for all the samples at different annealing temperature indicating the α -Fe(Si) phase. The intensity of the diffracted peak of α -Fe(Si) phase in the alloy is increased with the increase of annealing temperature. For an annealing at higher temperature i.e. 600°C, 650°C, 700°C, 750°C and 800°C, α -Fe(Si) phase were found at lower values of 2θ at.% 44.96°, 44.76°, 45.75°, 45.5° and 44.84° respectively with 100% peak intensity on (110) line. All the results of θ , d-values, FWHM from XRD analysis are listed in Table 4.9.

Figure 4.12 shows the variation of lattice parameter and Si-content α -Fe(Si) phase with respect to the annealing temperature of the samples. For the annealing temperature 600°C an increase of lattice parameter and attains the minimum value at 700°C. The lattice parameter of α -Fe(Si) phase is always smaller than that of pure Fe, the value of which is 2.8664Å [4.18]. The systematic but negligible shift of the peak forwards the larger angles with increasing temperature indicates that lattice parameter of the phase gradually decreases due to the increase of Si-content of the α -Fe(Si) phase. Both the decrease in lattice parameter and increase in intensity of the fundamental peak with increasing annealing temperature suggest that Si-atom diffuse most intensity into the bcc α -Fe with increase of annealing temperature. The diffusion of Si increases in bcc α -Fe with annealing temperature. Percentage of Si is the controlling parameter of structural change for nanocrystalline alloy. Percentage of Si in the α -Fe(Si) phase has can point of saturation i.e. maximum value. For this sample it is about 12.36% and obtained at 600°C. Above or below this critical annealing

temperature %Si decreases i.e. lattice parameter increases So Si-content and lattice parameter is closely related which is expressed in Pearson Hand book relationship [4.17].

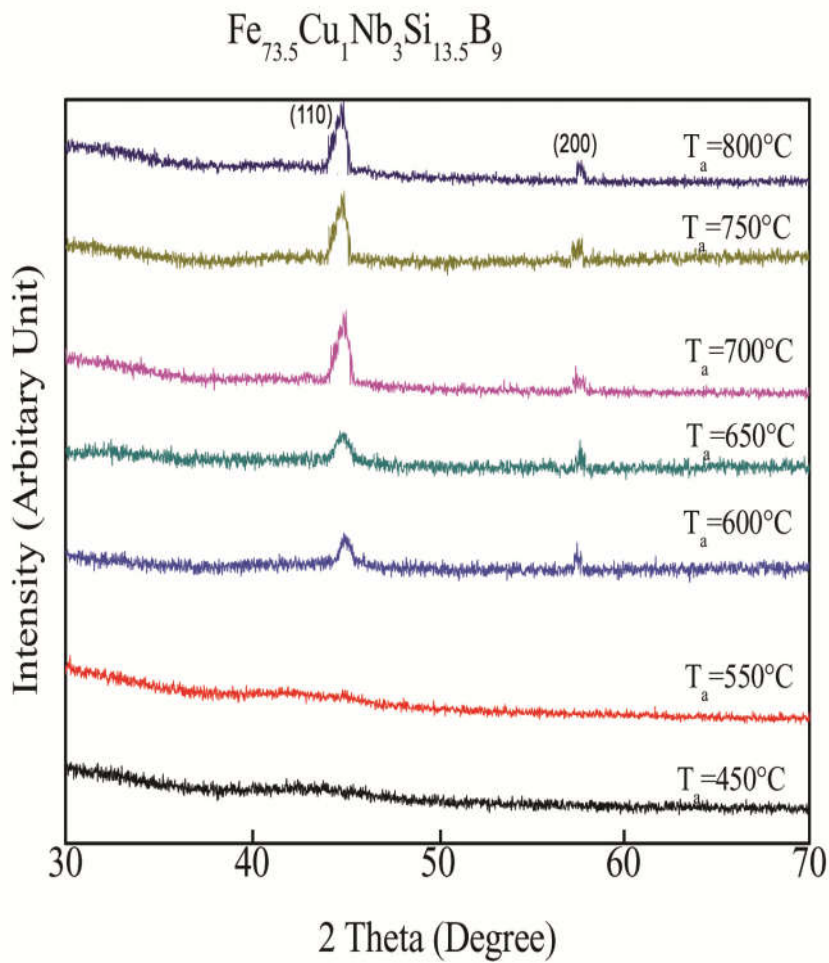


Figure 4.11 XRD spectra of $\text{Fe}_{73.5}\text{Cu}_1\text{Nb}_3\text{Si}_{13.5}\text{B}_9$ alloys of annealed at different temperatures at constant annealing time 30 minute

Table 4.9 Experimental XRD data of nanocrystalline $\text{Fe}_{73.5}\text{Cu}_1\text{Nb}_3\text{Si}_{13.5}\text{B}_9$ for different annealing temperature

Annealing Temp. in $^{\circ}\text{C}$	θ (deg.)	d (\AA)	FWHM (deg.)	a_0 (\AA)	D_g (nm)	Si (at %)
450	--	--	--	--	--	--
550	----	----	----	----	---	----
600	22.48	2.014	0.60	2.8489	14	12.36
650	22.38	2.0232	0.48	2.8613	18	6.57
700	22.87	1.9819	0.43	2.8028	19	10.80
750	22.25	2.0342	0.40	2.877	20	11.28
800	22.42	2.0196	0.39	2.8561	20	12.4

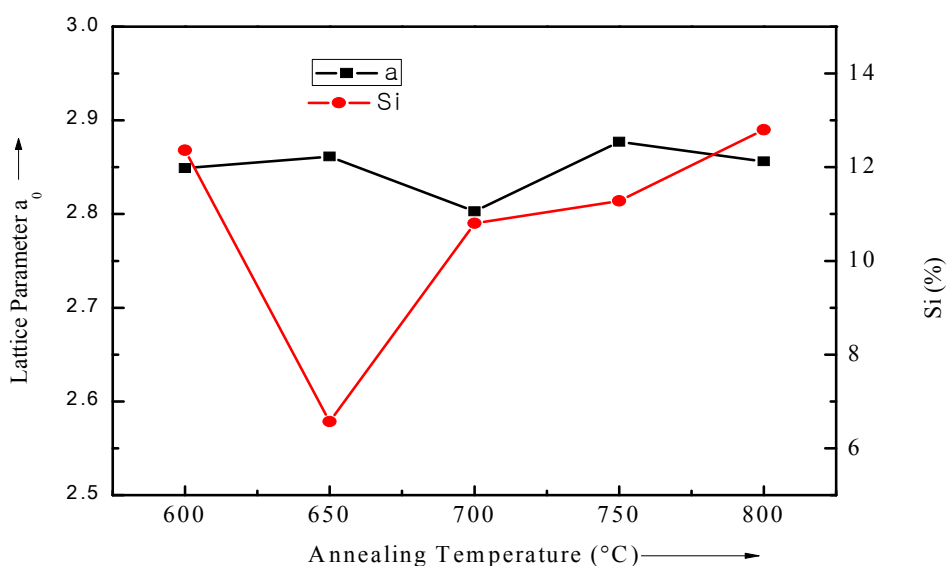


Figure 4.12 Change of Si (at. %) content and Lattice Parameter with different annealing temperature for the sample with composition $\text{Fe}_{73.5}\text{Cu}_1\text{Nb}_3\text{Si}_{13.5}\text{B}_9$

Instrumental broadening of the system was determined from $\theta - 2\theta$ scan of standard Si. At the position of (110) reflections, the value of instrumental broadening was found to be 0.07°C . The value instrumental broadening of the peak due to stacking fault of bcc crystal was corrected negligible in the present case. In figure 4.11 it is clear that the low annealing temperature 600°C , the FWHM of the peak is large and with the increases of annealing temperature, the values of FWHM are

getting smaller. All the values of grain size for every step of annealing temperature of the composition were determined and the values are listed in Table 4.9.

This fact indicates that at 600°C the grain size is smaller in size, 14nm and with increase of annealing temperature grain size is getting bigger in size the range of 18 to 20nm. Figure 4.13 shows that grain size increases with annealing temperature. The increase of annealing temperature initiates partitioning of Si in α -Fe phase and thus grain growth due to formation of nanocrystalline α -Fe(Si) grains. The formation of nanometric microstructure corresponding to the grain growth with increase of annealing temperature is ascribed to combined effects of Cu and Nb and their low solubility in Fe. Cu which is insoluble in α -Fe(Si), segregates prior to at the very beginning of nanocrystalline forming Cu-rich clusters and the nucleation of Fe(Si) grain in through to be multiplied by clustering of Cu which stands as the reason for the grain growth at the initial stage of crystallization. In the XRD method much larger area is subjected for investigation consequently, problems of statistical significance might arise since a small number of large grains might cause an overestimation of grain size.

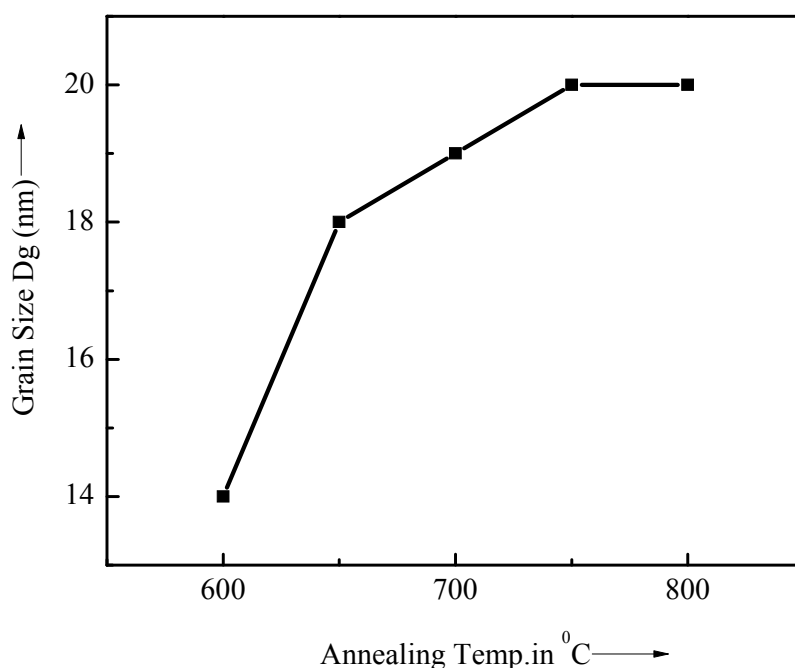


Figure 4.13 Change of Grain Size with different annealing temperature for the sample with composition $\text{Fe}_{73.5}\text{Cu}_1\text{Nb}_3\text{Si}_{13.5}\text{B}_9$

As mentioned earlier in the simple Scherrer formula, the width of a given reflection is used for grain size determination which underestimates the grain size as the strains evidently present in the nanostructure are not affect into account. Grain size, phase transition and transition temperatures were observed to depend on the Cu/Nb content. The magnetic properties are strongly correlated to the microstructural features.

4.4.2 XRD Analysis of the Nanocrystalline Ribbon with Composition

$\text{Fe}_{73.5}\text{Au}_1\text{Nb}_3\text{Si}_{13.5}\text{B}_9$

Figure 4.14 shows typical XRD patterns of bcc α -Fe(Si) phase for the sample of composition $\text{Fe}_{73.5}\text{Au}_1\text{Nb}_3\text{Si}_{13.5}\text{B}_9$ after heat treatment 30 minutes at different temperature. From 450°C to 800°C pattern of annealing temperature (T_a) 450°C to 600°C indicates the amorphous nature. After heat treatment at $T_a = 650^\circ\text{C}$ initiation of crystallization takes place. The same patterns were observed for all samples at different annealing temperature indicating the α -Fe(Si) phase are developed on amorphous ribbon after heat treatment. Moreover, the α -Fe phase is unique crystalline of the alloys annealed at 650°C to 800°C, the variation of intensity of the diffraction lines in patterns obtained under the same condition, reveals that the peak of α -Fe phase in the alloys is increased with increase of the annealing temperature of crystalline nanograin of α -Fe (Si) phase. All the results of θ , d-value, FWHM, a_0 , D_g and at.% Si at different annealing temperature of these composition are listed in Table 4.10.

In figure 4.15 the lattice parameter of α -Fe(Si) grains embedded in the amorphous matrix of various annealed samples in the temperature range between 650°C to 800°C has been performed, with the increase of annealing temperature lattice parameter slightly decreases. These results agree with the lattice parameter of α -Fe(Si) phase is always smaller than that of pure Fe. The Si-content of the alloy $\text{Fe}_{73.5}\text{Au}_1\text{Nb}_3\text{Si}_{13.5}\text{B}_9$ at 650°C to 800°C at constant annealing time 30 minutes are found to be in the range of 9.01% to 12.36%. All these results are presented in Table 4.10 and the pattern of change in Si content with respect to annealing temperature are presented in figure 4.15. Above or below this critical annealing temperature at.% Si decreases as lattice parameter increases.

In figure 4.16 the mean grain size of the nanograins determined from the X-ray fundamental line (110) using the Scherrer formula are presented. The increasing of annealing temperature initiates partitioning of Si in the α -Fe(Si) phase. In the range of annealing temperature 650°C to 800°C, the grain size remains in the range 13 - 25nm. These facts reveal that heat treatment temperature should be limited with 650°C to 700°C to obtained soft magnetic behavior which will be clear that nearly constant grain size.

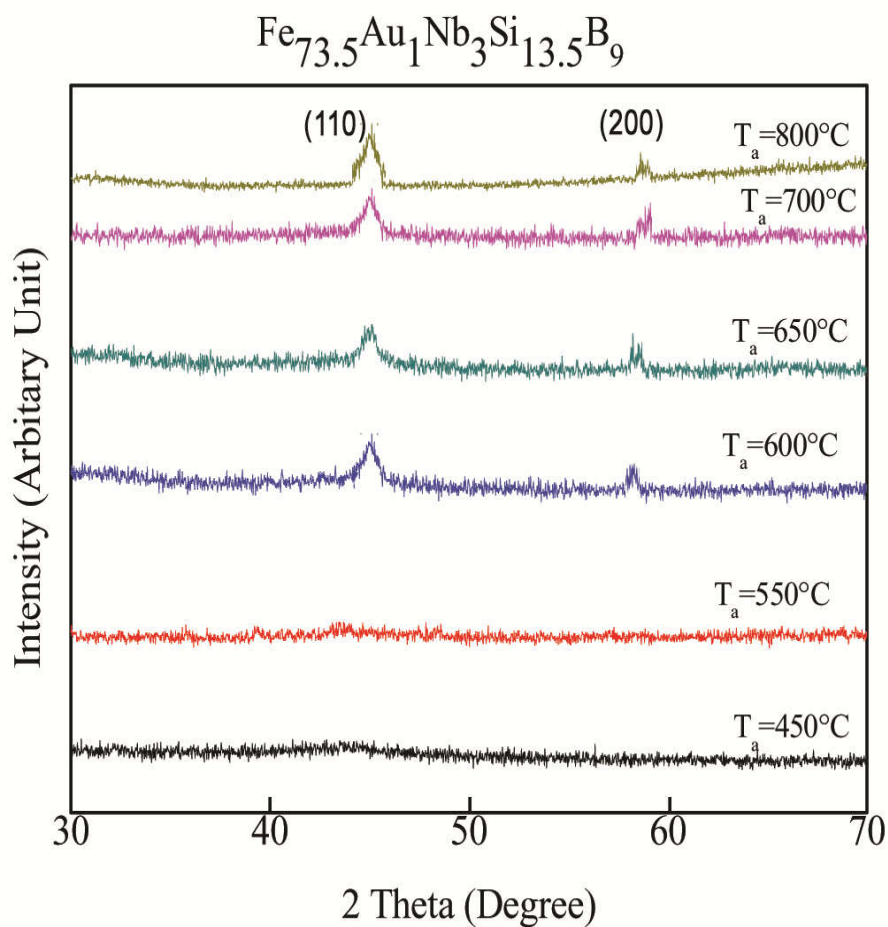


Figure4.14 XRD spectra of $\text{Fe}_{73.5}\text{Au}_1\text{Nb}_3\text{Si}_{13.5}\text{B}_9$ alloys of annealed at different temperature at constant annealing time 30 min

Table 4.10 Experimental XRD data of nanocrystalline $\text{Fe}_{73.5}\text{Au}_1\text{Nb}_3\text{Si}_{13.5}\text{B}_9$ amorphous ribbon at different annealing temperatures

Annealed temperature	Diffracted angel	d(A)	FWHM	Lattice parameter	Grain size	Si(%)
450	-	-	-	-	-	-
550	-	-	-	-	-	-
600	22.48	2.0145	0.65	2.8489	13	12.36
650	22.46	2.0176	0.40	2.8533	21	10.30
700	22.44	2.0195	0.44	2.8560	20	09.01
800	22.45	2.0169	0.325	2.8523	25	10.78

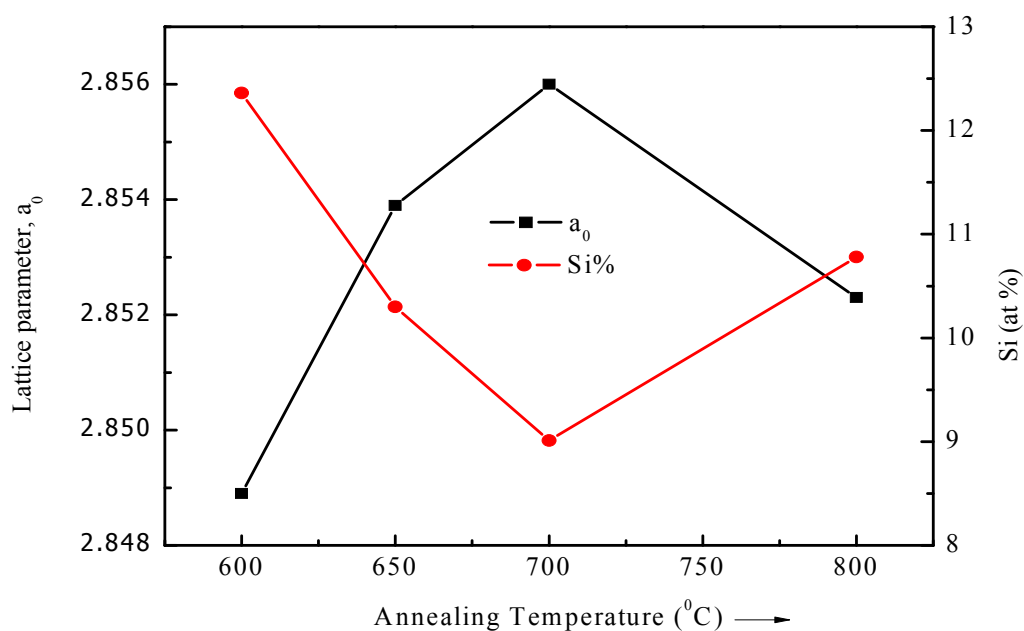


Figure 4.15 Change of Si (at %) content and Lattice Parameter with different annealing temperature for the sample with composition $\text{Fe}_{73.5}\text{Au}_1\text{Nb}_3\text{Si}_{13.5}\text{B}_9$

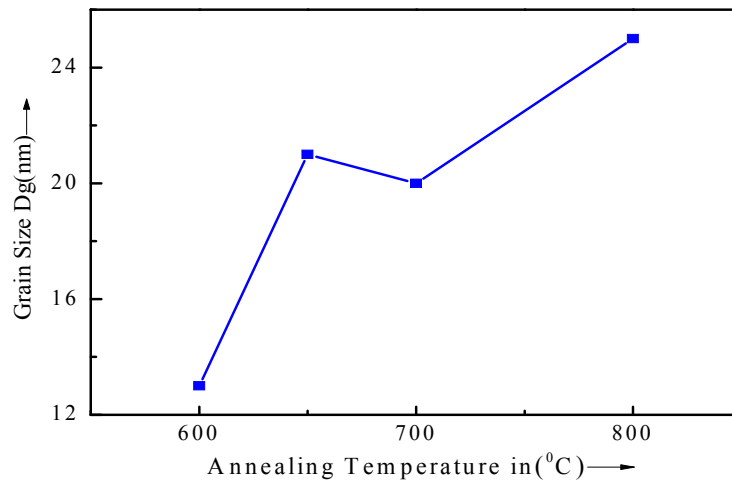


Figure 4.16 Change of Grain Size with different annealing temperature for the sample with composition $\text{Fe}_{73.5}\text{Ag}_1\text{Nb}_3\text{Si}_{13.5}\text{B}_9$

4.4.3 XRD Analysis of the Nanocrystalline Ribbon with Composition $\text{Fe}_{73.5}\text{Ag}_1\text{Nb}_3\text{Si}_{13.5}\text{B}_9$

In the present work, structure of the $\text{Fe}_{73.5}\text{Ag}_1\text{Nb}_3\text{Si}_{13.5}\text{B}_9$ alloys, annealed at temperature 450°C to 800°C , are investigated by the XRD shown in figure 4.17. From XRD patterns 450°C to 600°C indicates the amorphous nature. Due to annealing at 650°C , the first crystallization peak was found at the angle 45° . It means at the annealing temperature below 650°C no crystalline peak has been detected. After heat treatment at $T_a = 650^\circ\text{C}$ initiation of crystallization takes place. For annealing at higher temperature i.e. 650°C , 700°C , 750°C and 800°C , the $\alpha\text{-Fe}(\text{Si})$ phase were found at the lower values of 2θ at 45° , 44.84° , 44.852° , 44.88° and 44.66° respectively with 100% peak intensity on (110) line. The XRD pattern has taken for the samples annealed from 650°C to 800°C under the same condition. The intensity of the diffracted peak of $\alpha\text{-Fe}(\text{Si})$ phase in the alloy is increased with increase of annealing temperature.

All the results of θ , d-value, FWHM, a_0 , D_g and at.% Si at different annealing temperature of these composition are listed in Table 4.11. Figure 4.18 shows that, with increase in annealing temperature lattice parameter increase. Observed lattice parameter at various annealing temperature for the present alloy are significantly less

than that of pure Fe is 2.8664Å. From figure 4.18 it is observed that the Si-content in α -Fe(Si) phase decrease with annealing temperature up to 800°C and figure represents the inverse relationship between lattice parameter and silicon content.

It is notable that Si-contents in the nanocrystallites at different annealing temperatures are higher than Si-content of the amorphous phase diffuses into α -Fe space lattice during crystallization process to form α -Fe(Si) nanograins. This means that the crystallization of this alloy is a diffusion controlled process with temperature as controlling parameter. From figure 4.19 and Table 4.11 that grain size (D_g) constant up to 700°C and above this annealed temperature grain size increases. In the range of annealing temperature 650°C to 800°C, the grain size remains in the range of 9 to 30nm. Grain growth rapidly and attain value 20nm at 750°C indicating formation of boride phase. Grain size increases with annealing temperature from a value of $D_g = 30$ nm for $T_a = 800^\circ\text{C}$ while Si content rapidly decreases with T_a . This is contradictory to original FINEMET alloy. The real cause is not clear and remains still an open question. These facts reveal that heat treatment temperature should be limited with in 650°C to 700°C to obtain optimum soft magnetic behavior, which will be clear that constant grain size.

Table 4.11 Experimental XRD data of nanocrystalline $\text{Fe}_{73.5}\text{Ag}_1\text{Nb}_3\text{Si}_{13.5}\text{B}_9$ amorphous ribbon at different annealing temperatures

Annealing Temp. in °C	θ (deg.)	d (Å)	FWHM (deg.)	a_0 (Å)	D_g (nm)	Si (at. %)
450	--	--	--	--	--	--
550	--	--	--	--	--	--
600	--	--	--	--	--	--
650	22.50	2.013	0.82	2.8468	10	12.58
700	22.42	2.0196	0.87	2.8561	9	9.00
750	22.44	2.018	0.42	2.8538	20	10.00
800	22.33	2.027	0.28	2.8666	30	4.1

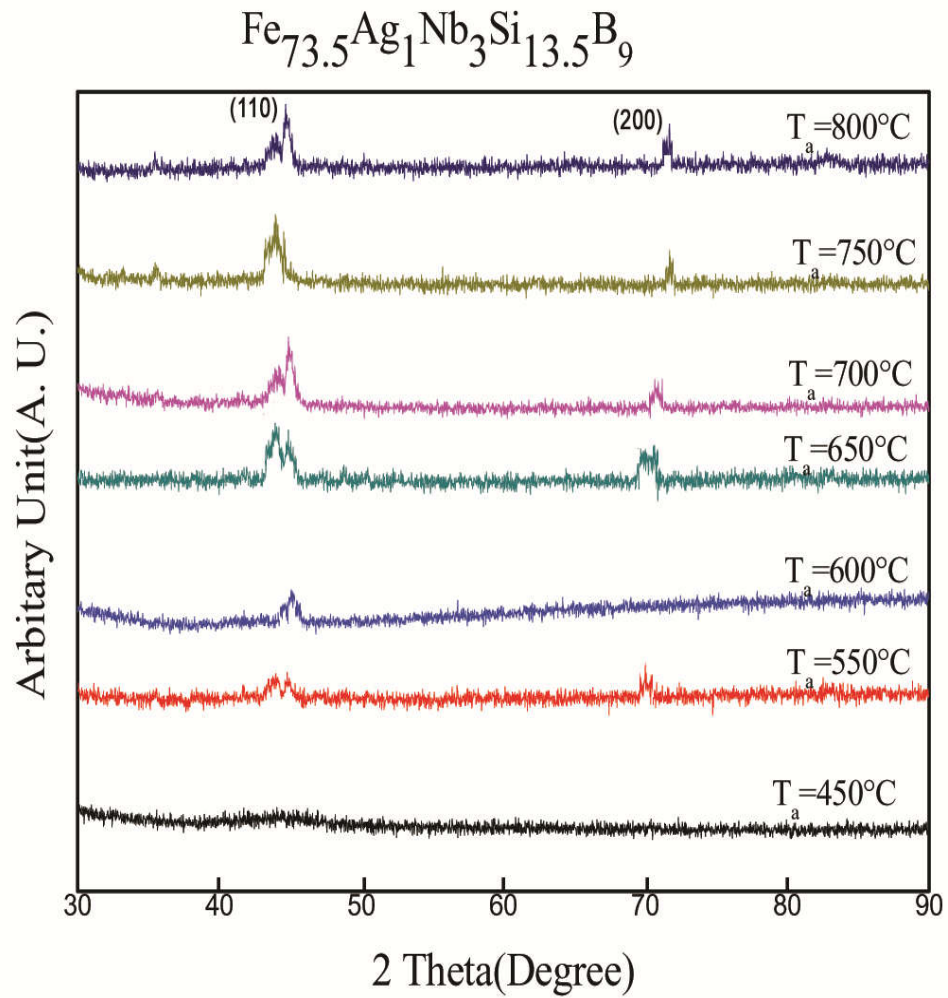


Figure4.17 XRD spectra of $\text{Fe}_{73.5}\text{Ag}_1\text{Nb}_3\text{Si}_{13.5}\text{B}_9$ alloys of annealed at different temperatures at constant annealing time 30 minutes

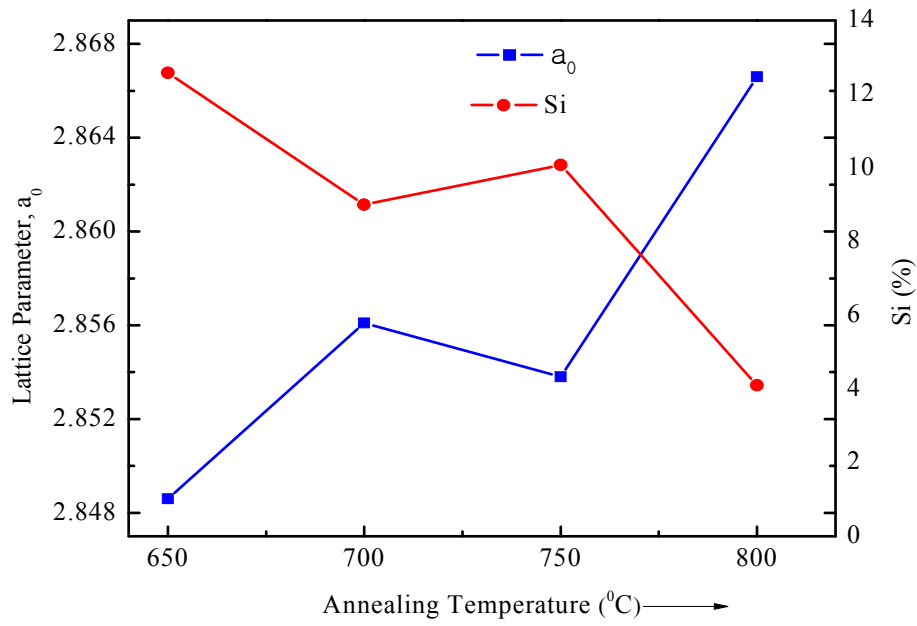


Figure4.18 Change of Si (at. %) content and Lattice Parameter with different annealing temperature for the sample with composition $\text{Fe}_{73.5}\text{Ag}_1\text{Nb}_3\text{Si}_{13.5}\text{B}_9$

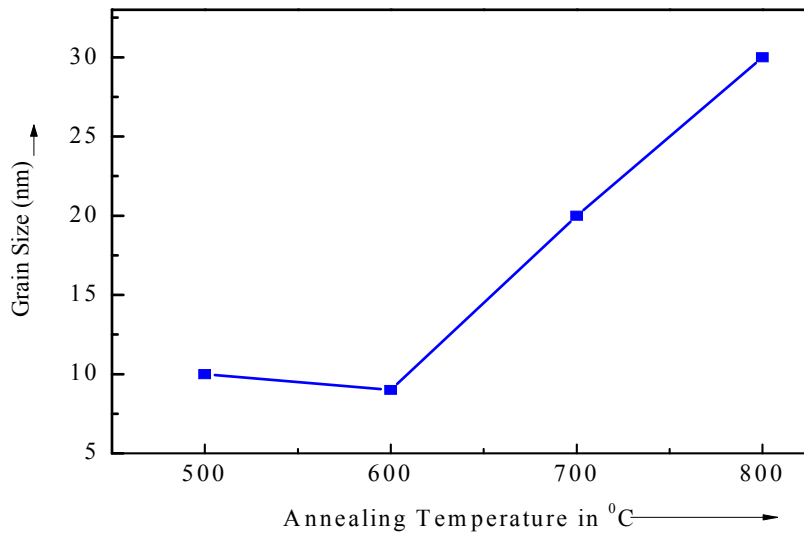


Figure4.19 Change of Grain Size with different annealing temperature for the sample with composition $\text{Fe}_{73.5}\text{Ag}_1\text{Nb}_3\text{Si}_{13.5}\text{B}_9$

4.5 Specific Magnetization Measurement of Fe-X- Nb-Si-B [X = Cu, Au & Ag] Nanocrystalline Amorphous Ribbons

The magnetization of these Fe-X-Nb-Si-B ribbons with composition $\text{Fe}_{73.5}\text{X}_1\text{Nb}_3\text{Si}_{13.5}\text{B}_9$ [X = Cu, Au & Ag] in as quenched condition is measured, using a vibrating sample magnetometer VSM [4.19]. The sample is measured as a function of magnetic field using a (V.S.M). The magnetometer was used as a field measuring device which was not affected by the presence of sample for its low susceptibility. In this type of magnetometer the sample is vibrated up and down in a region surrounded by several pick up coils. The magnetic sample is thus acting as a time changing magnetic flux, varying inside a particular region of fixed area. The lock-in-action of V.S.M. yields an accuracy of 0.05% of the full scale. Least measurable moment is $5 \times 10^{-4} \text{ emu}$. The proportionality constant accounting for the particular coil geometry and susceptibility is obtained by calibration with a high purity circular disk shaped Ni-sample. This sample has a saturation magnetization of about 54.75 emu/g with a saturation flux of about 20kOe at room temperature. A relative accuracy of about 1% is obtained with a double coils, the absolute accuracy depends on the calibration method. The ribbon samples were cut into small shapes, weighed and glued to a standard sample holder.

The magnetization process of the nanocrystalline amorphous ribbons with different field is shown in Figure 4.20 and Figure 4.21. Specific saturation magnetization (M_s) process for these ribbons has lower values for increasing replacement of Cu by Au or Ag. In contrast, magnetization measurement at room temperature is saturated with an applied field of 7kOe. It can be seen that maximum saturation is reach at 132.14emu/gm for $\text{Fe}_{73.5}\text{X}_1\text{Nb}_3\text{Si}_{13.5}\text{B}_9$ sample. Haranda *et. al* [4.20] have studied the approach to saturation in nanocrystalline FINEMET materials. The magnetization prior to saturation is associated with reversible rotation and has been fitted to the law

$$M(H) = M_s \left[1 - \frac{a_1}{H} - \frac{a_2}{H^2} \right] + bH^{1/2} \quad (4.5)$$

Where the term $\frac{a_2}{H^2}$ was described as being a direct consequence of the random anisotropy model, and attributable to α -Fe(Si) grain. The coefficient a_2 reflects the Herzer's predicted effective magnetic anisotropy of the nanocrystalline material,

where as in amorphous alloys it is postulated as being caused by local stress and magneto elastic coupling. M_S has been observed to increases in order with condition $Ag > Cu > Au$. It is observed that while the ribbon with composition $Fe_{73.5}Ag_1Nb_3Si_{13.5}B_9$ reaches it saturation value around 5kOe, $Fe_{73.5}Cu_1Nb_3Si_{13.5}B_9$ around 4kOe and $Fe_{73.5}Au_1Nb_3Si_{13.5}B_9$ requires 4.5kOe. The saturation magnetizations are shown in Table 4.12.

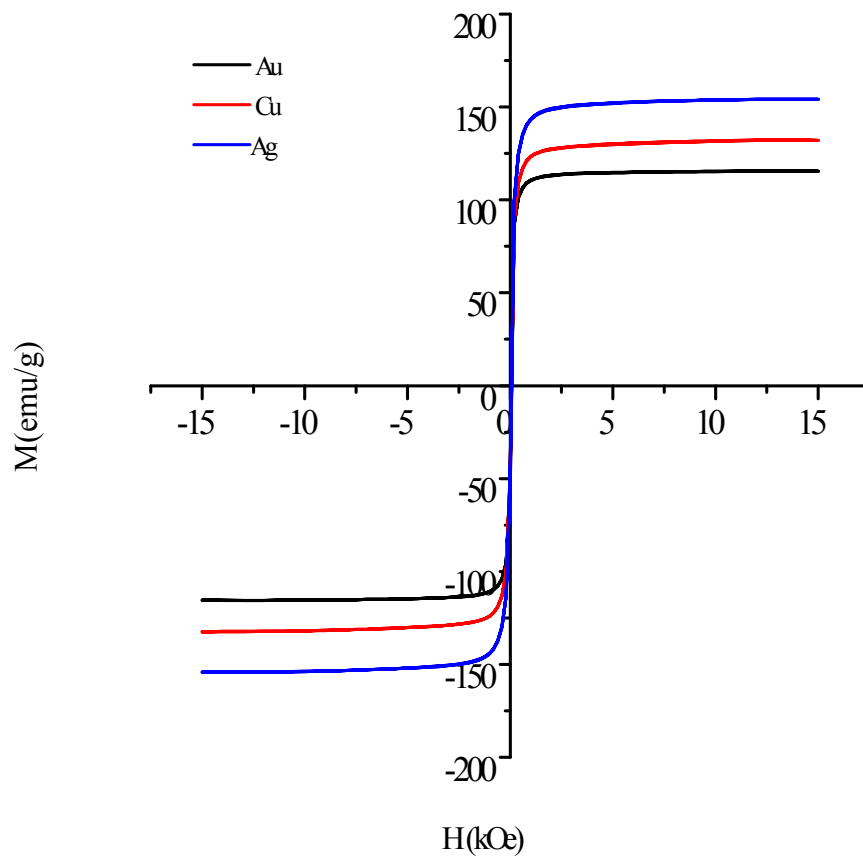


Figure4.20 Field dependence of specific magnetization of as-cast sample of $Fe_{73.5}X_1Nb_3Si_{13.5}B_9$ [$X = Cu, Au \& Ag$] ribbon alloys at room temperature

Table 4.12 Curie temperature and saturation magnetization of nanocrystalline amorphous ribbons with $\text{Fe}_{73.5}\text{X}_1\text{Nb}_3\text{Si}_{13.5}\text{B}_9$ alloys

X-content	Saturation Magnetization M_s in emu/s at room temperature	Magnetization M in emu/s at 10 kOe	Curie Temperature T_c in $^\circ\text{K}$	Curie Temperature T_c in $^\circ\text{C}$
Cu	132.14	132.14	692	419
Au	115.47	115.47	667	394
Ag	154	154	653	380

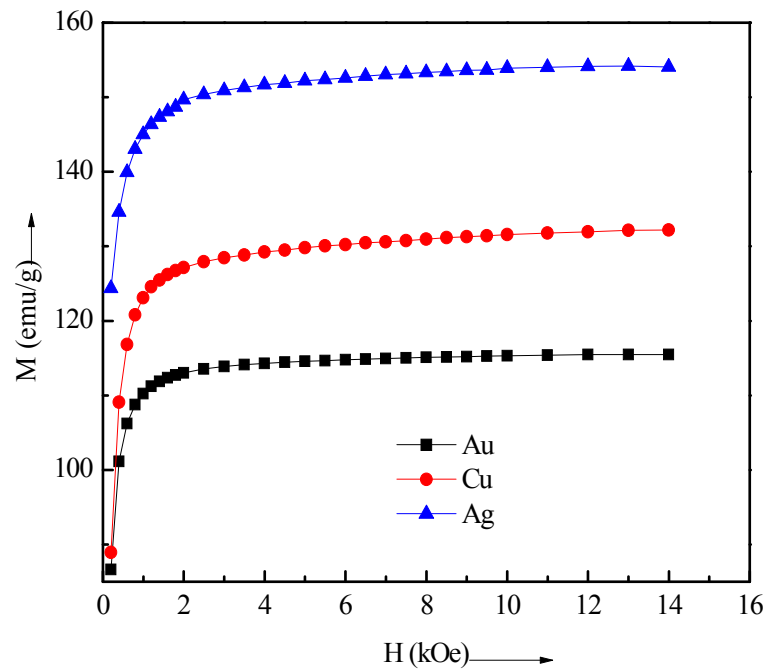


Figure 4.21 Field dependence of magnetization of amorphous $\text{Fe}_{73.5}\text{X}_1\text{Nb}_3\text{Si}_{13.5}\text{B}_9$ [X = Cu, Au & Ag] ribbon alloys at room temperature

Magnetization is also evaluated as a function of field to find the dependence of magnetization on the domain structure. Magnetic saturation can be achieved only for Fe-based alloys. In these cases, the total anisotropy is small and the next neighbor exchange coupling leads to ferromagnetic order. The critical composition for the disappearance of ferromagnetism full of curve M_s with the replacement Cu by Ag or Au, where the nearest neighbor coupling is no longer dominant and an intermediate range occur.

4.5.1 Temperature Dependence of Specific Magnetization $\text{Fe}_{73.5}\text{X}_1\text{Nb}_3\text{Si}_{13.5}\text{B}_9$ [X = Cu, Au & Ag] Nanocrystalline Amorphous Ribbons

The variation of saturation magnetization (M_s) as a function of temperature in the range 300 k to 800 k measured with an applied field of 10kOe in the amorphous state for the nanocrystalline amorphous samples with composition $\text{Fe}_{73.5}\text{X}_1\text{Nb}_3\text{Si}_{13.5}\text{B}_9$ [X = Cu, Au & Ag] are shown in figure 4.22(a), 4.22(b) and 4.22(c). The magnetization of all the samples decreases gradually with increasing temperature since the thermal energy is acting on opposition to the magnetic coupling or exchange energy between neighboring atoms. The numerical value's of Curie temperature (T_c) for the samples are shown in Table 4.12. Well defined values of T_c obtained from our measurements support the fact that in spite of chemical and structural disorder, ferromagnetic glasses have well defined magnetic ordering temperature.

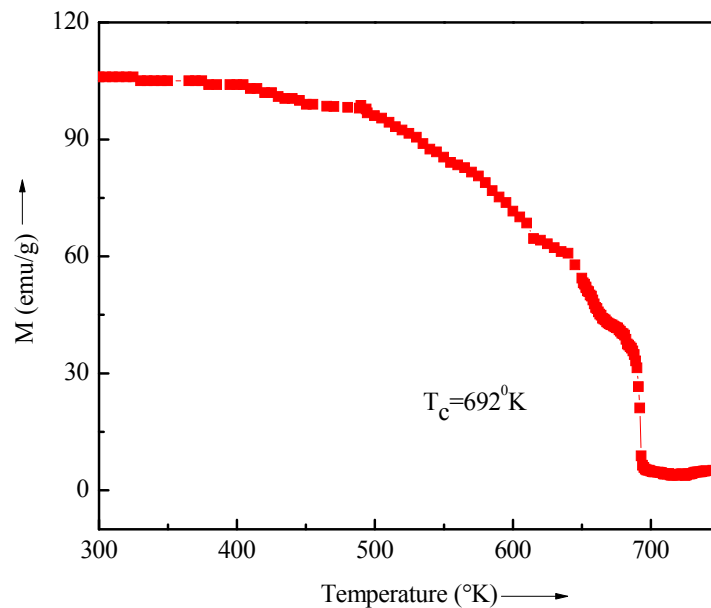


Figure 4.22(a) Temperature dependence of specific magnetization of amorphous nanocrystalline ribbons with composition $\text{Fe}_{73.5}\text{Cu}_1\text{Nb}_3\text{Si}_{13.5}\text{B}_9$ alloy

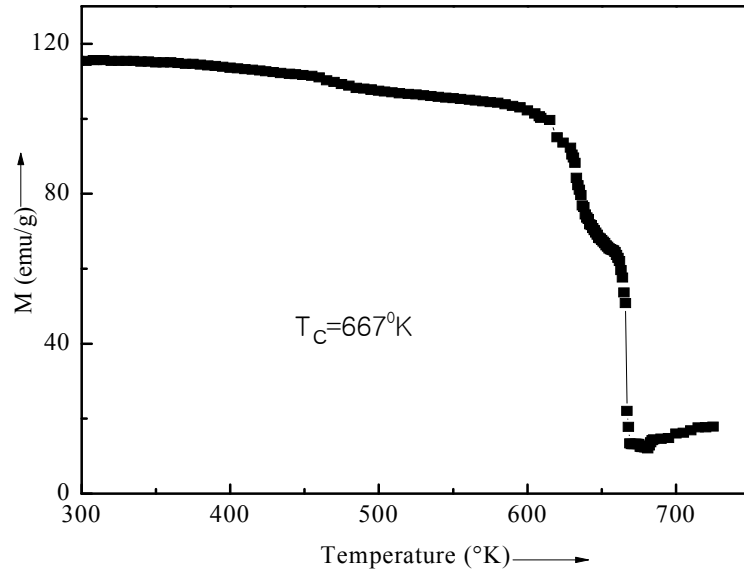


Figure 4.2(b) Temperature dependence of specific magnetization of amorphous nanocrystalline ribbons with composition $\text{Fe}_{73.5}\text{Au}_1\text{Nb}_3\text{Si}_{13.5}\text{B}_9$ alloy

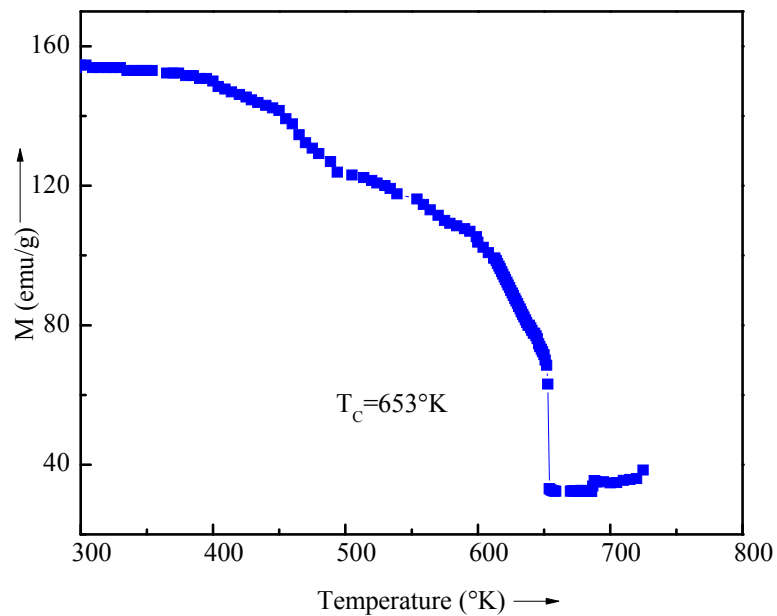


Figure 4.22(c) Temperature dependence of specific magnetization of amorphous nanocrystalline ribbons with composition $\text{Fe}_{73.5}\text{Ag}_1\text{Nb}_3\text{Si}_{13.5}\text{B}_9$ alloy

From these curve T_c has been determined as the temperature corresponding to the inflexion point where the rate change of magnetization with respect to temperature is maximum shown in figure 4.23(a), 4.23(b) and 4.23(c). As the temperature approaches to the T_c , magnetization falls more rapidly near to zero as the thermal energy exceeds the magnetic ordering or the exchange energy. The reduction of T_c with the substitution of Cu by Au or Ag in order $Ag < Au < Cu$ may be attributed to this simultaneous weakening of the strength of exchange interaction between the Fe magnetic moments.

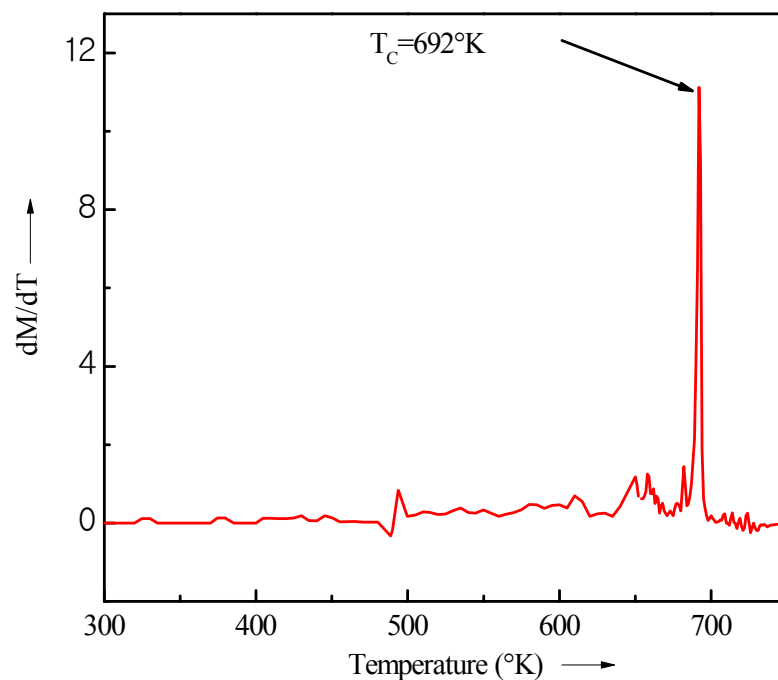


Figure 4.23(a) $\frac{dM}{dT}$ versus temperature curve of amorphous Nanocrystalline ribbons with composition $Fe_{73.5}Cu_1Nb_3Si_{13.5}B_9$ alloy

The sharp fall of M_s at T_c indicates that the material is quite homogeneous for the point to view of amorphosity the sharp fall of M_s are observed at $419^{\circ}C$ for sample $Fe_{73.5}Cu_1Nb_3Si_{13.5}B_9$, $394^{\circ}C$ for sample $Fe_{73.5}Au_1Nb_3Si_{13.5}B_9$ and $340^{\circ}C$ for the sample $Fe_{73.5}Ag_1Nb_3Si_{13.5}B_9$ from figure 4.22(a), 4.22(b) and 4.22(c). The accurate determination of T_c of amorphous material is really difficult due to irreversible components of the structural relaxation like long range internal stress, topological and chemical short range order. Therefore during the measurement of T_c of the heating

rate should be adjusted in such a way so that no substantial relaxation and crystallization takes place. In our experiment we use heating rate of about 5°C/min. that is frequently used for amorphous ribbon. Therefore the initial amorphous state should be taken into account. Increase in packing density of atoms in order to Cu > Au > Ag have significant contribution in the enhancement of T_c in amorphous state. These microstructural effects bring about a change in the inter atomic distances, which directly affect the strength of the exchange interaction resulting in a change of T_c 's. From the above measurements it has been elucidated that the thermo magnetic measurement is a powerful technique to analyze the crystallization behavior of amorphous ferromagnetic materials provided the crystallization material and the T_c 's of amorphous alloys lie below the crystallization temperature.

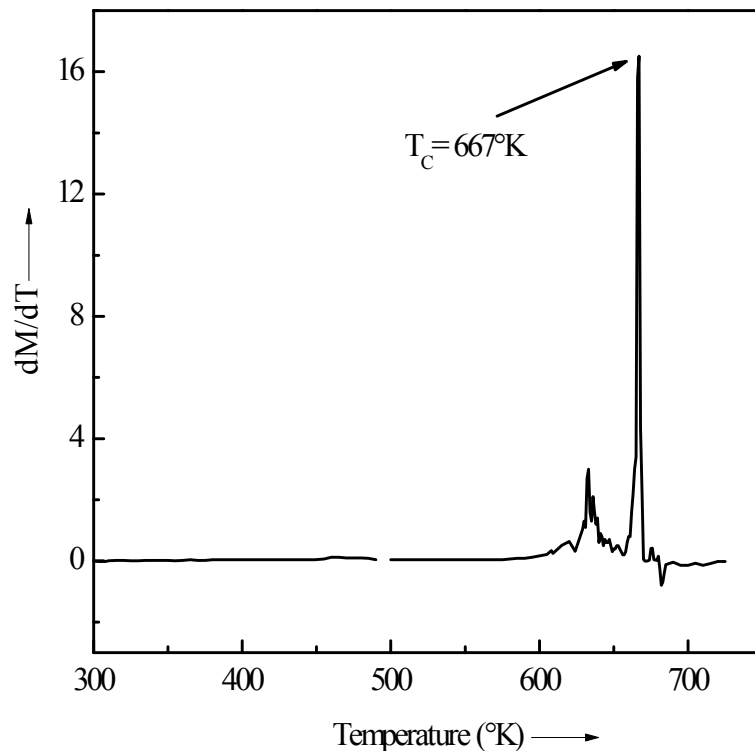


Figure 4.23(b) $\frac{dM}{dT}$ versus temperature curve of amorphous Nanocrystalline ribbons with composition $\text{Fe}_{73.5}\text{Au}_1\text{Nb}_3\text{Si}_{13.5}\text{B}_9$ alloy

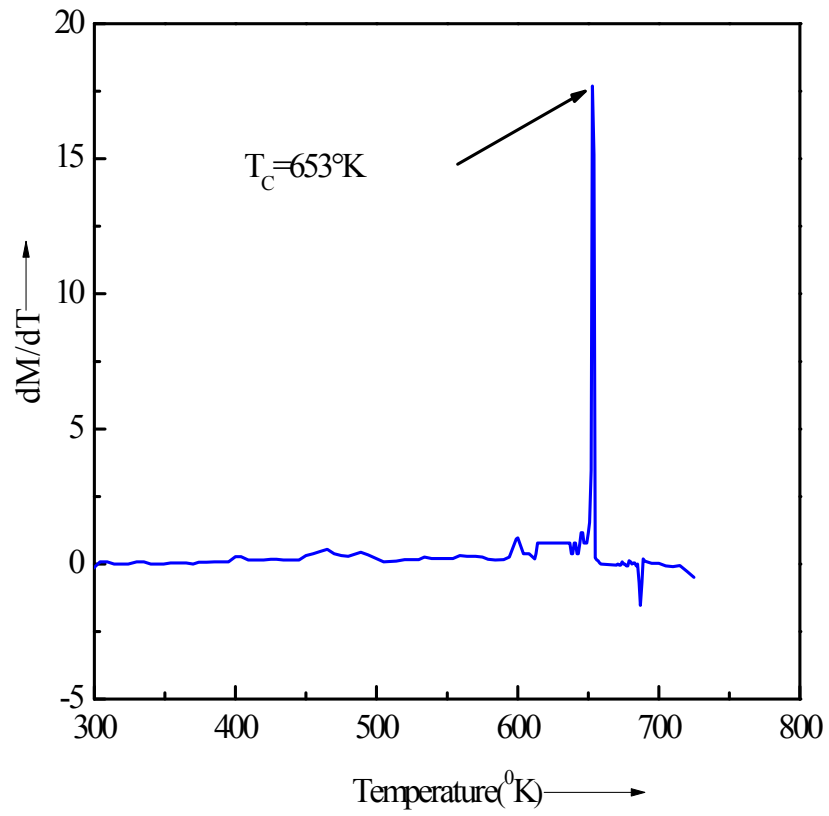


Figure 4.23(c) $\frac{dM}{dT}$ versus temperature curve of amorphous Nanocrystalline ribbons with composition $\text{Fe}_{73.5}\text{Ag}_1\text{Nb}_3\text{Si}_{13.5}\text{B}_9$ alloy

CONCLUSIONS

5.1 Conclusions

Nanocrystalline amorphous ribbon of the FINEMET family and originally proposed composition $\text{Fe}_{73.5}\text{Cu}_1\text{Nb}_3\text{Si}_{13.5}\text{B}_9$ has been studied and other two composition Cu replacement with Au and Ag. Three sets of nanocrystalline alloy were chosen with composition $\text{Fe}_{73.5}\text{Cu}_1\text{Nb}_3\text{Si}_{13.5}\text{B}_9$, $\text{Fe}_{73.5}\text{Au}_1\text{Nb}_3\text{Si}_{13.5}\text{B}_9$ and $\text{Fe}_{73.5}\text{Ag}_1\text{Nb}_3\text{Si}_{13.5}\text{B}_9$ has been studied to find out the correlation between microstructural features and magnetic properties dependent on various stages of nanocrystallization during the isothermal annealing around the crystallization temperature of their amorphous precursor. The crystallization behavior of the sample was investigated by DTA and XRD experiments. The amorphous and annealed samples were examined by XRD to identify the microstructure of the samples. Microstructural changes and crystallization process in Fe-Cu-Nb-Si-B amorphous alloys in order to elucidate the roles of combined addition of Nb and Cu replacement with Au or Ag. This turn has been aimed at furthering the understanding of crystallization of FINEMET alloys. Magnetization measurement as a function of temperature and field were performed by VSM.

The magnetic phase transition temperature, i.e Curie temperature was obtained from temperature dependence magnetization measurement. From the systematic investigation on the crystallization structural and magnetic properties the following conclusion can be obtained:

- (i) DTA experiment was performed for five different rates 10 to 50°C/min in steps of 10⁰C/min up to a temperature of 800°C. DTA reveals the primary and secondary crystallization onset temperature with the manifestation of two well defined exothermic peaks corresponding to nanocrystallization α -Fe(Si) (T_{x_1}) and Fe_2B (T_{x_2}) phases respectively. First crystallization phase T_{x_1} indicates stability of amorphous state of structural stability and magnetic ordering values of T_{x_1} are observed 513°C for $\text{Fe}_{73.5}\text{Cu}_1\text{Nb}_3\text{Si}_{13.5}\text{B}_9$, 522.4°C for $\text{Fe}_{73.5}\text{Au}_1\text{Nb}_3\text{Si}_{13.5}\text{B}_9$ and 575°C for $\text{Fe}_{73.5}\text{Ag}_1\text{Nb}_3\text{Si}_{13.5}\text{B}_9$ with heating rate 20°C/min. The order of the three samples with respect to their crystallization temperature range and peak temperature can be arranged by the following ways $\text{Fe}_{73.5}\text{Ag}_1\text{Nb}_3\text{Si}_{13.5}\text{B}_9 > \text{Fe}_{73.5}\text{Au}_1\text{Nb}_3\text{Si}_{13.5}\text{B}_9 >$

$\text{Fe}_{73.5}\text{Cu}_1\text{Nb}_3\text{Si}_{13.5}\text{B}_9$. The knowledge of crystallization temperature has been fruitfully utilized during the isothermal annealing of these amorphous ribbons for nanocrystallization which ultimately controls the magnetic properties of FINEMET alloys. The advantages realized are higher saturation induction and better thermal stability with soft magnetic properties at application temperature.

- (ii) The temperature difference between two crystallization peaks ($T_{p_2}-T_{p_1}$) are found to exist around 146°C for Cu, 140.3°C for Au and 165°C for Ag at constant heating rate 20°C/min. The saturation temperature is important for stability of $\alpha\text{-Fe(Si)}$ phase against detrimental Fe_2B phase while it is necessary for fabrication of higher quality inductors.
- (iii) The activation energy of the first crystallization phase $\alpha\text{-Fe(Si)}$ and second crystallization phase Fe_2B phase calculated using Kissinger's plot. Activation energy of $\alpha\text{-Fe(Si)}$ phase of all the samples are shown in the range 2.18eV - 4.37eV. But for the present sample FINEMET value 2.18eV which is higher than the above range in Cu replacement with Au and Ag. The activation energy of Fe_2B phase are varies 3.62 - 4.45eV. The nature of Fe_2B phase also maintain this order $\alpha\text{-Fe(Si)}$ phase. The composition of the alloys affected both the crystallization phases because the time needed for the constituent atom to have long range order depends on their bond energies.
- (iv) The amorphous stage of the as- cast ribbon has been confirmed by XRD. The evolution of the primary phase on annealed samples has been confirmed as $\alpha\text{-Fe(Si)}$ and their sizes have been determined from the line broadening of fundamental peaks (110) from XRD pattern as affected by annealing around the crystallization temperature. The crystallization phases of amorphous $\text{Fe}_{73.5}\text{Cu}_1\text{Nb}_3\text{Si}_{13.5}\text{B}_9$ alloy annealed at temperature in the range of 600°C to 800°C for 30 minutes is $\alpha\text{-Fe(Si)}$ phases with average grain size 14 to 20 nm. After heating above its crystallization temperature nanometric crystal with average grain grown in the amorphous matrix are 13 - 30 nm for $\text{Fe}_{73.5}\text{Au}_1\text{Nb}_3\text{Si}_{13.5}\text{B}_9$ and 9 - 30 nm for $\text{Fe}_{73.5}\text{Ag}_1\text{Nb}_3\text{Si}_{13.5}\text{B}_9$. This is quite reasonable since their crystallization onset temperature is 650°C and higher. The lattice parameter and Si at%

shows an inverse relationship indicating that Si diffuses out of α -Fe(Si) grain for which the size of α -Fe lattice is regained. The improvement of magnetic properties with increase of annealing temperature is mainly connected with the microstructure i.e with the certain of free randomly oriented α -Fe(Si) grain in the residual matrix. According to our experimental result alloys are annealed in a certain temperature in minimum size of the α -Fe(Si) grain 14nm at 600⁰C for Cu-based, 13 nm at 600⁰C for Au-based and 9nm at 700⁰C for Ag-based samples.

- (v) The saturation magnetization (M_s) values of all the studied samples at room temperature in order with condition Ag > Cu > Au. Magnetic saturation can be achieved only for Fe based alloys. In this Fe content all the samples are same. In this case the critical composition for the disappearance of ferromagnetism full of curve M_s with replacement Cu by Ag or Au, where the nearest neighbor coupling is no longer dominant and an intermediate range occur.
- (vi) The curie temperature of all the samples has been determined by temperature dependence saturation magnetization. The sharp fall of M_s at T_c indicates that the material is quite homogeneous for the point to view of amorphosity the sharp fall of M_s are observed at 419⁰C for Cu 394⁰C for Au and 380⁰C for Ag. In our experiment increase in packing density of atoms in order to Cu > Au > Ag have significant contribution in the enhancement of T_c in amorphous state.

Finally, concluded that promising initial results on FINEMET alloy suggest Cu replace Au or Ag that might also find their way in high temperature soft magnetic applications. The play ground of microstructural engineering of soft magnetic properties will undoubtedly after new discoveries for future materials scientist and engineers.

5.2 Scope for Future Work.

There is much scope for further research in controlling the magnetic characteristics by changing composition and heat treatment. Certain improvement parameters like complex initial permeability, quality factor, magnetic anisotropy and magnetostriction can be studied in detail for a better understanding of microstructure

property relationship of FINEMETT types as well as composition of Cu replacement Ag or Au. Moreover, different composition samples forming techniques and heat treatment should be further investigated in order to optimize all properties.

REFERENCES

Chapter I

- [1.1] Kulik T., Hernando A. and Vasquez M.; “Correlation between structure and the magnetic properties of amorphous and nanocrystalline $\text{Fe}_{73.5}\text{Cu}_1\text{Nb}_3\text{Si}_{22.5-x}\text{B}_9$ [X = Cu, Ag & Au] alloys”, J. Magn. Magn. Mater., **133**, 310, 1994.
- [1.2] Jing Zhi, Kai-Yuan He, Li-Zhi Cheng and Yu-Jan Fu; “Influence of the elements Si/B on the structure and magnetic properties of nanocrystalline $(\text{Fe,Cu,Nb})_{73.5}\text{Si}_x\text{B}_{22-x}$ [X = Cu, Ag & Au] alloys”; J. Magn. Magn. Matter 9, **153** 315, 1996.
- [1.3] Kane S. N, Sarabhai S., Gupta A., Varga L. K., Kulit T.; “Effect of quenching rate on crystallization in $\text{Fe}_{73.5}\text{Cu}_1\text{Nb}_3\text{Si}_{22.5-x}\text{B}_9$ alloys”; J. Magn. Magn. Mater., **215-216**, 372, 2000.
- [1.4] Bigot J., Lecaude N., Perron J. C., Millan C., Ramiarinjaona C. and Riolland J. F., “Influence of annealing condition on nanocrystallization and magnetic properties in $\text{Fe}_{73.5}\text{Cu}_1\text{Nb}_3\text{Si}_{22.5-x}\text{B}_9$ [X = Cu, Ag & Au] alloy”, J. Magn. Magn. Matter., **133**, 29, 1994.
- [1.5] Hasiak M., Zbroszczyk J., Olszewki J., Ciuzynska W. H., Wyslocki B., Blachowicz A., “Effect of cooling rate on magnetic properties of amorphous and nanocrystalline alloys”; **215-216**, 410, 2000.
- [1.6] Saroaut Noor, Sikder S. S., Saha D. K. and Hakim M. A, “Time and temperature dependence of nanocrystalline and initial permeability of FINEMET alloy”; Nuclear science and application, No.15, 13-19, June 2006.
- [1.7] Saroaut Noor; M Phil Thesis, “Effects of two step annealing on complex permeability of Fe-Cu-Nb-Si-B nanocrystalline soft magnetic materials” Department of Physics, KUET, Khulna, March 2005
- [1.8] Yoshizawa Y., Osuma S., Yamauchi K.; “New Fe-based soft magnetic alloys composed of ultra-fine grain structure”, J. Appl. Phys., 6044 – 6046, 1998.
- [1.9] Herzer G.; “Grain size dependence of coercivity and permeability in nanocrystalline ferromagnets”; IEEE Trans. Magn., 26, 1397-1402, 1990.
- [1.10] Herzer G.; “Magnetization process in Nanocrystalline Ferro magnets”, Mat. Sci. Eng., A133, 1 – 5, 1991.

- [1.11] Herzer G; "Nanocrystalline soft magnetic alloys"; In Hand Book of Materials, Vol.10 Ed; H. H. J Buschow, Elsevier Puls.Co. 1997
- [1.12] Hakim M. A. and Hoque S. M; "Effect of structural parameters on soft magnetic properties of two phase nanocrystalline alloy of $Fe_{73.5}Cu_1Ta_3Si_{13.5}B_9$ " J. Magn. Mater. (JMMM), 284, P.395 – 402, 2004.
- [1.13] Mondal S. P, Kazi Haniun Maria, Sikder S. S, Shamima Chowdhury, Saha D. K. and Hakim M. A., "Influence of annealing conditions in Nanocrystalline and ultra-soft magnetic properties of $Fe_{73.5}Cu_1Nb_3Si_{13.5}B_9$ ", J. Mater. Sci. Technol, 28 (i), 21 – 26, 2012.
- [1.14] Kazi Haniun Maria, Mondal S. P, Shamima Chowdhury, Sikder S. S, Hakim M. A. and Saha D. K; "Effect of annealing temperature on the soft magnetic properties of $Fe_{75.5}Cu_1Nb_1Si_{13.5}B_9$ Amorphous alloys", Journal Emerging Trends sciences (JETEAS), 2 (i), 102 - 108, 2011
- [1.15] Jing Zhi, Kai-Yuan He, Li-Zbi Ching and Yu - Jan Fu; "Influence of the elements Si/B on the structure and magnetic properties of nanocrystalline $(Fe, Cu, Nb)_{77.5}Si_xB_{22.5-x}$ Alloys". J. Magn, Magn. Mater, 153, 315, 1996.
- [1.16] Hakim M. A; "Magnetic softening of nanocrystalline FeCuNbSiB alloys on annealing", J. Bangladesh Electronic Society; Vol. 4, pp. 44 – 45, 2004.
- [1.17] Lim S. M., Pi W. K., Noh T. H., Kim H. and Jand Karg I .K.; "Effects of Al on the magnetic properties of nanocrystalline $Fe_{73.5}Nb_3Cu_1Si_{13.5}B_9$ alloys"; J. Appl. Phys. ; Vol. 73, No. 10, 15 May 1993.
- [1.18] Saroaut Noor, Sikder S. S., Saha D. K. and Hakim M. A.; "Time and Temperature dependence of nanocrystallization and Initial permeability of FINEMET Alloy" ; Nuclear Science and applications, Vol. 15, No. 1, 9 - 13, 2006.
- [1.19] Herzer. G; "Nanocrystalline soft magnetic alloys", In Handbook of materials", Vol.10ed, Buschow K. H. J, Elsevier pub.co.
- [1.20] Hakim M. A. and Hoque S. M; "Effect of structural parameters on soft magnetic properties of two phase nanocrystalline alloys of $Fe_{73.5}Nb_3Cu_1Si_{13.5}B_9$," Magn. J. Magn. Mater.(JMMM), 284, pp.395 -402, 2004.

- [1.21] Saha D. K. and Hakim M. A.; “Crystallization behavior of amorphous nanocrystalline soft magnetic alloys”, Bangladesh Academy of Science, Vol. No.2, pp.177-187, 2006.
- [1.22] Yoshizawa Y. and Yamachi K.; “Magnetic properties of Fe-Cu-M-Si-B M = Cr, V, Mo, Nb, W) alloy”, Mater. Sci. Eng. A(b)133,176,1991.
- [1.23] Müller M. and Matern N.; “The influence of refractory element addition on the magnetic properties and on the crystallization behavior of nanocrystalline soft magnetic Fe-B-Si-Cu alloys”, J. Magn. Magn. Mater. 136,79,1994.
- [1.24] Roy P. K.; M. Phil Thesis, Depart of Physics, KUET, Khulna, May-2007
- [1.25] Herzer.G; In Buschow KHJ Editor, “Hand book of magnetic materials”, Amsterdam: Elsevier Science, 10, 415, 1997.
- [1.26] Saroaut Noor, Sikder S. S., Saha D. K. and Hakim M. A.; “Time and Temperature dependence of nanocrystallization and Initial Permeability of FINEMET Alloys”, Nuclear Science and Applications, Vol.15, no.1, 9-13, 2006
- [1.27] Franco V., Conde C. F. and Conde A; “Magnetic properties and crystallization of a $\text{Fe}_{63.5}\text{Cr}_{10}\text{Cu}_1\text{Nb}_3\text{Si}_{13.5}\text{B}_9$ alloy”; J. Magn. Magn. Mater., 203; 60-62, 1999
- [1.28] Mondal S.P, Kazi Hanium Maria, Sikder S.S, Shamima Choudry, Saha D.K and Hakim M.A, “ Influence of annealing Condition on Nanocrystalline and Ultra –Soft magnetic Properties of $\text{Fe}_{73.5}\text{Nb}_3\text{Cu}_1\text{Si}_{13.5}\text{B}_9$ alloy”; J. Mater. Sci. Technol., 28(1), 21-26,2012
- [1.29] Manjura Haque S. and Hakim A., “Ultra soft magnetic properties of verified $\text{Fe}_{73.5}\text{Cu}_{0.6}\text{Nb}_2\text{Si}_{13}\text{B}_{8.5}$ ” J. Material Chemistry and Physics, **101**, 112-117, 2007
- [1.30] Franco V, Conde C. F., Conde A. and Kiss L. F.; “Super paramagnetic behavior in $\text{Fe}_{76}\text{Cu}_1\text{Nb}_3\text{Si}_{10.5}\text{B}_{9.5}$ alloy”, J. Magn. Magn. Mater., 215-216, 400-403, 2000.
- [1.31] Hakim M. A., “Magnetic Softening of nanocrystalline Fe-Cu-Nb-Si-B alloys on annealing”; J. Bangladesh Electronic society, Vol.4, pp.40-45, 2004.

- [1.32] Zashed Iqbal, M. Phil. Thesis, "The Effect of Grain size and Phase constitution on the Magnetic Properties of higher content Cr substituted $\text{Fe}_{73.5-x}\text{Cr}_x\text{Nb}_3\text{Cu}_1\text{Si}_{13.5}\text{B}_9$ Nanocrystalline Alloys" Department of Physics, KUET, Khulna, July 2015
- [1.33] Slawska A., Wanicwska M., Gutowski H., Lachowicz, Kulik T. and Matiya M., Phys. Rev. B46, 14 594, 1992.
- [1.34] Lachowicz H. K., Slawska A. and Wanicwska; J. Magn. Magn. Mater., 133, 238, 1994.
- [1.35] Sultan Mahmud Md., Sikder S. S. and Hakim M. A.; "Crystallization behavior and initialization permeability of FeCrCuNbSiB nanocrystalline alloys", Journal of Science & Arts, Issue 1. 33-41, 2004
- [1.36] Chau N., Thanh P. Q., Hoa N. Q. and N. D., "The existence of giant magneto caloric effect and laminar structure in $\text{Fe}_{73.5-x}\text{Cr}_x\text{Nb}_3\text{Cu}_1\text{B}_9$ " J. Magn. Magn. Mater. **304** 36-40 2006
- [1.37] Chau N, Hue P. T., Hoa N. Q., Anh D., Luong N. H., Asgar M. A., Sikder S. S., Sultan Mahmud Md., "An Existence of Laminar structure in nanocrystalline ribbon in finemet with partial substitution of Fe by Cr" proceeding of the seventh vietamese- German seminar.
- [1.38] Saha D. K., and Hakim M. A., "Crystallization behavior of $\text{Fe}_{73.5}\text{Au}_1\text{Nb}_3\text{Si}_{10.5}\text{B}_{9.5}$ Amorphous Nanocrystalline soft Magnetic Alloy" Bangladesh Academy of Science, Vol. 30N 2, P. 177-187, 2006.
- [1.39] Hakim M. A., Sikder S. S., Sultan Mahmud Md. and Manjura Haque S.; Dilution of magnetic moment of Fe by Cr for $\text{Fe}_{73.5-x}\text{Cu}_1\text{Cr}_x\text{Nb}_3\text{Si}_{13.5}\text{B}_9$ and field cooled and zero field cooled behavior for higher Cr-content'; Journal of Korean Physical Society (JKPS), Vol.52, No.5, 2008
- [1.40] Müller M., and Marten N.; " The influence of refractory element additions on the magnetic properties and on the crystallization behavior of nanocrystalline soft magnetic Fe-b-Si-Cu alloys", J. Magn. Magn. Mater., 136,79, 1994.
- [1.41] Inoue A., Kabayashi K., Kanerhira J. and Masumoto T., " Mechanical properties and thermal stability of (Fe-Co-Ni)-M-B (M = IV, V, and VI group transition metals) amorphous alloys with low boron concentration", Sci. Rep. Res. Inst., Tohoku Univ. Vol. A 29, p 331-342.1981.
- [1.42] Suzuki K., Makino A., Kataoka N., Inoue A., and Masumoto T., "Soft magnetic properties of nanocrystalline bcc Fe-Zr-B and Fe-M-B-Cu (M

- =Transition metal) alloys with high saturation magnetization”, J. Appl. Phys., 70(10), 6232,), 1991
- [1.43] Suzuki K., Makino A., Inoue A., and Maximoto T; “Low core losses of nanocrystalline Fe-M-B (M=Zr, Hf or Nb) alloys”, J. Appl. Phys. 74, 336, 1993
- [1.44] Franco V, Conde C. F., Conde A., Kiss L. F., “ Super paramagnetic behavior in a Fe₇₆Cu₁ Nb₃ Si_{10.5} B_{9.5} alloy”, J. Magn. Magn. Mater., 215-216, 400-403, 2000.
- [1.45] Ayers J. D., Hans V. G., Sprague J. A., Elan W. T.; “On the role of Cu and Nb in the formation of nanocrystals in amorphous Fe_{73.5}Cu₁Cr_xNb₃Si_{13.5}B₉”, Appl. Phys. Let., 64, 974,1994
- [1.46] Herzer.G; Hand Book of Magn. Mater., **10**, 427, 1997
- [1.47] Kubaschenski O., “Iron-Binary Phase Diagram”, (Springer- Verlag, Berlin, Heidelberg, New York) 1982.
- [1.48] Kazi Hanimun Maria, Siba P. Mondol, Shamima Choudhury, Sikder S. S., Hakim M. A. and Saha D. K.; “Effect of annealing temperature on the soft magnetic properties of Fe_{73.5-x}Cu₁Cr_xNb₃Si_{13.5}B₉ amorphous alloys” Journal emerging Trends Science (JETEAS), 2(1); 102-108, 2011
- [1.49] Ohnuma O, Pins D. H., Abet T., Onodera H. and Hono K.; “Optimization of the microstructure and properties of Co substituted Fe-Si-B-Nb-Cu nanocrystalline soft magnetic alloys,” J. Appl. Phys., Vol. 11, P.1986-1994, 1 June 2003.

Chapter II

- [2.1] Yoshizawa Y., Oguma S and Yamauchi K; “New Fe-based soft magnetic amorphous alloys composed of ultrafine grain structure”, J. Appl. Phys. 64(10), 6044 – 6046, 1988.
- [2.2] Herger G.; “Grain size dependence of coercivity and permeability in nanocrystalline ferromagnets”, IEEE Trans. Magn. 26(5), 1397 – 1402, 1990.
- [2.3] McHenry M. A., Willard M. A. and Laughlin D. E.; “Amorphous and nanocrystalline materials for applications as soft magnets”, Prog. Mat. Sci. 44, 291- 433, 1999.
- [2.4] Alben R., Budnic J. I. and Gargil G. S.; “a_{III} Metlicglassess; American SOC for metals”, pp304, 1978.

- [2.5] Slawska – Waniewska A., Nowicki P., Lachowicz H. K., Gorria P., Barandiarra J. M. and Hernando A.; “Magnetic interactions in Fe-Zr-B-Cu nanocrystalline materials at elevated temperature”, *Phys. Rev. B* 50(9), 6465 – 6467, 1994.
- [2.6] Bean C. P. and Livingston J. D.; “Superparamagnetism”, *J. Appl. Phys.* 30(4), S120, 1959.
- [2.7] G. Herzer; “Nanocrystalline Soft Magnetic Alloys”; *Hand Book of Materials*, K. H. J. Buchow (ed), 10, 415-462, 1997
- [2.8] Y. Yoshizawa, S. Ogma and K. Yamauchi; “New Fe-Based Soft Magnetic Alloys Composed of Ultra-fine Grains Structure”; *J. Appl. Phys.* 64, 6044, 1988
- [2.9] Y. Yoshizawa and K. Yamachi; “Magnetic Properties of Fe-Cu-M-Si-B (M = Cr, V, Mo, Nb, Ta, W) alloy”; *Mater. Sci. Eng. A (b)*. 133, 176, 1991
- [2.10] Y. Yoshizawa and K. Yamachi; “Fe-based soft magnetic alloys composed of ultra-fine grains structure”; *Mater. Trans. JIM. (a)* 31, 307, 1990
- [2.11] G. Herzer and Warlimont H.; “Nanocrystalline soft magnetic materials by partial crystallization of amorphous alloys”, *Nanostructured materials* 1, 263-268, 1992
- [2.12] Hono K., Higara K., Wang Q., Inoue A. and Sakurai T.; “The microstructure evolution of a $\text{Fe}_{73.5}\text{Nb}_3\text{Cu}_1\text{Si}_{13.5}\text{B}_9$ nanocrystalline Soft Magnetic material”; *Acta. Metall. Mater.* 40(9) 2137-2147, 1992
- [2.13] Hono K. and Sakurai T.; “Atom Probe studies of nanostructured alloys”; *Appl. Surf. Sci.* 87/88,166, 1995
- [2.14] Ayers J. D., Harris V. G., Sprague J. A. and Elan W. T.; “On the role of Cu and Nb in the formation of nanocrystals in amorphous $\text{Fe}_{73.5}\text{Nb}_3\text{Cu}_1\text{Si}_{13.5}\text{B}_9$ ”, *Appl. Phys. Lett.* 64, 974, 1994.
- [2.15] Koster U., Schonmann M., Blank-Bewersdorff S. Brauer, Sutton M. and Stephemon G. B.; “Nanocrystalline materials by crystallization of metal-metalloid glasses”, *Mat. Sci. Eng.* **A133**, 611-615, 1991
- [2.16] Yoshizawa Y. and Yamauchi K.; “Magnetic Properties of Nanocrystalline Fe-Based Soft Magnetic Alloys”, *Mater. Res. SOC. Symp. Proc.* 232, 183 1991a.
- [2.17] Herzer G.; In: *Proc of Int. Symp. On 3ab Transition-Semi Metal Thin Films. Magnetism and Processing (Japan SOC for the promotion of Science, Committee, Sendia, Japan)* **131** 130, 1991
- [2.18] Warliment H.; *Mater. Sci. Eng.* 99, 1988

- [2.19] Makino A., Inoue A. and Masumoto T.; *Mat. Trans. JIM* **36**, 924, 1995
- [2.20] Martin J. W., Doherty R. D. and Canter B.; “Stability of microstructure in metallic systems”; Cambridge, UK, 1997
- [2.21] Kauzmann W.; *Chem. Rev.*; **43** PP. 219-256, 1948
- [2.22] *The IUPAC Compendium of Chemical Terminology*, **66** 583, 1997
- [2.23] Jones H., *Rep. Prog. Phys.*, **36** 1425, 1973
- [2.24] Turnbull D., *J. dc physique*, **35** C4-1, 1974
- [2.25] Takayama S.; “Amorphous structure and their formation and stability”; *J. Materials Sci.* Vol. 11(1) 164-185, 1976
- [2.26] Irvine J. T. S., Amano E., Huanosta A., Valenzuela R. and West A. R.; “Solid State should peak at T_c ”; *Ionic* 40/41, 220, 1990
- [2.27] Cohen M. H. and Turnbull D.; “Composition Requirements for Glass Formation in Metallic and Ionic Systems”; *Nature* 189 131-132, 1961
- [2.28] Gargil G., III; *J. Appl. Phys*, 41, 2248, 1970
- [2.29] Chen H. S.; *Acta. Mat.* 22, 1505, 1974
- [2.30] Nageland S. R. and Taue J.; “Nearly- free- electron Approach to the theory of Metallic Glass Alloys”; *Phys. Rev. Lett.*, 35, 380, 1975
- [2.31] Berkowitz A. E., Walter J. L. and Wall K. F.; “Magnetic Properties of amorphous particles produced by Spark Erosion”; *Phys. Rev. Lett.* 46, 1484, 1981
- [2.32] Murray P. and White J.; “Kinetics of the thermal dehydration of clays”; *Trans. Brit. Ceram. SOC.* 48, 187-206, 1949
- [2.33] Murray P. and White J.; “Kinetics of the thermal decomposition of clay 2, Isothermal decomposition of clay materials”; *Trans. Brit. Ceram. SOC.* 54, 151-187, 1955
- [2.34] Murray P. and White J.; “Kinetics of the thermal decomposition of clay 4, Interpretation of the differential thermal analysis of clays”, *Trans. Brit. Ceram. Soc.* 54, 204-237, 1955

- [2.35] Sewel E. C.; “The consequences for differential thermal analysis of assuming a reaction to be first order”; Clay Minerals Bul. 2, 233-241, 1955
- [2.36] Kissinger H. E.; “Reaction Kinetics in Differential Thermal Analysis”; Anal. Chem. 29(11) 1702-1706, 1957
- [2.37] Boswell F. G.; “On the calculation of activation energies using a modified Kissinger method”; J. Therm. Anal. 18(2) 353-358, 1980
- [2.38] Cullity B. D.; “Elements of X-Ray diffraction”; Reading, M.A. Addisonwesley, 1978
- [2.39] Herzer G.; “Grain size dependence of coercivity and permeability of Nanocrystalline ferromagnets”; IEEE Trans. Magn., **MAG-26** 1397, 1990.
- [2.40] Herzer G.; “Grain structure and magnetism of nanocrystalline ferromagnetic”, IEEE Trans. Magn., 25(5), 3327-3329, 1989.
- [2.41] Alben R., Becker J. J. and Chi M. C.; “Random Anisotropy in Amorphous Ferromagnets”; J. Appl. Phy. **49** 1653-1658, 1978.
- [2.42] Chudnovsky E. M., Saslow W. M. and Serota R. A.; “Ordering in ferromagnets with random anisotropy”, Phys. Rev. B33, 251, 1986.
- [2.43] Bertotti G., Ferrara E., Fiorillo F. and Tiberto P.; Mat. Sci. Eng. **A**, **226-228** 603, 1997
- [2.44] Coey JMD; “Rare-earth iron Permanent magnets”; Oxford; Oxford Science Publications, Clearendon Press, 1996
- [2.45] Hernando A., Vazquez M., Kulik T. and Prados C.; “Analysis of the dependence of Spin-Spin correlations on the thermal treatment of the Nanocrystalline materials”; Phys. Rev. B **51** 3581, 1995
- [2.46] Kouvel J. S.; “Magnetism and Metallurgy”; eds. A. Berkowitz and E. Kneller Academic press, New York, **Vol. 2A**, P 523,1969
- [2.47] Mc Henry M. E., Willard M. A. and Laughlin D. E.; “Amorphous and nanocrystalline materials for application as soft magnets”; Prog. Mat. Sci. 44, 291-433, 1999
- [2.48] Yamaguchi K. and Mizaguchi T.; J. Phys. SOC. Japan, 39, 541, 1075
- [2.49] Bozorth R.; “Ferromagnetism”, D. Van Nostrand, Princeton N. J. 76, 1951
- [2.50] Bozorth; “Ferromagnetism” , D. Van Nordtrand Company, Inc. Priceton, NJ, p.64, 1964.

- [2.51] Hernando A. and Kulik T.; “Exchange interaction through amorphous paramagnetic layers in ferromagnetic nanocrystals”; Phys. Rev. B **49** 7064, 1994
- [2.52] Handrich K.; “Conditions for the Existence of Amorphous Ferromagnets” Phys. Stat. Sol. (b) 53, K17, 1972

Chapter III

- [3.1] Turnbull D.; “Under what conditions can a glass be formed?”; Contemp. Phys. 10, 473-488, 1969
- [3.2] Duwez P., Willens R. H. and Kelment Jr. W.; J. Appl. Phys. Lett., 31, 1136, 1960.
- [3.3] Coey JMD and Sun H.; J. Magn. Magn. Mater., 87, 1251, 1991.
- [3.4] Schnitzke K., Schultz L., Wecker J. and Katter M.; J. Appl. Phys. Lett., 57, 2853, 1990.
- [3.5] Le Chatelier H.; Bull SOC. France Mineral, 10, 204, 1987
- [3.6] Pearson W. B.; “A Hand book of Lattice spacing and Structures of Metals and Alloys” (Oxford Pergamon), 1958
- [3.7] M. A. Mazid and M. A. Chowdhury; “Design and Construction of Forner type Vibrating Sample Magnetometer”; AECD/MMD/1 (Bangladesh). June, 1986
- [3.8] Simon Foner; “Versatile and Sensitive Vibrating Sample Magnetometer”; Rev. Sci. Instr. 30, 160, 1959

Chapter IV

- [4.1] Koster U. and Meinhardt J; Mat. Sci. Eng., AI 78:271, 1994.
- [4.2] Kuliik T., Hernando A and Vazquez M.; J. Magn. Magn. Mater., 133:130, 1994
- [4.3] Chen C. L. and Hasegawa R. S.; “Mössbauer study of glassy alloy (Fe-Mo)₈₀B₂₀; J. Appl. Phys. 49(3) 1721, 1978

- [4.4] Moorjani K., Chatak S. K., Rao K. V., Kramer B. and Chen H. S.; Int. Conf. on Liquid and Amorphous Metals, Grenoble, France, 1980.
- [4.5] Herzer G.; "Elsevier Hand Book of Magnetic Materials", 10, 427, 1997.
- [4.6] Mc Henry M. E., Willard M. A. and Laughlin D. E.; "Amorphous and nanocrystalline materials for applications as soft magnets." Prog. Mat. Sci. 44, 29-433, 1999.
- [4.7] Manjura Hoque S., Hakim M. A. and, Chau N.; "Ultra soft magnetic properties devitrified $\text{Fe}_{75.5}\text{Nb}_{2.4}\text{Cu}_{0.6}\text{Si}_{13}\text{B}_{8.5}$ alloy" Mat. Chem. Phys. 101, 112-117, 2007.
- [4.8] Saha D. K. and Hakim M. A.; Journal of Bangladesh Academy of Sciences; Vol. 30, No. 2, 177-187, 2006.
- [4.9] Marzo F. E., Pierna A. R. and Altube A. A.; "Analysis of nanocrystallization of FINEMET type alloy by temperature modulated differential scanning calorimetry"; Journal of Non-crystalline solids, 287, 349-354, 2001.
- [4.10] Hono K., A-Inoue and Sakurai T.; Appl. Phys. Lett., 58, 2180, 1991.
- [4.11] Kissinger H. E.; "Reaction Kinetics in Differential Thermal Analysis" Anal. Chem., 29(11), 1702-1706, 1957.
- [4.12] Illekova E.; Thermochemica Acta, 280-281, 289, 1996.
- [4.13] Chen C. L. and Hasagwa R. S.; ibid, Vol.49, pp.1721, 1978.
- [4.14] Liu T., Chen N., Xu Z. X. and Ma R. Z.; "The amorphous to nanocrystalline transformation in $\text{Fe}_{73.5}\text{Cu}_1\text{Nb}_3\text{Si}_{13.5}\text{B}_9$ studied by thermogravimetry analysis"; J. Magn. Mater. 152, 359-364, 1996.
- [4.15] Herzer G.; "Grain Structure and Magnetism of Nanocrystalline ferromagnets", IEEE Trans. Magn., 25(5), 3327-3329, 1989.
- [4.16] Yoshizawa Y., Oguma S. and Yamachi K.; "New Fe-based soft magnetic amorphous alloys composed of ultrafine grain structure"; J. Appl. Phys. 64(10), 6044-6046, 1988.

- [4.17] Pearson W. B.; "A Hand book of Lattice spacing and Structures of Metals and Alloys" (Oxford Pergamon), 1958.
- [4.18] Noor. S., "Effects of two-step annealing on complex permeability of Fe-Nb-Cu-Si-B nanocrystalline soft magnetic materials" M. Phil Thesis, , KUET, P 70-72, March 2005.
- [4.19] Mazid M. A. and Chowdhury M. A.; "Design and Construction of Forner type Vibrating Sample Magnetometer"; AECD/MMD/1(Bangladesh), June, 1986.
- [4.20] Haranda G. R., Gonzalez J. and Kulakowski K.; J. Appl. Phys.; 83: 6341, 1998.

CONFERENCE PUBLICATIONS

1. A. K. M. Asaduzzaman, M. A. Hossain, S. S. Sikder and M. A. Gafur; “Crystallization Behavior and Activation Energy of Fe-X-Nb-Si-B [X = Cu, Au & Ag] Alloys” International Conference on Physics 2016, 10-12 March.
2. A. K. M. Asaduzzaman, M. A. Hossain, S. S. Sikder and M. A. Gafur; “Influence of Annealing Condition on Structural Properties of Nanocrystalline $\text{Fe}_{73.5}\text{Cu}_1\text{Nb}_3\text{Si}_{13.5}\text{B}_9$ Alloy”, Conference on Weather Forecasting and Advances in Physics; Bangladesh Perspectives, 21 May 2016.